

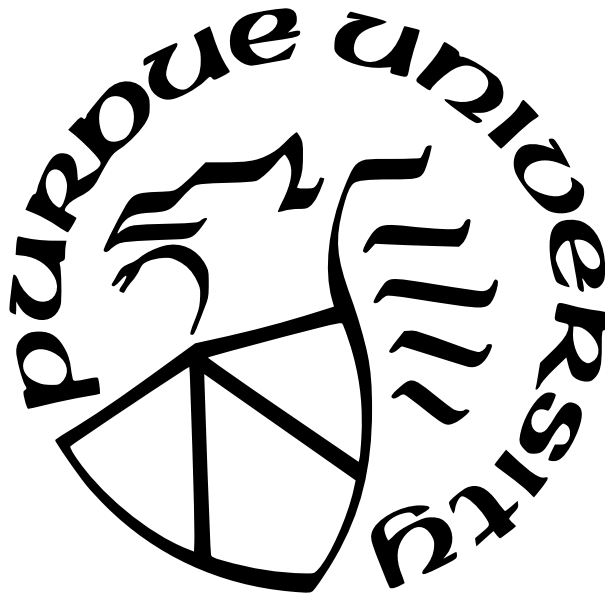
**CONSTITUTIVE MODELING OF THIN-WALLED
COMPOSITE STRUCTURES USING MECHANICS OF
STRUCTURE GENOME**

by
Ankit Deo

A Dissertation

*Submitted to the Faculty of Purdue University
In Partial Fulfillment of the Requirements for the degree of*

Doctor of Philosophy



School of Aeronautics and Astronautics

West Lafayette, Indiana

December 2021

**THE PURDUE UNIVERSITY GRADUATE SCHOOL
STATEMENT OF COMMITTEE APPROVAL**

Dr. Wenbin Yu, Chair

School of Aeronautics and Astronautics

Dr. Andres Arrieta

School of Mechanical Engineering

Dr. Vikas Tomar

School of Aeronautics and Astronautics

Dr. Arun Prakash

School of Civil Engineering

Approved by:

Dr. Gregory Blaisdell

Dedicated to my parents, Smaranika, and Priti Prasad Deo.

ACKNOWLEDGMENTS

Completing this dissertation means a lot to me and it could not have been possible without the help and guidance of several people.

Firstly, I am forever indebted to my advisor, Prof. Wenbin Yu, for his constant guidance and support without which the current work would've never began. His constant words of encouragement along with the professional values (truth, unity, balance and humble boldness) which he upholds and instills in his students, have been the guiding light through the past 6 years of my stay here. I have always appreciated his patience and perseverance in tackling the various problems I have posed. I feel very fortunate to have him as my advisor.

I am also grateful to my other committee members – Prof. Vikas Tomar, Prof. Andres Arrieta and Prof. Arun Prakash for their time and constructive suggestions in improving my dissertation.

I would like to thank my lab mates at the Multiscale Structural Mechanics Lab, past and present: Dr. Liang Zhang, Dr. Fang Jiang, Dr. Bo Peng, Dr. Hamsasew M. Sertse, Dr. Ning Liu, Dr. Zhengyuan Gao, Dr. Ernesto Camarena, Dr. Orzuri Rique Garaizar, Fei Tao, Banghua Zhao, Haodong Du, Rong Chiu, Kshitiz Swaroop and Khizar Rouf for their constant support. I would specifically like to thank Fei Tao for lending an ear to discuss new ideas and also personal matters.

I would also like to thank my friends: Radhika, Omanshu, Victoria, Raj, Jairaj, Priya, Adwait, and Monika for making my life at Purdue enjoyable. I am indebted to Raj for the countless hours he spent proof reading my technical articles, which ranged from Journal papers to Preliminary report. I would like to thank my closest friends (Vedant and Varun) and my cousin brother (Sumeet Dada) for being around in my times of need. Last but not least I would like to thank my parents for believing in me and constantly encouraging me to exceed my expectations.

TABLE OF CONTENTS

LIST OF TABLES	7
LIST OF FIGURES	8
ABSTRACT	10
1 INTRODUCTION	11
1.1 Thin-walled beams	11
1.2 Thin-walled plates	14
1.3 Thin-walled 3D structures	17
1.4 Motivation and objective	19
1.5 Outline of this thesis	20
2 FORMULATION	21
2.1 General formulation	21
2.2 Variational statement and kinematics	26
2.3 MSG thin-walled beams	27
2.4 MSG thin-walled plates	32
2.5 MSG thin-walled 3D structures	36
2.6 Constraints and boundary conditions	40
2.7 Finite element implementation	42
3 RESULTS	50
3.1 Equivalent beam properties	50
3.1.1 Isotropic strip	50
3.1.2 Isotropic I-section	52
3.1.3 Anisotropic I-section	54
3.1.4 Circular tube	57
3.1.5 Realistic wind turbine blade section	61
3.1.6 Isotropic multi-cell box section	63

3.2	Equivalent plate properties	65
3.2.1	Isotropic corrugated plate	65
3.2.2	Isotropic corrugated panel (with irregular thickness)	66
3.2.3	Anisotropic corrugated plate	68
3.3	Equivalent 3D properties	72
3.3.1	Isotropic cellular solid with varying flange angle	72
3.3.2	Hierarchical square	80
3.3.3	Composite square	83
4	CONCLUSION AND FUTURE PROSPECTS	89
4.1	Conclusion	89
4.2	Future prospect: MSG-TW using RM plate model	90
A	SLOPE CONTINUITY CONDITION	96
B	ANALYTICAL SOLUTION FOR A CIRCULAR TUBE	99
	REFERENCES	103
	VITA	109

LIST OF TABLES

3.1	Stiffness value for an isotropic strip section: (a) MSG-TW (Centric), (b) Harursampath et al. [20], (c) Yu et al. [18], and (d) MSG solid.	51
3.2	Stiffness value for an isotropic I-section: (a) MSG-TW (Centric), (b) MSG-TW (Off-Centric), (c) Harursampath et al. [20], (d) Yu et al. [18], and (e) MSG solid.	52
3.3	Stiffness value for an anisotropic I section: (a) MSG-TW(Centric),(b) MSG-TW(Off-Centric) (c) Harursampath et al. [20], (d) Chandra et al. [72], and (e) MSG solid.	56
3.4	Stiffness value for an isotropic I-section: (a) MSG-TW (Centric), (b) Yu et al. [18], and (c) MSG solid.	58
3.5	Stiffness value for realistic wind turbine blade section: (a) MSG solid (b) MSG-TW(Off-Centric), and (c) Error %.	63
3.6	Stiffness value for an isotropic multi-cell section: (a) MSG-TW (Centric), (b) MSG solid, and (c) Error %.	65
3.7	Equivalent plate properties for an isotropic corrugated plate: (a) MSG-TW, (b) Xia et al. [27], (c) Ye et al. [44] and (d) MSG solid.	67
3.8	Membrane and bending moduli for an isotropic corrugated panel (a) MSG-TW, (b) Buannic et al. [2] and (c) MSG solid.	68
3.9	Equivalent plate properties for an anisotropic corrugated sheet: (a) MSG-TW, (b) Park et al. [74] and (c) MSG solid.	70
3.10	Equivalent 3D stiffness matrix of a cellular solid structure for $\theta = 15^\circ$ (a) MSG-TW, (b) MSG solid model, and (c) Error %.	78
3.11	Equivalent 3D stiffness matrix of a cellular solid structure for $\theta = -15^\circ$ (a) MSG-TW, (b) MSG solid model, and (c) Error %.	79
3.12	Equivalent 3D stiffness matrix of a hierarchical square for $r = 5$ cm (a) MSG-TW, (b) MSG solid model, and (c) Error %.	83
3.13	Equivalent 3D stiffness matrix of a composite square (a) MSG-TW, (b) MSG solid model, and (c) Error %.	85

LIST OF FIGURES

1.1	Thin-walled beam.	12
1.2	Types of corrugated structures.	14
1.3	RVE model using plate elements [27].	16
1.4	Two-step homogenisation process.	17
1.5	Thin-walled 3D structure [52].	18
2.1	Various structures and their corresponding SGs.	22
2.2	Local-global coordinate transformation.	24
2.3	Slope continuity constraint $\Delta\alpha = 0$	40
2.4	Elemental coordinates and dofs.	43
3.1	Isotropic Strip.	51
3.2	Convergence study of isotropic I-section.	53
3.3	Overlaps in an isotropic I-section.	54
3.4	Thin-walled anisotropic I section.	55
3.5	Thin-walled composite circular tube section.	57
3.6	Convergence study of composite circular tube with respect to aspect ratio.	59
3.7	Convergence study of composite circular tube with respect to number of segments.	60
3.8	Realistic composite wind turbine multi-cell section [73].	61
3.9	MSG-TW model for realistic composite wind turbine multi-cell section [73].	62
3.10	Isotropic multi-cell section.	64
3.11	Isotropic corrugated plate.	66
3.12	Isotropic corrugated panel (with irregular thickness).	67
3.13	Anisotropic corrugated sheet.	69
3.14	Mode shape corresponding to fundamental frequency of the plate.	71
3.15	Cellular solid structure.	73
3.16	Equivalent Young's modulus of a cellular solid structure in x_2 direction.	74
3.17	Equivalent Young's modulus of a cellular solid structure in x_3 direction.	75
3.18	Equivalent shear modulus of a cellular solid structure in $x_2 - x_3$ direction.	76
3.19	In-plane Poisson's ratio of a cellular solid structure.	77

3.20	Schematic of a hierarchical square SG.	80
3.21	Equivalent Young's modulus of a hierarchical square.	81
3.22	Equivalent shear's modulus of a hierarchical square in $x_2 - x_3$ direction.	82
3.23	In-plane Poisson's ratio of a hierarchical square.	82
3.24	Schematic of a composite square SG.	84
3.25	Variation of $2E_{13}$ to a global strain of $\Gamma_{33} = 0.01$	86
3.26	Variation of E_{22} to a global strain of $\Gamma_{33} = 0.01$	86
3.27	Variation of E_{22} and $2E_{13}$ along the reference line of the top flange.	87
4.1	Rotational kinematics variables.	91
4.2	Convergence study of isotropic strip section.	95
4.3	$2\epsilon_{13}$ distribution along the middle reference line.	95
A.1	Slope continuity	96

ABSTRACT

Quick and accurate predictions of equivalent properties for thin-walled composite structures are required in the preliminary design process. Existing literature provides analytical solutions to some structures but is limited to particular cases. No unified approach exists to tackle homogenization of thin-walled structures such as beams, plates, or three-dimensional structures using the thin-walled approximation. In this work, a unified approach is proposed to obtain equivalent properties for beams, plates, and three-dimensional structures for thin-walled composite structures using mechanics of structure genome. The adopted homogenization technique interprets the unit cell associated with the composite structures as an assembly of plates, and the overall strain energy density of the unit cell as a summation of the plate strain energies of these individual plates. The variational asymptotic method is then applied to drop all higher-order terms and the remaining energy is minimized with respect to the unknown fluctuating functions. This has been done by discretizing the two-dimensional unit cell into one-dimensional frame elements in a finite element description. This allows the handling of structures with different levels of complexities and internal geometry within a general framework. Comparisons have been made with other works to show the advantages which the proposed model offers over other methods.

1. INTRODUCTION

The preliminary design of aerospace structures requires quick and accurate prediction of their mechanical behavior. For a particular class of structures which can be constructed by repeating a fundamental building block (unit cell) many times, a multiscale approach is usually adopted. A constitutive modeling is performed over the unit cell to obtain the constitutive models for the structure which is to be used as inputs for the global structural analysis. Various methods exist which range from using analytical formulations to using two-dimensional (2D) or three-dimensional (3D) finite elements. Representative volume element (RVE) analysis [1]–[3], mechanics of structure genome (MSG) [4], [5] and mathematical homogenisation theory (MHT) [6], [7] are a few of the techniques used for multiscale modeling. Within this class of structures that can be analyzed using the multiscale techniques a niche class of structures exist, which can be considered as thin-walled structures because the structure consists of members with small thickness. These structures can be classified based on the type of global structural models under consideration into beams, plates, and 3D structures.

1.1 Thin-walled beams

Thin-walled beams are a particular class of structures for which the thickness of the walls is much smaller than the overall cross-section of the structure, which is, in turn, small in comparison to the overall length of the structure, i.e., all the three dimensions are of different orders of magnitude. The previous statement can be written as $c/l \ll 1$, where c is the characteristic dimension of the cross-section and l the wavelength of deformation along the beam; $h/c \ll 1$, where h is the maximum thickness of the wall. A typical thin-walled beam is shown in Figure 1.1 and the beam cross-sectional properties can be acquired by describing the whole cross-section using a 2D solid model in MSG. As shown in Figure 1.1, thin-walled approximations can also be used to obtain the cross-sectional properties by considering the dotted lines as the plate reference line which are made of four segments $A1 - A2$, $A2 - A3$, $A3 - A4$, and $A4 - A1$. Thin-walled beams have found use in applications such as wind turbine blades, rocket motor casing, tennis rackets, fishing rods, offshore drilling bits etc.

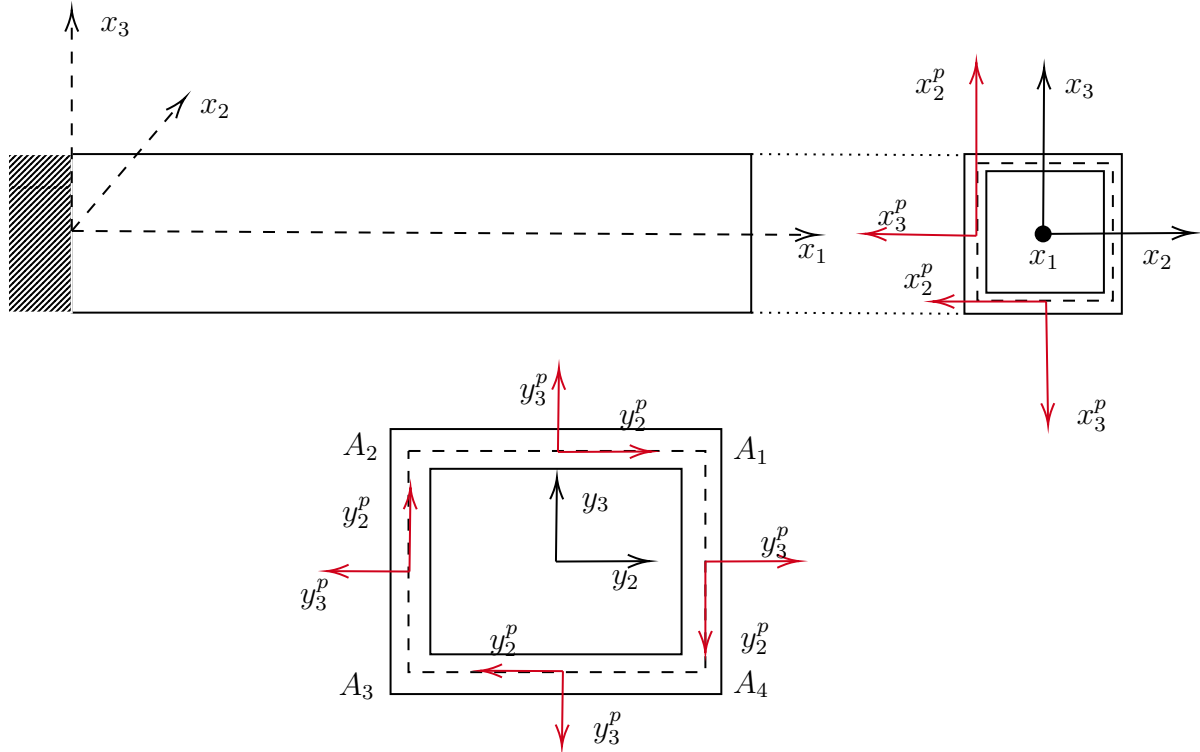


Figure 1.1. Thin-walled beam.

[8]–[13]. Using the inherent small parameters present in the beam, c/l and h/c , researchers have developed thin-walled beam theories which provide reasonably accurate results with a significant decrease in computational effort. Thin-walled beam theories present in current literature can be broadly divided into two different classes of approaches, the first one invoking assumptions before the derivation [14]–[16] and the second one using asymptotic methods based on dropping small terms which have small contributions to the overall strain energy [17]–[20].

The assumptions which are based on engineering intuition in the first class of approaches can be a certain form of the displacement field or integral of particular stress fields being zero, or certain strain components being zero. Although this approach does provide reasonably accurate results, depending on the choice of the displacement field or different approximations the final results vary and hence the results cease to be consistent in nature. Especially for the case of composite materials, where all the modes of displacement field could be potentially coupled, the theories developed using these assumptions might fail.

The second class of approaches use asymptotic methods to obtain beam models of different refinements, i.e., the higher order the terms incorporated, the higher the degrees of refinement obtained. In this form of approach two sub-classes exist, formal asymptotic method (FAM) [21] and variational asymptotic method (VAM) [22]. The author prefer the use of VAM over FAM. The reason VAM was chosen over FAM is because it is much easier to perform a finite element (FE) analysis on the weak form of the equations (which is inherently used in the case of VAM) rather than having to convert a set of partial differential equations into a weak form which is used in the case of FAM. VAM accounts for material anisotropy in a systematic manner and the modes of deformation which contribute most significantly to the energy emerge out of the formulation. VAM was first used for shell modelling in [22]. The concept was further enhanced for beam modelling in [23] and converted into a commercial software called the Variational asymptotic beam sectional analysis (VABS). VABS takes into consideration initial twist and curvatures of the beam, providing accurate beam properties which are inputs for its sister software – Geometrically exact beam theory (GEBT) for performing the global beam analysis [24].

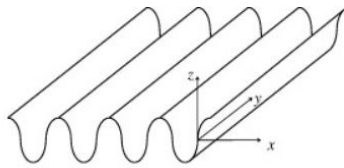
The case of thin-walled cross-sections for beams was first tackled in an analytical fashion using VAM in [19], but since the shell bending terms were neglected, the beam stiffness matrix obtained was stiffer in comparison to VABS. The shell bending terms were incorporated into the formulation in [25] which increased the accuracy of the beam stiffness matrix in comparison to VABS. Initial twist was introduced into the formulation in [18] and initial curvatures were introduced in [17]. All the aforementioned works have strived towards obtaining an analytical solution to the beam cross-sectional analysis and provide reasonably accurate results but are restricted to only open and single cell cross-sections. Developing a practical multi-cell thin-walled beam theory poses a problem because finding a solution in an analytical fashion requires stress components at the junctions to be continuous which can be solved as shown in [26] but converting into a general-purpose code is challenging.

In the most recent publications related to this field, a thin-walled theory for restrained warping of open sections has been introduced in [20]. The overall cross-section has been considered as a collection of strips and the energy has been minimized for each strip individually. The method does provide accurate results for some cases, but as shown later in this

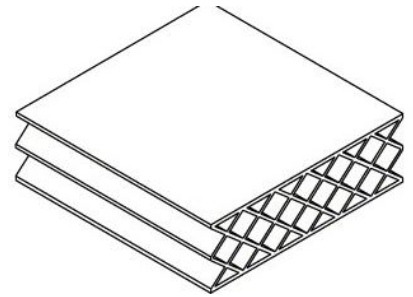
work, the theory breaks down for some cases because of inadequate continuity constraints at the junctions of each section.

1.2 Thin-walled plates

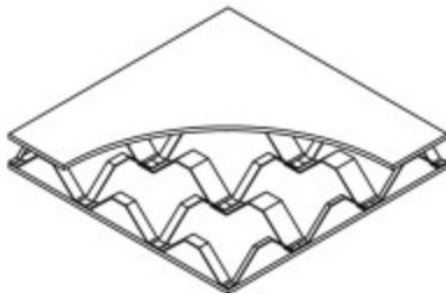
Thin-walled plates are a particular class of structures which have the unit cell repeating itself in one or two directions and the transverse direction being much smaller than the overall in-plane dimensions of the structure. The unit cell is, in turn, an assembly of plates or shells where the thickness of these plates or shells are much smaller than the overall dimension of the unit cell. A typical class of thin-walled plates is commonly referred to as corrugated structures and Figure 1.2 shows the different types of corrugated structures which can be classified into sheets, panels, and bi-directional panels.



(a) Corrugated sheets [27]



(b) Corrugated panels [28]



(c) Bi-directional corrugated panels [29]

Figure 1.2. Types of corrugated structures.

Corrugated structures show the unique property of having an order of magnitude difference in stiffness values in different directions and are widely used in aerospace, automotive, marine, and civil industry. They find applications such as decks, ship panels, and accommodation modules in the marine industry [30], as corrugated roofs and walls in the civil

industry [31], [32], as energy absorbing structures in the packaging industry [33], and as thermal protection systems in the aerospace industry [34], [35]. In recent years corrugated panels have found applications for flexible wings or morphing wings [36]–[39].

Equivalent plate properties for corrugated structures can be obtained by the traditional homogenisation techniques [5], [7] but since these amount to a large computational time and effort, researchers use the thin-walled approximation to obtain the equivalent plate properties [2], [3], [27], [40]–[45]. The methods to obtain equivalent plate properties can also be classified based on the underlying methodology used, into axiomatic [2], [3], [27], [40]–[43] and asymptotic [5], [7], [44], [45] approaches.

The theories in [5], [7] provide equivalent plate properties that replicate the original structure very accurately, these methods use 3D or 2D solid elements to describe the unit cell (FAM [7] and VAM [5]). Buannic et al. [2] and Biancolini [3] use 2D plate elements to describe the unit cell by considering an RVE, which is an assembly of plates as seen in Figure 1.3. The RVE used in this approach is 3D in nature, which makes it more computationally expensive than the approach proposed in this work. The work in [3] uses a condensation method to remove the internal nodes of the RVE by using a condensation matrix. Further the work in [3], creates submatrices relating the degrees of freedom (dofs) of the external nodes with the plate strain terms by applying the Kirchoff-Love assumption which decrease the computational time in comparison to [2] but still requires the whole RVE to be described with a finite element (FE) mesh. Moreover, this method assumes that the bending modes of deformation are decoupled from the stretching modes which hinders the model to account for all coupled deformation modes.

Xia et al. [27] is an axiomatic and analytical approach, which uses the equivalent force method in conjunction with the RVE analysis to obtain equivalent properties but are limited to symmetrically layered plates and cannot provide the coupling terms associated with membrane-bending response, i.e., the B matrix in the plate stiffness matrix. Further, [27] assumes particular local strain field components to be zero for a particular global response. For example, when $\bar{\epsilon} = [0 \ 0 \ 1 \ 0 \ 0 \ 0]^T$, ϵ_x and ϵ_y is assumed zero which inhibits in-plane axial-shear coupling at the unit cell level.

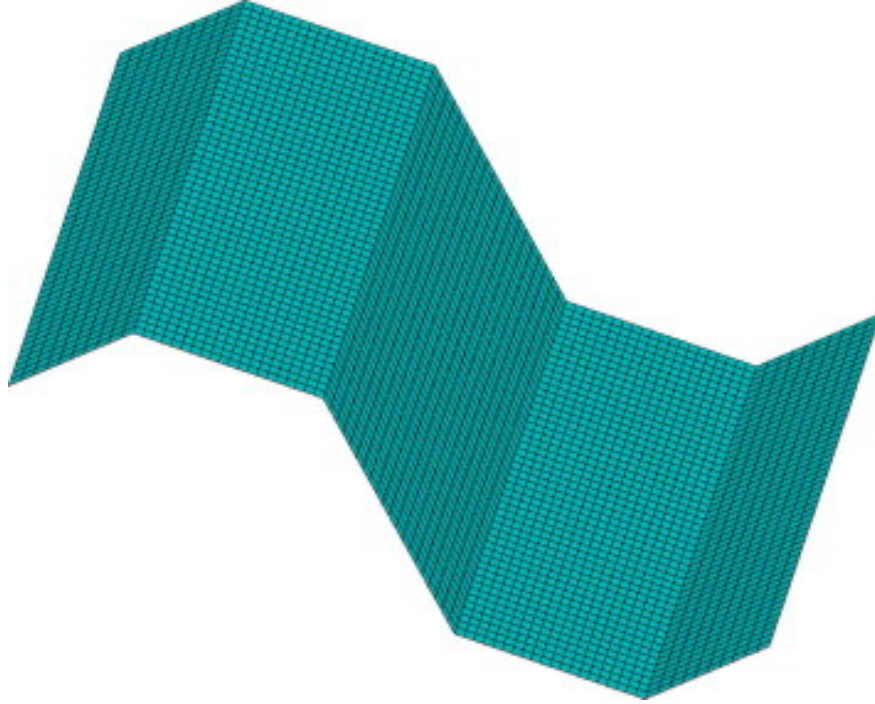


Figure 1.3. RVE model using plate elements [27].

Dayyani et al. [40] is also an axiomatic and analytical approach, which uses an innovative method of obtaining the overall strain energy produced in the unit cell (made from isotropic material) by virtual forces and then using the Castigliano's second theorem to obtain the force-displacement response. This model assumes the mode of deformations along both the in-plane directions and the out-of-plane directions to be individually decoupled and hence cannot capture the in-plane Poisson's effect.

Talbi et al. [42] and Aboura et al. [43] are also axiomatic approaches, which have been solved numerically and analytically. The work in [42] is an extension of [43], both these methods obtain material properties in the reference coordinate systems by transforming local material properties using tensor transformation laws and eventually use this information to obtain equivalent properties by averaging them. The models are limited to only orthotropic materials and provide a stiffer plate stiffness matrix because it assumes continuity of the displacement field at every point of the core and face sheets and not just at the crests. This assumption is outcome of the two-step homogenization process which has been used in the work and is illustrated in Figure 1.4. As shown in Figure 1.4, the core is considered to be

a homogeneous solid, and in the next homogenization step the panel is approximated as a laminate made of the face sheets with the homogeneous solid core hence assuming continuity at all points of the core and face sheets.

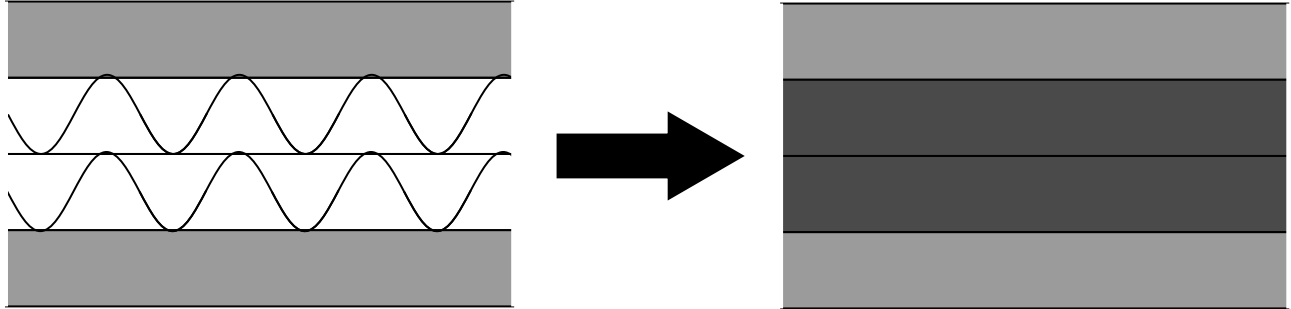


Figure 1.4. Two-step homogenisation process.

Cheon and Kim [41] is an axiomatic and analytical approach and obtains equivalent properties for corrugated panels by performing a two-step process of first calculating the effective plate properties of the core using [27] and then using those properties to obtain effective plate properties for the corrugated panel via a layer-wise theory. This method provides a stiffer equivalent plate because the connection between the core and the facing is assumed at every point of the core and face sheets and not just at the crests. This is again an example of the two-step homogenization process which is illustrated in Figure 1.4.

Although axiomatic approaches [27], [41]–[43] provide accurate results for some cases but due to the inherent assumptions present in them, they are often unable to capture the cases where all the modes of displacement field could be potentially coupled and cannot be easily assumed.

1.3 Thin-walled 3D structures

Thin-walled 3D structures studied in this work are a particular class of structures that have the unit cell being repeated in all three directions and the overall dimensions of the unit cell being much smaller than the dimensions of the structure. The unit cells are, in turn, an assembly of plates or shells where the thickness of these plates or shells are much smaller than the dimension of the unit cells. These structures are also referred to as cellular solids and are

widely used in applications where weight savings and multifunctional properties are critical. Aerospace sandwich cores, vibration and sound insulators, compact heat exchangers, and biomedical implants are a few application examples of these structures [46]–[51]. A typical thin-walled 3D structure is shown in Figure 1.5.

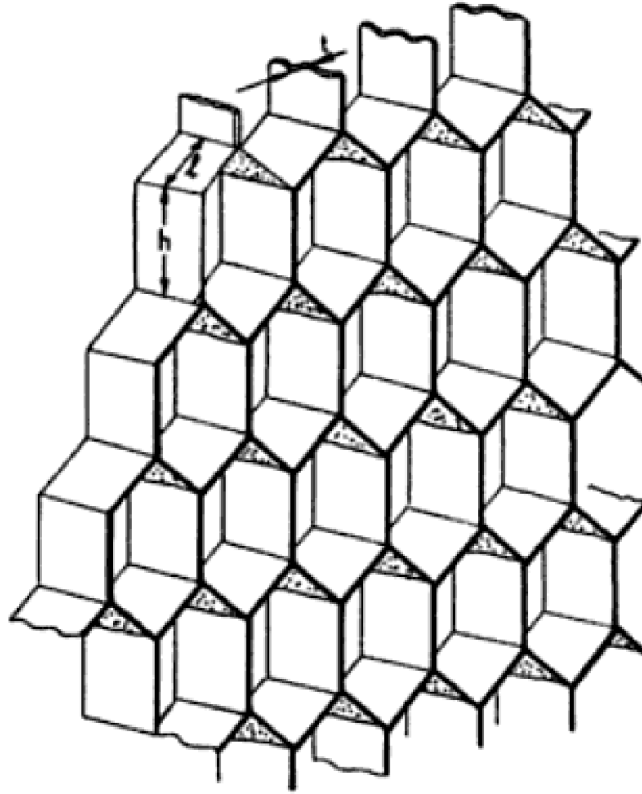


Figure 1.5. Thin-walled 3D structure [52].

As mentioned in the case of beams and plates, during the prototyping phase of the structure it is often impractical to analyze the entire structure as a whole hence researchers have made progresses towards obtaining equivalent or homogenized properties of the unit cells which are in turn used as inputs for the global 3D analysis. Several analytical and numerical approaches have been proposed in the literature to determine the equivalent mechanical properties of cellular materials [52]–[65]. Amongst these works, [52]–[56] obtain the equivalent properties which can be used by the classical elasticity model where every material point has 3 degrees of freedom (dofs) and [57]–[61] obtain the equivalent properties which can be used by the Cosserat elasticity model where every material point has 6 dofs. It should be

noted that [5] can also be used to obtain the equivalent properties which can be used by the classical elasticity model.

As briefly described above, several methods exist in literature to model the mechanics of cellular materials. Each method has its own assumptions, advantages and limitations. Amongst the works presented above, [52], [54]–[56] obtain the effective properties in close-form expressions and [5], [53], [66] obtain the effective properties numerically. As mentioned earlier [5] uses VAM and [53] uses FAM to obtain the properties.

All the above mentioned works which provide closed-form solutions have inherent assumptions associated with them. For example [52] only considers the bending deformation as the mode of deformation in elements of the unit cell.

In [54], a clear demarcation has been done as to when the elements have a bending dominant behaviour and when the element have a stretching dominant behaviour which does not make the theory general purpose to be used for composites as all modes of deformation can potentially be coupled.

Mousanezhad et al. [67] uses the Castigliano’s second theorem to obtain the equivalent 2D properties in which the in-plane Poisson’s effect is not considered when representing the overall strain energy associated with the unit cell and hence, the results obtained are less accurate than the approach proposed in this dissertation, which considers these terms.

1.4 Motivation and objective

Based on the literature review, works available in current literature have the following major drawbacks:

- Additional stress continuity condition need to be imposed for beams with closed sections which can be solved as shown in [26] but converting into a general-purpose code is challenging.
- Cases of non-corrugated but arbitrary shaped composite cores has not been studied [27], [41]–[44].

- For the case of equivalent 3D properties, general anisotropic materials have not been considered and out-of-plane properties [52]–[56] cannot be predicted, since these researches have only considered in-plane properties.
- No unified theories exist which can account for general thin-walled structures which might be modeled using a beam model, or a plate model, or an equivalent 3D model.

This need has been addressed in this work by using the mechanics of structure genome (MSG). MSG is a framework developed in [5] to provide constitutive models for various structures. MSG requires a structure gene (SG) to be defined as the smallest mathematical building block of the structure. The SG can be a 2D planar structure for the case where we have uniformity along one direction and hence MSG is more computationally efficient than the traditional RVE analysis. To use MSG for multi-scale constitutive modeling we need to answer the following three questions: 1) what is the model of the original structure? 2) what is the macroscopic model desired for structural design and analysis? 3) what is the structure gene? In the current work, the answer to the first question is a plate model for every segment of the unit cell. The answer to the second question depends on the global model desired and the answer to the third question is a 2D domain (see Figure 2.1).

1.5 Outline of this thesis

The report follows the following outline with Chapter 1 reviewing the related works and presents the motivation for the current work. Chapter 2 presents the theory and the overall framework for obtaining the equivalent properties of various structures. Chapter 3 presents the results we have obtained using the present theory for modeling thin-walled structures as beams, plates, and 3D solids. Chapter 4 summarizes the work done and possible extension of the work.

2. FORMULATION

2.1 General formulation

According to MSG, we chose the original model to be the Kirchhoff–Love plate model or the classical laminated plate theory (CLPT) which give the overall strain energy of the SG in terms of plate stiffness matrices and plate strain terms defined in the plate coordinate system. As seen in Figure 2.1, a thin-walled structure could externally look like a beam (the left figure), a plate (the middle figure), or a 3D structure (the right figure). Such structures can be homogenized using the regular formulation of MSG in [4] by describing each segment using a solid model (named MSG Solid in this dissertation). Moreover as seen in Figure 2.1 if it is uniform along one direction, the corresponding SG can be a 2D domain in comparison to a 3D domain. If the finite element method (FEM) is used for solving, 2D finite elements should be used to discretize the 2D SG and 3D finite elements should be used to discretize the 3D SG. However, if the thickness of each segment is small, it is possible for us to exploit the thinness of the segment to construct a thin-walled version of MSG (named MSG-TW in this dissertation). The corresponding SG retains its original dimension, however, it is formed by an assembly of straight line segments for the case of 2D SG and an assembly of surface elements for the case of 3D SG. The current work has only dealt with 2D SGs.

Since in the case of 2D SG it is a 1D problem, analytical solutions are possible for simple configurations. However for general configurations (e.g. a SG with many interconnected line segments), it is more convenient to use 1D finite elements to solve this problem. To facilitate the formulation, four coordinate systems are set up (see Figure 2.1):

- a global coordinate system $\mathbf{x} = (x_1, x_2, x_3)$, the origin of which can be situated anywhere in the structure. For a beam-like structure, it is convenient to set the origin at the geometric centroid of the cross-section. For a plate-like structure, it is convenient to set the origin at the geometric center of the thickness of the plate. This choice helps define the macroscopic displacements as the average of their counterparts of the original model.

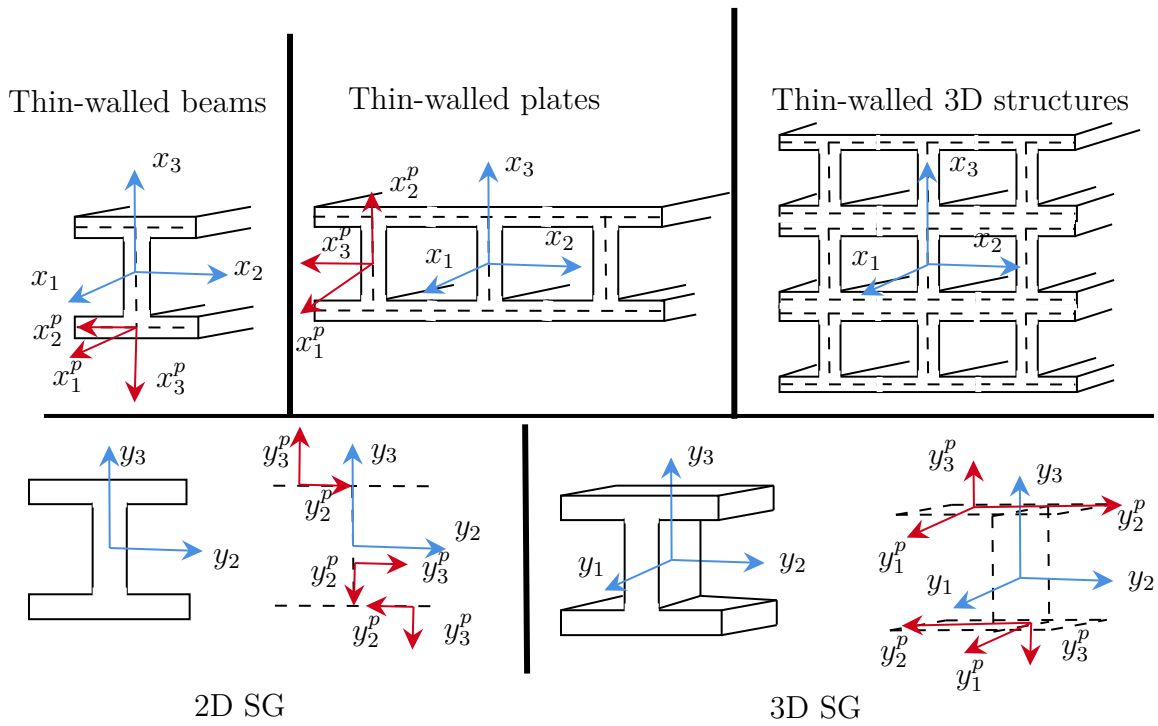


Figure 2.1. Various structures and their corresponding SGs.

- a global coordinate system along each segments $\mathbf{x}^P = (x_1^p, x_2^p, x_3^p)$, which is the rotation of \mathbf{x} to align itself with the reference line of every segment. Here, x_3^p is the outward normal to the reference line (for a 2D SG, $x_1^p = x_1$). x_2^p forms a right-hand system with x_1^p and x_3^p . This coordinate is defined for each segment and changes from segment to segment.
- a local coordinate system $\mathbf{y} = (y_1, y_2, y_3)$, which defines the SG. (y_1, y_2, y_3) align with (x_1, x_2, x_3) , respectively. It is noted that the local coordinate corresponding to x_1 does not exist when a 2D SG is considered and $\mathbf{y} = (y_2, y_3)$.
- a local coordinate system along each segment $\mathbf{y}^P = (y_1^p, y_2^p, y_3^p)$, which is rotation of \mathbf{y} to align itself with the reference line of every segment in the SG. (y_1^p, y_2^p, y_3^p) align with (x_1^p, x_2^p, x_3^p) respectively. This coordinate system is defined for each segment and changes from segment to segment within the SG. It is noted that the local coordinate corresponding to x_1^p does not exist when a 2D SG is considered and $\mathbf{y}^P = (y_2^p, y_3^p)$.

Since the SG is much smaller than the overall dimension of the structure, according to the original formulation of MSG [5], we can define the local coordinates $y_i = x_i/\varepsilon$ and $y_i^p = x_i^p/\varepsilon$, where ε is a small book-keeping parameter. Here the Latin indices assume value $i \equiv (1, 2, 3)$.

Any function of the original thin-walled structure can be written as a function dependent on \mathbf{x} and \mathbf{y} which are in turn dependent on \mathbf{x}^P and \mathbf{y}^P , $f \equiv f(x_i(x_\alpha^p), y_i(y_\alpha^p))$ (here $\alpha = 1, 2$ because x_3^p has been eliminated when we represent every segment as a plate). The partial derivative of this function with respect to x_α^p can be written as:

$$\begin{aligned}
\frac{\partial f}{\partial x_\alpha^p} &= \left(\frac{\partial x_i}{\partial x_\alpha^p} \frac{\partial f}{\partial x_i} \right)_{y_\alpha^p} + \left(\frac{\partial y_\alpha^p}{\partial x_\alpha^p} \frac{\partial y_i}{\partial y_\alpha^p} \frac{\partial f}{\partial y_i} \right)_{x_\alpha^p} \\
&= \left(\frac{\partial x_i}{\partial x_\alpha^p} \frac{\partial f}{\partial x_i} \right)_{y_\alpha^p} + \left(\frac{1}{\varepsilon} \frac{\partial f}{\partial y_\alpha^p} \right)_{x_\alpha^p}
\end{aligned} \tag{2.1}$$

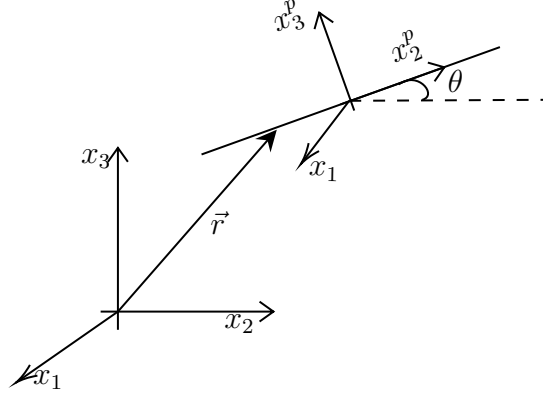


Figure 2.2. Local-global coordinate transformation.

For a 2D SG, $f \equiv f(x_1, x_z(x_2^p), y_z(y_2^p))$, with $z = 2, 3$. The partial derivative of the function with respect to x_1^p only depends on the global coordinate $x_1^p \equiv x_1$ and the partial derivative of the function with respect to x_2^p can be reduced as:

$$\frac{\partial f}{\partial x_2^p} = \left(\frac{\partial x_z}{\partial x_2^p} \frac{\partial f}{\partial x_z} \right)_{y_2^p} + \left(\frac{1}{\varepsilon} \frac{\partial f}{\partial y_2^p} \right)_{x_2^p} \quad (2.2)$$

In order to relate the local plate coordinate system with the global coordinate system, we consider a position vector $\vec{r}(x_1, x_2, x_3) \equiv \vec{r}(x_1, x_2^p, x_3^p)$, which can be defined in both the local plate coordinate system as well as the global coordinate system (see Figure. 2.2). Any tangent vector along x_i can be written as:

$$\hat{e}_i = \frac{\partial \vec{r}}{\partial x_i} \quad (2.3)$$

and correspondingly any tangent vector along x_i^p can be written as:

$$\hat{e}_i^p = \frac{\partial \vec{r}}{\partial x_i^p} = \sum_j \frac{\partial \vec{r}}{\partial x_j} \frac{\partial x_j}{\partial x_i^p} = \sum_j \hat{e}_j \frac{\partial x_j}{\partial x_i^p} \quad (2.4)$$

Eq. (2.4) can be explicitly be written in a matrix form as:

$$\begin{pmatrix} \hat{e}_1^p \\ \hat{e}_2^p \\ \hat{e}_3^p \end{pmatrix} = \begin{bmatrix} \beta_{11} & \beta_{21} & \beta_{31} \\ \beta_{12} & \beta_{22} & \beta_{32} \\ \beta_{13} & \beta_{23} & \beta_{33} \end{bmatrix} \begin{pmatrix} \hat{e}_1 \\ \hat{e}_2 \\ \hat{e}_3 \end{pmatrix} \quad (2.5)$$

here,

$$\beta_{ij} = \frac{\partial x_i}{\partial x_j^p}$$

As (x_1, x_2^p, x_3^p) is obtained by rotating (x_1, x_2, x_3) by an angle θ along x_1 , we have:

$$\begin{aligned} x_2^p &= \cos \theta x_2 + \sin \theta x_3 \\ x_3^p &= -\sin \theta x_2 + \cos \theta x_3 \end{aligned} \quad (2.6)$$

from which it can be seen that β_{ij} refer to the direction cosine matrix, transforming a vector in the x_i to x_i^p . For a 2D SG, $\beta_{1\alpha} = 0$ and $\beta_{11} = 1$. This transformation directly translates to the local \mathbf{y}^p and \mathbf{y} coordinate systems as well. We can represent the rotation matrix associated with the 2D SG as:

$$\begin{pmatrix} \hat{e}_1^p \\ \hat{e}_2^p \\ \hat{e}_3^p \end{pmatrix} = \begin{bmatrix} 1 & 0 & 0 \\ 0 & \dot{y}_2 & \dot{y}_3 \\ 0 & -\dot{y}_3 & \dot{y}_2 \end{bmatrix} \begin{pmatrix} \hat{e}_1 \\ \hat{e}_2 \\ \hat{e}_3 \end{pmatrix} \quad (2.7)$$

Here $(\dot{\cdot})$ refers to the derivative of any quantity with respect to y_2^p . It is noted:

$$\begin{aligned} \frac{\partial x_2}{\partial x_2^p} &= \frac{\partial y_2}{\partial y_2^p} = \dot{y}_2 \\ \frac{\partial x_3}{\partial x_2^p} &= \frac{\partial y_3}{\partial y_2^p} = \dot{y}_3 \end{aligned} \quad (2.8)$$

\ddot{y}_2 and \ddot{y}_3 vanish in this work since all the segments are discretized using straight lines. It is noted that even if a segment is curved, we can approximate it using enough number of straight line elements. Having defined the coordinate system, the next step in the formulation is to define the strain energy density of the SG which would be minimized with respect to the fluctuating functions to obtain the final equivalent properties and constitutive relations.

2.2 Variational statement and kinematics

Since the ratio of height to length of the segment is considered small and the external work done of the structure is one order smaller in comparison to the strain energy [5], we can represent the overall strain energy of the SG as:

$$\Pi = \frac{1}{2} \int_S \langle (\epsilon^p)^T K (\epsilon^p) \rangle dS \quad (2.9)$$

where K represents the plate stiffness matrix obtained by modeling each segment using MSG-based CLPT [5], and S denotes the domain of the global structural model. For the case of beams the integral \int_S is only performed along x_1 . For the case of plates the integral \int_S is performed along x_1 and x_2 . For the case of equivalent 3D model the integral \int_S is performed along x_1 , x_2 , and x_3 . K contains the well-known A , B , D matrices in CLPT. It is noted that MSG-based CLPT can obtain a plate model of the same form as the conventional CLPT without using ad hoc assumptions (Kirchhoff kinematic assumptions and plane stress assumption) for a segment made of arbitrary anisotropic materials. For example, MSG-based CLPT can model plates made of 3D woven composites. $\langle \cdot \rangle$ represents an integral along the reference lines for all the members within the SG. ϵ^p represents the plate strains in the (x_1, x_2^p, x_3^p) coordinate system. $\epsilon^p = [\epsilon_{11}^p, \epsilon_{22}^p, 2\epsilon_{12}^p, \kappa_{11}^p, \kappa_{22}^p, 2\kappa_{12}^p]^T$, where $\epsilon_{\alpha\beta}^p$ represent the in-plane strains and $\kappa_{\alpha\beta}^p$ represent the bending curvatures. They are defined as [5]:

$$\begin{aligned} \epsilon_{\alpha\beta}^p &= \frac{1}{2} \left(\frac{\partial u_\beta^p}{\partial x_\alpha^p} + \frac{\partial u_\alpha^p}{\partial x_\beta^p} \right) \\ \kappa_{\alpha\beta}^p &= -\frac{\partial^2 u_3^p}{\partial x_\alpha^p \partial x_\beta^p} \end{aligned} \quad (2.10)$$

where α and β take values 1 and 2, $u_i^p \equiv u_i^p(x_j(x_k^p), y_j(y_k^p))$ for the case of a 3D SG and $u_i^p \equiv u_i^p(x_1, x_2(x_2^p), x_3(x_2^p), y_2(y_2^p), y_3(y_2^p))$ for the case of a 2D SG. u_1^p represents the displacement field along x_1^p direction, u_2^p represents the displacement field along x_2^p direction, u_3^p represents the displacement field along x_3^p direction, of any point on the reference line of each segment. Depending on the global model, we can define u_1 , u_2 , and u_3 as the displacement field along

x_1 , x_2 , and x_3 respectively and u_i^p are related to u_i with the help of the rotation matrix defined in Eq. (2.5):

$$\begin{Bmatrix} u_1^p \\ u_2^p \\ u_3^p \end{Bmatrix} = \begin{bmatrix} \beta_{11} & \beta_{21} & \beta_{31} \\ \beta_{12} & \beta_{22} & \beta_{32} \\ \beta_{13} & \beta_{23} & \beta_{33} \end{bmatrix} \begin{Bmatrix} u_1 \\ u_2 \\ u_3 \end{Bmatrix} \quad (2.11)$$

For the case of 2D SG made of straight plate segments, the rotation matrix defined in Eq. (2.7) can be employed and Eq. (2.11) reduces to:

$$\begin{Bmatrix} u_1^p \\ u_2^p \\ u_3^p \end{Bmatrix} = \begin{bmatrix} 1 & 0 & 0 \\ 0 & y_2 & y_3 \\ 0 & -y_3 & y_2 \end{bmatrix} \begin{Bmatrix} u_1 \\ u_2 \\ u_3 \end{Bmatrix} = \Omega \begin{Bmatrix} u_1 \\ u_2 \\ u_3 \end{Bmatrix} \quad (2.12)$$

Having defined the plate strain terms in the global coordinate system, the next step in the formulation is to define the 3D displacement field of the original structures. These depend on the final global model and have been defined in [4]. In the subsequent sections we have taken these displacement fields and written the plate strains corresponding to the original structure in terms of the global model and small fluctuating functions. These plate strains would eventually be used in Eq. (2.9) to formulate a minimization problem to obtain the fluctuating fields in terms of the global strain fields.

2.3 MSG thin-walled beams

To model a thin-walled structure as a beam, we have taken the displacement field from [4] and derived the local plate strain terms (Eq. (2.10)) for a 2D SG. According to [4] the displacement field for thin-walled beams, $u_i(x_1, y_2(y_2^p), y_3(y_2^p))$, can be written as:

$$\begin{aligned} u_1(x_1, y_2(y_2^p), y_3(y_2^p)) &= \bar{u}_1(x_1) - \varepsilon y_2 \bar{u}'_2(x_1) - \varepsilon y_3 \bar{u}'_3(x_1) + \varepsilon w_1(x_1, y_2, y_3) \\ u_2(x_1, y_2(y_2^p), y_3(y_2^p)) &= \bar{u}_2(x_1) - \varepsilon y_3 \Phi(x_1) + \varepsilon w_2(x_1, y_2, y_3) \\ u_3(x_1, y_2(y_2^p), y_3(y_2^p)) &= \bar{u}_3(x_1) + \varepsilon y_2 \Phi(x_1) + \varepsilon w_3(x_1, y_2, y_3) \end{aligned} \quad (2.13)$$

where u_i and \bar{u}_i denote the displacement field of the original structure and the displacement field of the Euler–Bernoulli beam model respectively. Φ represents the sectional rotation. w_i are the unknown fluctuating functions associated with the displacement field in each direction of the coordinate system x_i , and they are used to describe deformation that cannot be described by the simpler kinematics of an Euler–Bernoulli beam model. Since we are constructing a beam model out of the original model, the kinematic fields in the beam model need to be defined in terms of the displacement field of the original model as:

$$\begin{aligned}
\bar{u}_1 &= \langle u_1 \rangle + \varepsilon \langle y_2 \rangle \bar{u}'_2 + \varepsilon \langle y_3 \rangle \bar{u}'_3 \\
\bar{u}_2 &= \langle u_2 \rangle + \varepsilon \langle y_3 \rangle \Phi \\
\bar{u}_3 &= \langle u_3 \rangle - \varepsilon \langle y_2 \rangle \Phi \\
\Phi &= \frac{1}{2} \langle u_{3,2} - u_{2,3} \rangle
\end{aligned} \tag{2.14}$$

The first three definitions physically mean that the beam displacements are averages of the 3D displacements over the SG with an offset of the corresponding rotations. The last definition physical means that the 1D rotation due to twist is the same as the true 3D twist averaged over the SG. $()'$ refers to the derivative with respect to x_1 .

As the equations on the right hand side of Eq. (2.13) is four times redundant in comparison to the left hand side, we would require four constraints on the introduced fluctuating functions. The definition of the beam displacements in Eq. (2.14) provides us with the necessary constraints on w_i which need to be imposed to solve the problem. The constraints are:

$$\begin{aligned}
\langle w_i \rangle &= 0 \\
\langle w_{3,2} - w_{2,3} \rangle &= 0
\end{aligned} \tag{2.15}$$

where, it can be seen these constraints make sure that the overall rigid body translations and rotations associated with the introduced fluctuating functions are zero. Due to the complexity of implementing the last constraint, we have opted to impose a similar constraint which was provided in [68] that can be written as:

$$\langle y_2 w_3 - y_3 w_2 \rangle = 0 \tag{2.16}$$

This constraint changes the definition of Φ to:

$$\Phi = \frac{\langle y_2 u_3 - y_3 u_2 \rangle - \langle y_2 \rangle \bar{u}_3 + \langle y_3 \rangle \bar{u}_2}{\varepsilon \langle y_2^2 + y_3^2 \rangle} \quad (2.17)$$

This definition can be physically interpreted as, the 1D twist associated with the SG is combination of average twist in the SG because of pure rotation (the underlined term) and the twist in the SG because of the offset of the origin in the SG.

If the geometrical centroid is chosen as the origin, we have $\langle y_2 \rangle = 0$ and $\langle y_3 \rangle = 0$, and the 1D displacement fields are the average of the the corresponding 3D displacements and the beam rotation corresponds to a pure rotation. If the geometrical centroid is not chosen as the origin, \bar{u}_i and Φ will assume a different meanings but the same constraints on the fluctuating functions are used. Substituting Eq. (2.13) into Eq. (2.12), we get:

$$\begin{aligned} u_1^p &= \bar{u}_1 - \varepsilon y_2 \bar{u}'_2 - \varepsilon y_3 \bar{u}'_3 + \varepsilon w_1 \\ u_2^p &= \dot{y}_2 \bar{u}_2 + \dot{y}_2 \bar{u}_3 + \varepsilon (\dot{y}_3 y_2 - \dot{y}_2 y_3) \Phi + \varepsilon \dot{y}_2 w_2 + \varepsilon \dot{y}_3 w_3 \\ u_3^p &= -\dot{y}_3 \bar{u}_2 + \dot{y}_2 \bar{u}_3 + \varepsilon (\dot{y}_2 y_2 + \dot{y}_3 y_3) \Phi - \varepsilon \dot{y}_3 w_2 + \varepsilon \dot{y}_2 w_3 \end{aligned} \quad (2.18)$$

Since for the thin-walled beam model we have, $u_i(x_1, y_2(y_2^p), y_3(y_2^p))$, the local plate strain terms definitions in Eq. (2.10) can be explicitly written as (using the partial derivative expression in Eq. (2.2)):

$$\begin{aligned} \epsilon_{11}^p &= \frac{\partial u_1^p}{\partial x_1} \\ \epsilon_{22}^p &= \frac{1}{\varepsilon} \frac{\partial u_2^p}{\partial y_2^p} \\ 2\epsilon_{12}^p &= \frac{\partial u_2^p}{\partial x_1} + \frac{1}{\varepsilon} \frac{\partial u_1^p}{\partial y_2^p} \\ \kappa_{11}^p &= -\frac{\partial^2 u_3^p}{\partial x_1^2} \\ \kappa_{22}^p &= -\frac{1}{\varepsilon^2} \frac{\partial^2 u_3^p}{\partial (y_2^p)^2} \\ 2\kappa_{12}^p &= -2 \frac{1}{\varepsilon} \frac{1}{\partial y_2^p} \left(\frac{\partial u_3^p}{\partial x_1} \right) \end{aligned} \quad (2.19)$$

and then on inputting Eq. (2.18) into Eq. (2.19) we get the following plate strain expressions:

$$\begin{aligned}
\epsilon_{11}^p &= \gamma_{11} + \varepsilon y_3 \kappa_2 - \varepsilon y_2 \kappa_3 + \underline{\varepsilon w_1'} \\
\epsilon_{22}^p &= y_2 \dot{w}_2 + y_3 \dot{w}_3 \\
2\epsilon_{12}^p &= \dot{w}_1 + (\varepsilon y_2 y_3 - \varepsilon y_3 y_2) \kappa_1 + \underline{\varepsilon (y_2 w_2' + y_3 w_3')} \\
\kappa_{11}^p &= y_2 \kappa_2 + y_3 \kappa_3 + \underline{\varepsilon (y_3 w_2'' - y_2 w_3'' - (y_3 y_3 + y_2 y_2) \kappa_1')} \\
\kappa_{22}^p &= \frac{1}{\varepsilon} (y_3 \ddot{w}_2 - y_2 \ddot{w}_3) \\
2\kappa_{12}^p &= -2 (\kappa_1 - \underline{y_3 \dot{w}_2' + y_2 \dot{w}_3'})
\end{aligned} \tag{2.20}$$

$(\ddot{\cdot})$ refers to the second derivative with respect to y_2^p and $(\cdot)''$ refers to the double derivative with respect to x_1 . ϵ_{11}^p physically represents the normal strain along the x_1 direction. ϵ_{22}^p physically represents the longitudinal strain along the x_2^p direction. $2\epsilon_{12}^p$ physically represents the shear strain along the $x_1 - x_2^p$ plane. κ_{11}^p represents the out-of-plane bending curvature along the x_2^p direction. κ_{22}^p represents the twist curvature along the x_1 direction. $2\kappa_{12}^p$ represents the out-of-plane bending curvature in the $x_1 - x_2^p$ plane.

In Eq. (2.20), the underlined terms in the in-plane local plate strain terms are of order $O(\hat{\varepsilon}\varepsilon)$. And the underlined terms in the out-of-plane bending curvature terms are of order $O(\hat{\varepsilon}\varepsilon^2)$. On inputting this form of the plate strain terms into the overall strain energy we see that the contributions of the underlined terms to the overall energy is of order $O(\hat{\varepsilon}^2\varepsilon h^2)$, which is asymptotically smaller than the contributions of the non-underlined terms which are of order $O(\hat{\varepsilon}^2 h^2)$ and hence are dropped. Here, h refers to the characteristic dimension of the cross-section.

The 1D beam strains in Eq. (2.20), $\epsilon = [\gamma_{11} \quad \kappa_1 \quad \kappa_2 \quad \kappa_3]^T$ are defined as:

$$\gamma_{11} = \bar{u}_1', \quad \kappa_1 = \Phi', \quad \kappa_2 = -\bar{u}_3'', \quad \kappa_3 = \bar{u}_2'' \tag{2.21}$$

where γ_{11} is the extensional strain, κ_1 is the twist rate, κ_2 and κ_3 are the bending curvatures along x_2 and x_3 respectively. Let us introduce new variables, w_i^p , such that:

$$\begin{Bmatrix} w_1^p \\ w_2^p \\ w_3^p \end{Bmatrix} = \Omega \begin{Bmatrix} w_1 \\ w_2 \\ w_3 \end{Bmatrix} \quad (2.22)$$

because while performing the finite element implementation of theory the shape functions will be defined along each segment in the (y_2^p, y_3^p) coordinate system, as the line integral in Eq. (2.9) is along the reference line of each segment for 2D SGs.

From Eq. (2.22), we have:

$$\begin{aligned} w_1^p &= w_1 \\ w_2^p &= \dot{y}_2 w_2 + \dot{y}_3 w_3 \\ w_3^p &= -\dot{y}_3 w_2 + \dot{y}_2 w_3 \end{aligned} \quad (2.23)$$

After dropping of all the asymptotically small terms, Eq. (2.20) can be written as:

$$\begin{aligned} \epsilon_{11}^p &= \gamma_{11} + \varepsilon y_3 \kappa_2 - \varepsilon y_2 \kappa_3 \\ \epsilon_{22}^p &= \dot{w}_2^p \\ 2\epsilon_{12}^p &= \dot{w}_1^p + (\varepsilon y_2 \dot{y}_3 - \varepsilon y_3 \dot{y}_2) \kappa_1 \\ \kappa_{11}^p &= \dot{y}_2 \kappa_2 + \dot{y}_3 \kappa_3 \\ \kappa_{22}^p &= -\frac{1}{\varepsilon} \dot{w}_3^p \\ 2\kappa_{12}^p &= -2(\kappa_1) \end{aligned} \quad (2.24)$$

which can be written in a matrix form as:

$$\epsilon^p = \mathbf{P}_0 \epsilon + \Gamma_h w^p \quad (2.25)$$

where

$$\mathbf{P}_0 = \begin{bmatrix} 1 & 0 & x_3 & -x_2 \\ 0 & 0 & 0 & 0 \\ 0 & x_2\dot{y}_3 - x_3\dot{y}_2 & 0 & 0 \\ 0 & 0 & \dot{y}_2 & \dot{y}_3 \\ 0 & 0 & 0 & 0 \\ 0 & -2 & 0 & 0 \end{bmatrix} \quad \Gamma_h = \begin{bmatrix} 0 & 0 & 0 \\ 0 & \frac{\partial}{\partial y_2^p} & 0 \\ \frac{\partial}{\partial y_2^p} & 0 & 0 \\ 0 & 0 & 0 \\ 0 & 0 & -\frac{1}{\varepsilon} \frac{\partial}{\partial y_2^p} \left(\frac{\partial}{\partial y_2^p} \right) \\ 0 & 0 & 0 \end{bmatrix} \quad (2.26)$$

Having defined the local plate strains in terms of the global beam strains, we move on to the plate modeling, here it is shown that the expression for the local plate strains are similar to the Eq. (2.26) with the exception of \mathbf{P}_0

2.4 MSG thin-walled plates

For the case of the plate model, we have taken the displacement field from [4] and derived the local plate strain terms (Eq. (2.10)) for a 2D SG. According to [4] the overall displacement field for the case of 2D SG and plate model, $u_i(x_1, x_2(x_2^p), y_2(y_2^p), y_3(y_2^p))$, can be written as:

$$\begin{aligned} u_1 &= \bar{u}_1(x_1, x_2) - \varepsilon y_3 \bar{u}_{3,1}(x_1, x_2) + \varepsilon w_1(x_1, x_2, y_2, y_3) \\ u_2 &= \bar{u}_2(x_1, x_2) - \varepsilon y_3 \bar{u}_{3,2}(x_1, x_2) + \varepsilon w_2(x_1, x_2, y_2, y_3) \\ u_3 &= \bar{u}_3(x_1, x_2) + \varepsilon w_3(x_1, x_2, y_2, y_3) \end{aligned} \quad (2.27)$$

where u_i and \bar{u}_i denote the displacement field of the original structure and the displacement field of the Kirchhoff–Love plate model. w_i are the unknown fluctuating functions associated with the displacement field in each direction of the coordinate system, x_i , and they are used to describe deformation that cannot be described by the simpler kinematics of the Kirchhoff–Love plate model. Since we are constructing a plate model out of the original model, the

kinematic fields in the plate model need to be defined in terms of the displacement field of the original model as:

$$\begin{aligned}
\bar{u}_1 &= \langle u_1 \rangle + \varepsilon \langle y_3 \rangle \bar{u}_{3,1} \\
\bar{u}_2 &= \langle u_2 \rangle - \varepsilon \langle y_3 \rangle \bar{u}_{3,2} \\
\bar{u}_3 &= \langle u_3 \rangle
\end{aligned} \tag{2.28}$$

$(\cdot)_{,a}$ refers to the derivative of (\cdot) with respect to x_a .

The physical meaning of these definitions is that the 2D displacements are the average of the original 3D displacements of the structure over the SG. If the origin of y_3 is at the geometrical centroid of the SG, \bar{u}_i are averages of the corresponding 3D displacements. The definition of the plate displacement fields in Eq. (2.28), provides us with the necessary constraints on w_i which need to be imposed to solve the problem. The constraints are:

$$\langle w_i \rangle = 0 \tag{2.29}$$

These constraints remove the rigid body translations associated with the introduction of the fluctuating functions. We would also have to impose periodic boundary conditions along the y_2 direction to respect the periodic nature of the SG. The imposing of the periodic boundary condition makes sure that the rigid body rotation associated with the introduction of the fluctuating functions is also zero. It should be noted that, if the geometrical centroid is not chosen as the origin, \bar{u}_i will assume a different meaning but the same constraints on the fluctuating functions are used. Now substituting Eq. (2.27) into Eq. (2.12), we obtain the 3D displacement field in the local plate coordinate systems as:

$$\begin{aligned}
u_1^p &= \bar{u}_1(x_1, x_2) - \varepsilon y_3 \bar{u}_{3,1}(x_1, x_2) + \varepsilon w_1(x_1, x_2, y_2, y_3) \\
u_2^p &= \dot{y}_2 \bar{u}_2 + \dot{y}_3 \bar{u}_3 - \varepsilon \dot{y}_2 y_3 \bar{u}_{3,2} + \varepsilon \dot{y}_2 w_2 + \varepsilon \dot{y}_3 w_3 \\
u_3^p &= -\dot{y}_3 \bar{u}_2 + \dot{y}_2 \bar{u}_3 + \varepsilon \dot{y}_3 y_3 \bar{u}_{3,2} - \varepsilon \dot{y}_3 w_2 + \varepsilon \dot{y}_2 w_3
\end{aligned} \tag{2.30}$$

Since for the thin-walled plate model we have, $u_i(x_1, x_2, y_2, y_3)$, the local plate strain terms definitions in Eq. (2.10) can be explicitly written as (using the partial derivative expression in Eq. (2.2)):

$$\begin{aligned}
\epsilon_{11}^p &= \frac{\partial u_1^p}{\partial x_1} \\
\epsilon_{22}^p &= \dot{y}_2 \frac{\partial u_2^p}{\partial x_2} + \frac{1}{\varepsilon} \frac{\partial u_2^p}{\partial y_2^p} \\
2\epsilon_{12}^p &= \frac{\partial u_2^p}{\partial x_1} + \dot{y}_2 \frac{\partial u_1^p}{\partial x_2} + \frac{1}{\varepsilon} \frac{\partial u_1^p}{\partial y_2^p} \\
\kappa_{11}^p &= -\frac{\partial^2 u_3^p}{\partial x_1^2} \\
\kappa_{22}^p &= -\left(\dot{y}_2^2 \frac{\partial^2 u_3^p}{\partial x_2^2} + \frac{\dot{y}_2}{\varepsilon} \frac{\partial}{\partial x_2} \left(\frac{\partial u_3^p}{\partial y_2^p} \right) + \frac{\dot{y}_2}{\varepsilon} \frac{\partial}{\partial y_2^p} \left(\frac{\partial u_3^p}{\partial x_2} \right) + \frac{1}{\varepsilon^2} \frac{\partial^2 u_3^p}{\partial (y_2^p)^2} \right) \\
2\kappa_{12}^p &= -2 \frac{\partial}{\partial x_1} \left(\dot{y}_2 \frac{\partial u_3^p}{\partial x_2} + \frac{1}{\varepsilon} \frac{\partial u_3^p}{\partial y_2^p} \right)
\end{aligned} \tag{2.31}$$

and then on inputting Eq. (2.30) into Eq. (2.31) we get the local plate strains in each segment as:

$$\begin{aligned}
\epsilon_{11}^p &= \epsilon_{11} + \varepsilon y_3 \kappa_{11} + \underline{\varepsilon w_{1,1}} \\
\epsilon_{22}^p &= \dot{y}_2^2 (\epsilon_{22} + \varepsilon y_3 \kappa_{22}) + \dot{y}_2 \dot{w}_2 + \dot{y}_3 \dot{w}_3 + \varepsilon (\underline{\dot{y}_2 w_{2,2} + \dot{y}_3 w_{3,2}}) \\
2\epsilon_{12}^p &= \dot{y}_2 (2\epsilon_{12} + \varepsilon y_3 (2\kappa_{12})) + \dot{w}_1 + \varepsilon (\underline{\dot{y}_2 w_{1,2} + \dot{y}_2 w_{2,1} + \dot{y}_3 w_{3,1}}) \\
\kappa_{11}^p &= \dot{y}_2 \kappa_{11} + \underline{\dot{y}_3 (\bar{u}_{2,11} - \varepsilon y_3 \bar{u}_{3,211})} + \varepsilon (\underline{\dot{y}_3 w_{2,11} - \dot{y}_2 w_{3,11}}) \\
\kappa_{22}^p &= \dot{y}_2 \left(1 + \dot{y}_3^2 \right) \kappa_{22} + \frac{1}{\varepsilon} (\dot{y}_3 \ddot{w}_2 - \dot{y}_2 \ddot{w}_3) + \underline{\dot{y}_2^2 \dot{y}_3 (\bar{u}_{2,22} - \varepsilon y_3 \bar{u}_{3,222})} \\
&\quad + \underline{2\dot{y}_2 (\dot{y}_3 \dot{w}_{2,2} - \dot{y}_2 \dot{w}_{3,2})} + \varepsilon \underline{\dot{y}_2^2 (\dot{y}_3 w_{2,22} - \dot{y}_2 w_{3,22})} \\
2\kappa_{12}^p &= 2\kappa_{12} + \underline{2\dot{y}_2 \dot{y}_3 (\bar{u}_{2,12} - \varepsilon y_3 \bar{u}_{3,212})} \\
&\quad + \underline{2(\dot{y}_3 \dot{w}_{2,1} - \dot{y}_2 \dot{w}_{3,1})} + 2\varepsilon \underline{\dot{y}_2 (\dot{y}_3 w_{2,21} - \dot{y}_2 w_{3,21})}
\end{aligned} \tag{2.32}$$

where the 2D plate strains $\epsilon = [\epsilon_{11} \quad \epsilon_{22} \quad 2\epsilon_{12} \quad \kappa_{11} \quad \kappa_{22} \quad 2\kappa_{12}]^T$, are defined as:

$$\begin{aligned}
\epsilon_{11} &= \bar{u}_{1,1}, & \epsilon_{22} &= \bar{u}_{2,2}, & 2\epsilon_{12} &= \bar{u}_{1,2} + \bar{u}_{2,1}, \\
\kappa_{11} &= -\bar{u}_{3,11}, & \kappa_{22} &= -\bar{u}_{3,22}, & 2\kappa_{12} &= -2\bar{u}_{3,12}
\end{aligned} \tag{2.33}$$

in which ϵ_{11} , ϵ_{22} , and $2\epsilon_{12}$ are the in-plane extensional and shear strains, κ_{11} , κ_{22} , and $2\kappa_{12}$ are the out-of-plane bending curvatures. Here again the underlined terms in the in-plane local plate strain terms are of order $O(\hat{\epsilon}\epsilon)$. And the underlined terms in the out-of-plane bending curvature terms are of order $O(\hat{\epsilon}^2\epsilon^2)$. On inputting this form of the plate strain terms into the overall strain energy we see that the contributions of the underlined terms to the overall energy is of order $O(\hat{\epsilon}^2\epsilon h^2)$, which is asymptotically smaller than the contributions of the non-underlined terms which are of order $O(\hat{\epsilon}^2 h^2)$ and hence are dropped. After dropping the asymptotically smaller terms, Eq. (2.32) can be written as:

$$\begin{aligned}
\epsilon_{11}^p &= \epsilon_{11} + \varepsilon y_3 \kappa_{11} \\
\epsilon_{22}^p &= \dot{y}_2^2 (\epsilon_{22} + \varepsilon y_3 \kappa_{22}) + \dot{y}_2 \dot{w}_2 + \dot{y}_3 \dot{w}_3 \\
2\epsilon_{12}^p &= \dot{y}_2 (2\epsilon_{12} + \varepsilon y_3 (2\kappa_{12})) + \dot{w}_1 \\
\kappa_{11}^p &= \dot{y}_2 \kappa_{11} \\
\kappa_{22}^p &= \dot{y}_2 (1 + \dot{y}_3^2) \kappa_{22} + \frac{1}{\varepsilon} (\dot{y}_3 \ddot{w}_2 - \dot{y}_2 \ddot{w}_3) \\
2\kappa_{12}^p &= 2\kappa_{12}
\end{aligned} \tag{2.34}$$

which can be written in a matrix form as:

$$\epsilon^p = \mathbf{P}_0 \epsilon + \Gamma_h w^p \tag{2.35}$$

where

$$\mathbf{P}_0 = \begin{bmatrix} 1 & 0 & 0 & x_3 & 0 & 0 \\ 0 & \dot{y}_2^2 & 0 & 0 & x_3 \dot{y}_2^2 & 0 \\ 0 & 0 & \dot{y}_2 & 0 & 0 & x_3 \dot{y}_2 \\ 0 & 0 & 0 & \dot{y}_2 & 0 & 0 \\ 0 & 0 & 0 & 0 & \dot{y}_2 (1 + \dot{y}_3^2) & 0 \\ 0 & 0 & 0 & 0 & 0 & 1 \end{bmatrix} \tag{2.36}$$

and Γ_h and w^p remain the same as that of the MSG thin-walled (MSG TW) beam model in Eq. (2.26) and Eq. (2.23).

2.5 MSG thin-walled 3D structures

As done for the previous cases, for the case of thin-walled 3D structures, we have taken the displacement field from [4] and derived the local plate strain terms (Eq. (2.10)) for a 2D SG. According to [4], the displacement field for the case of a 3D thin-walled structure, $u_i(x_1, x_2(x_2^p), x_3(x_2^p), y_2(y_2^p), y_3(y_2^p))$, can be written as:

$$\begin{aligned} u_1 &= \bar{u}_1(x_1, x_2, x_3) + \varepsilon w_1(x_1, x_2, x_3, y_2, y_3) \\ u_2 &= \bar{u}_2(x_1, x_2, x_3) + \varepsilon w_2(x_1, x_2, x_3, y_2, y_3) \\ u_3 &= \bar{u}_3(x_1, x_2, x_3) + \varepsilon w_3(x_1, x_2, x_3, y_2, y_3) \end{aligned} \quad (2.37)$$

where u_i and \bar{u}_i denote the displacement field of the original structure and the displacement field of the equivalent 3D model. w_i are the unknown fluctuating functions associated with the displacement field in each direction of coordinate system, x_i . Since we are constructing a homogenized model out of the original model, the kinematic fields in the homogenized model need to be defined in terms of the displacement field of the original model as:

$$\begin{aligned} \bar{u}_1 &= \langle u_1 \rangle \\ \bar{u}_2 &= \langle u_2 \rangle \\ \bar{u}_3 &= \langle u_3 \rangle \end{aligned} \quad (2.38)$$

The physical meaning of these definition is that the 3D displacements of the homogenized structure are the average of the original 3D displacements of the structure over the SG. The definition of the 3D displacement fields of the homogenized structure in Eq. (2.38), provides us with the necessary constraints on w_i which need to be imposed to solve the problem. The constraints are:

$$\langle w_i \rangle = 0 \quad (2.39)$$

where, it can be seen that these constraints removes the rigid body translations associated with the introduction of the fluctuating functions. We would also have to impose periodic boundary conditions along the y_2 and y_3 direction to respect the periodic nature of the SG.

The imposing of the periodic boundary condition makes sure that the rigid body rotation associated with the introduction of the fluctuating functions is also zero. Now substituting Eq. (2.37) into Eq. (2.12), we obtain the 3D displacement field in the local plate coordinate systems as:

$$\begin{aligned}
u_1^p &= \bar{u}_1 + \varepsilon w_1 \\
u_2^p &= \dot{y}_2 \bar{u}_2 + \dot{y}_3 \bar{u}_3 + \varepsilon \dot{y}_2 w_2 + \varepsilon \dot{y}_3 w_3 \\
u_3^p &= -\dot{y}_3 \bar{u}_2 + \dot{y}_2 \bar{u}_3 - \varepsilon \dot{y}_3 w_2 + \varepsilon \dot{y}_2 w_3
\end{aligned} \tag{2.40}$$

Since for the thin-walled 3D model we have, $u_i(x_1, x_2, x_3, y_2, y_3)$, the local plate strain terms definitions in Eq. (2.10) can be explicitly written as (using the partial derivative expression in Eq. (2.2)):

$$\begin{aligned}
\epsilon_{11}^p &= \frac{\partial u_1^p}{\partial x_1} \\
\epsilon_{22}^p &= \dot{y}_2 \frac{\partial u_2^p}{\partial x_2} + \dot{y}_3 \frac{\partial u_2^p}{\partial x_3} + \frac{1}{\varepsilon} \frac{\partial u_2^p}{\partial y_2^p} \\
2\epsilon_{12}^p &= \frac{\partial u_2^p}{\partial x_1} + \dot{y}_2 \frac{\partial u_1^p}{\partial x_2} + \dot{y}_3 \frac{\partial u_1^p}{\partial x_3} + \frac{1}{\varepsilon} \frac{\partial u_1^p}{\partial y_2^p} \\
\kappa_{11}^p &= -\frac{\partial^2 u_3^p}{\partial x_1^2} \\
\kappa_{22}^p &= -\left(\dot{y}_2^2 \frac{\partial^2 u_3^p}{\partial x_2^2} + \dot{y}_3^2 \frac{\partial^2 u_3^p}{\partial x_3^2} + 2\dot{y}_2 \dot{y}_3 \frac{\partial^2 u_3^p}{\partial x_2 \partial x_3} + 2\frac{\dot{y}_2}{\varepsilon} \frac{\partial}{\partial y_2^p} \left(\frac{\partial u_3^p}{\partial x_2} \right) + 2\frac{\dot{y}_3}{\varepsilon} \frac{\partial}{\partial y_2^p} \left(\frac{\partial u_3^p}{\partial x_3} \right) + \frac{1}{\varepsilon^2} \frac{\partial^2 u_3^p}{\partial (y_2^p)^2} \right) \\
2\kappa_{12}^p &= -2\frac{\partial}{\partial x_1} \left(\dot{y}_2 \frac{\partial u_3^p}{\partial x_2} + \dot{y}_3 \frac{\partial u_3^p}{\partial x_3} + \frac{1}{\varepsilon} \frac{\partial u_3^p}{\partial y_2^p} \right)
\end{aligned} \tag{2.41}$$

and then on inputting Eq. (2.40) into Eq. (2.41) we obtain the local plate strains in each segment as:

$$\begin{aligned}
\epsilon_{11}^p &= \Gamma_{11} + \underline{\varepsilon w_{1,1}} \\
\epsilon_{22}^p &= \dot{y}_2^2 \Gamma_{22} + \dot{y}_3^2 \Gamma_{33} + \dot{y}_2 \dot{y}_3 (2\Gamma_{23}) + \dot{y}_2 \dot{w}_2 + \dot{y}_3 \dot{w}_3 \\
&\quad + \underline{\varepsilon [\dot{y}_2^2 w_{2,2} + \dot{y}_3^2 w_{3,3} + \dot{y}_2 \dot{y}_3 (w_{2,3} + w_{3,2})]} \\
2\epsilon_{12}^p &= \dot{y}_2 (2\Gamma_{12}) + \dot{y}_3 (2\Gamma_{13}) + \dot{w}_1 + \underline{\varepsilon [\dot{y}_2 (w_{2,1} + w_{1,2}) + \dot{y}_3 (w_{1,3} + w_{3,1})]} \\
\kappa_{11}^p &= \underline{\dot{y}_3 \bar{u}_{2,11} - \dot{y}_2 \bar{u}_{3,11} + \varepsilon [\dot{y}_3 w_{2,11} - \dot{y}_2 w_{3,11}]} \\
\kappa_{22}^p &= \frac{1}{\varepsilon} (\dot{y}_3 \ddot{w}_2 - \dot{y}_2 \ddot{w}_3) \\
&\quad + \underline{\dot{y}_2^2 \dot{y}_3 \bar{u}_{2,22} - \dot{y}_3^2 \dot{y}_2 \bar{u}_{3,33} - \dot{y}_2^3 \bar{u}_{3,22} + \dot{y}_3^3 \bar{u}_{2,33} + 2\dot{y}_2 \dot{y}_3 (\dot{y}_3 \bar{u}_{2,23} - \dot{y}_2 \bar{u}_{3,23})} \\
&\quad + \varepsilon \left(\underline{\dot{y}_2^2 \dot{y}_3 w_{2,22} - \dot{y}_3^2 \dot{y}_2 w_{3,33} - \dot{y}_2^3 w_{3,22} + \dot{y}_3^3 w_{2,33} + 2\dot{y}_2 \dot{y}_3 (\dot{y}_3 w_{2,23} - \dot{y}_2 w_{3,23})} \right) \\
&\quad + 2 \left(\underline{\dot{y}_2 \dot{y}_3 \dot{w}_{2,2} - \dot{y}_2^2 \dot{w}_{3,2} + \dot{y}_3^2 \dot{w}_{2,3} - \dot{y}_3 \dot{y}_2 \dot{w}_{3,3}} \right) \\
2\kappa_{12}^p &= 2 \left(\underline{\dot{y}_2 \dot{y}_3 (\bar{u}_{2,21} - \bar{u}_{3,31}) - \dot{y}_2^2 (\bar{u}_{2,31} + \bar{u}_{3,21}) + \bar{u}_{2,31} + \dot{y}_3 \dot{w}_{2,1} - \dot{y}_2 \dot{w}_{3,1}} \right) \\
&\quad + 2\varepsilon \left(\underline{\dot{y}_2 \dot{y}_3 (w_{2,21} - w_{3,31}) - \dot{y}_2^2 (w_{2,31} + w_{3,21}) + w_{2,31}} \right)
\end{aligned} \tag{2.42}$$

where the 3D continuum strains $\epsilon = [\Gamma_{11} \quad \Gamma_{22} \quad \Gamma_{33} \quad 2\Gamma_{23} \quad 2\Gamma_{13} \quad 2\Gamma_{12}]^T$, are defined as:

$$\begin{aligned}
\Gamma_{11} &= \bar{u}_{1,1}, & \Gamma_{22} &= \bar{u}_{2,2}, & \Gamma_{33} &= \bar{u}_{3,3}, \\
2\Gamma_{23} &= \bar{u}_{3,2} + \bar{u}_{2,3}, & 2\Gamma_{13} &= \bar{u}_{3,1} + \bar{u}_{1,3}, & 2\Gamma_{12} &= \bar{u}_{1,2} + \bar{u}_{2,1}
\end{aligned} \tag{2.43}$$

in which Γ_{11} , Γ_{22} , and Γ_{33} are the normal strains in the three directions of the equivalent 3D model, $2\Gamma_{12}$, $2\Gamma_{23}$, and $2\Gamma_{13}$ are the shearing strains. Here again the underlined terms in the in-plane local plate strain terms are of order $O(\hat{\varepsilon}\varepsilon)$. And the underlined terms in the out-of-plane bending curvature terms are of order $O(\hat{\varepsilon}\varepsilon^2)$. On inputting this form of the plate strain terms into the overall strain energy we see that the contributions of the underlined terms to the overall energy is of order $O(\hat{\varepsilon}^2\varepsilon h^2)$, which is asymptotically smaller

than the contributions of the non-underlined terms which are of order $O(\hat{\epsilon}^2 h^2)$ and hence are dropped. After dropping off the asymptotically small terms, Eq. (2.42) can be written as:

$$\begin{aligned}
\epsilon_{11}^p &= \Gamma_{11} \\
\epsilon_{22}^p &= \dot{y}_2^2 \Gamma_{22} + \dot{y}_3^2 \Gamma_{33} + \dot{y}_2 \dot{y}_3 (2\Gamma_{23}) + \dot{y}_2 \dot{w}_2 + \dot{y}_3 \dot{w}_3 \\
2\epsilon_{12}^p &= \dot{y}_2 (2\Gamma_{12}) + \dot{y}_3 (2\Gamma_{13}) + \dot{w}_1 \\
\kappa_{11}^p &= 0 \\
\kappa_{22}^p &= \frac{1}{\varepsilon} (\dot{y}_3 \ddot{w}_2 - \dot{y}_2 \ddot{w}_3) \\
2\kappa_{12}^p &= 0
\end{aligned} \tag{2.44}$$

which can be written in matrix form as:

$$\epsilon^p = \mathbf{P}_0 \epsilon + \Gamma_h w^p \tag{2.45}$$

where,

$$\mathbf{P}_0 = \begin{bmatrix} 1 & 0 & 0 & 0 & 0 & 0 \\ 0 & \dot{y}_2^2 & \dot{y}_3^2 & \dot{y}_2 \dot{y}_3 & 0 & 0 \\ 0 & 0 & 0 & 0 & \dot{y}_3 & \dot{y}_2 \\ 0 & 0 & 0 & 0 & 0 & 0 \\ 0 & 0 & 0 & 0 & 0 & 0 \\ 0 & 0 & 0 & 0 & 0 & 0 \end{bmatrix} \tag{2.46}$$

and Γ_h and w^p remain the same as that of the MSG-TW beam and MSG-TW plate model, in Eq. (2.26) and Eq. (2.23).

Eq. (2.25), Eq. (2.35) and Eq. (2.45) have the same form with the only difference being in \mathbf{P}_0 and hence the same set of elements can be used to solve all the three models. As mentioned earlier, the SG is divided into individual segments that have their own parameterization of x_2^p and correspondingly y_2^p . Hence, at the junctions, it is required to have continuity conditions imposed.

2.6 Constraints and boundary conditions

As seen in Eq. (2.25), Eq. (2.35), and Eq. (2.45), the variables w_1^p and w_2^p have first-order derivatives with respect to y_2^p , hence just C^0 continuity condition at the junction of two intersecting segments has to be imposed on them. This continuity condition can be derived from the fact that u_1 and u_2 are continuous at the junction. The variable w_3^p has a second-order derivative in y_2^p , which implies that it requires C^1 continuity conditions at the junction, one of which can be derived from the fact that u_3 is continuous at the junction.

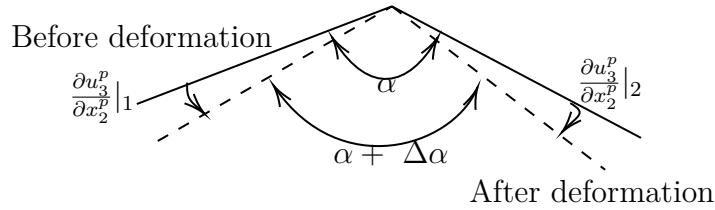


Figure 2.3. Slope continuity constraint $\Delta\alpha = 0$.

Another condition can be derived from using the fact that no change in angle would occur at the junctions due to shear effects, which can be imposed by the slope, i.e., $\frac{\partial u_3^p}{\partial x_2^p}$ being equal at the junctions which has been illustrated in Figure 2.3. An in-depth derivation of this boundary conditions, using position vectors, can be found in Appendix A. The above statements provide the following continuity conditions:

$$\begin{aligned} [u_i] &= 0 \\ \left[\frac{\partial u_3^p}{\partial x_2^p} \right] &= 0 \end{aligned} \quad (2.47)$$

where $[\cdot]$ refers to $(\cdot)_{(1)} - (\cdot)_{(2)}$ with (1) and (2) being the two intersecting members. The first continuity equation in Eq. (2.47) translates to the following continuity conditions on w_i in all models, including the beam model, plate model, and 3D solid model:

$$[w_i] = 0 \quad (2.48)$$

The second continuity equation in Eq. (2.47) translates to the following continuity conditions on w_i (after dropping small terms):

$$\begin{aligned}
& [\dot{y}_2 \dot{w}_3 - \dot{y}_3 \dot{w}_2 + \Phi] = 0 \quad \text{for a beam model} \\
& [\bar{u}_{3,2} - \dot{y}_2 \dot{y}_3 (\epsilon_{22} + \varepsilon y_3 \kappa_{22}) + \dot{y}_2 \dot{w}_3 - \dot{y}_3 \dot{w}_2] = 0 \quad \text{for a plate model} \\
& [\dot{y}_2 \dot{w}_3 - \dot{y}_3 \dot{w}_2 + \dot{y}_3 \dot{y}_2 (\Gamma_{33} - \Gamma_{22}) + \dot{y}_2^2 (2\Gamma_{23}) - \bar{u}_{2,3}] = 0 \quad \text{for a 3D structure}
\end{aligned} \tag{2.49}$$

Eq. (2.49) can further be written as (after removing constant terms):

$$\begin{aligned}
& [\theta^p] = [\bar{\theta}] = 0 \quad \text{for a beam model} \\
& [\theta^p - \dot{y}_2 \dot{y}_3 (\epsilon_{22} + \varepsilon y_3 \kappa_{22})] = [\bar{\theta}] = 0 \quad \text{for a plate model} \\
& [\theta^p + \dot{y}_3 \dot{y}_2 (\Gamma_{33} - \Gamma_{22}) + \dot{y}_2^2 (2\Gamma_{23})] = [\bar{\theta}] = 0 \quad \text{for a 3D structure}
\end{aligned} \tag{2.50}$$

here,

$$\theta^p = -\dot{y}_3 \dot{w}_2 + \dot{y}_2 \dot{w}_3 = \dot{w}_3^p$$

Overall constraints on the fluctuating functions (Eq. (2.15), Eq. (2.16), Eq. (2.29), and Eq. (2.39)) along with periodic boundary conditions on the corresponding edges (y_2 edges for the plate model, and y_2 and y_3 edges for the 3D structure) need to be imposed. It should be noted that this periodicity is imposed on w_i and $\bar{\theta}$ at the corresponding edges.

The strain energy density of the SG is written from Eq. (2.9) as:

$$U = \frac{1}{w} \left\langle \frac{1}{2} (\epsilon^p)^T K (\epsilon^p) \right\rangle \tag{2.51}$$

In Eq. (2.51), w denotes the volume of the domain spanned by y_i corresponding to the coordinates x_i remaining model. For the case of MSG TW beams, $w = 1$. For the case of MSG-TW plates, w is equal to the size of the SG along y_2 direction. For the case of MSG-TW 3D structures, w is equal to the area spanned by y_2 and y_3 .

The next step is to solve the Euler-Lagrange equation which is obtained from minimizing the functional in Eq. (2.51) subject to constraints in Eq. (2.15), Eq. (2.16), Eq. (2.29), and

Eq. (2.39). The finite element formulation used for solving the problem has been presented in the next section

2.7 Finite element implementation

The next step in the formulation is to solve for the unknown functions w_i by minimizing the functional in Eq. (2.51). As the line integral performed for the strain energy density in Eq. (2.51) is along every line segment, the shape functions have to be defined along (y_2^p, y_3^p) and the nodal variables transformed into (y_2, y_3) as is done in the case of frame elements [69]. The fluctuating functions w_i^p can be written in the form:

$$w^p(x_1, y_2(\xi), y_3(\xi)) = S(y_2(\xi), y_3(\xi)) V^p(x_1) \quad (2.52)$$

where ξ is the elemental coordinate system and runs from -1 to 1 while y_2^p runs from $-l_e/2$ to $l_e/2$, $\xi = 2y_2^p/l_e$, l_e being the length of the segment. y_2 and y_3 are functions of ξ in the following fashion:

$$y_2(\xi) = \frac{y_{22} - y_{21}}{2}\xi + \frac{y_{22} + y_{21}}{2}, \quad y_3(\xi) = \frac{y_{32} - y_{31}}{2}\xi + \frac{y_{32} + y_{31}}{2} \quad (2.53)$$

and $y_2 = \frac{y_{22}-y_{21}}{l_e}$, $y_3 = \frac{y_{32}-y_{31}}{l_e}$. Here the extremities of the segment are (y_{21}, y_{31}) and (y_{22}, y_{32}) . Each segment can be divided into one or more 1D elements. To ensure an exact solution for the fluctuating functions, quadratic elements with three nodes are used. Figure 2.4 shows a typical plate segment with its extremities and the corresponding 1D frame element and dofs. Every element has 12 dofs and the node numbering has also been shown in Figure 2.4. In Eq. (2.52), V^p takes the form as [69]:

$$V^p = \left[w_{11}^p \quad w_{21}^p \quad w_{31}^p \quad \theta_1^p \quad w_{12}^p \quad w_{22}^p \quad w_{32}^p \quad \theta_2^p \quad w_{13}^p \quad w_{23}^p \quad w_{33}^p \quad \theta_3^p \right]^T \quad (2.54)$$

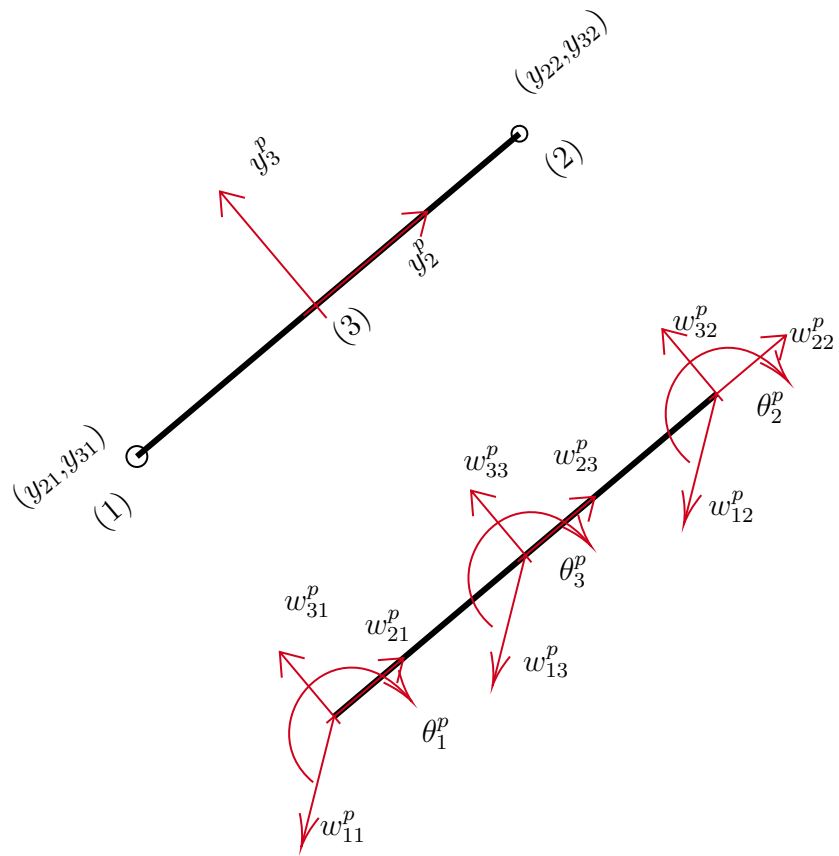


Figure 2.4. Elemental coordinates and dofs.

Here w_{ij}^p refers to the fluctuating function at the node j along direction i . Values of $i = (1, 2, 3)$ correspond to (x_1, y_2^p, y_3^p) respectively. θ_j^p refers to the rotation along x_1 direction at node j . $S[\xi]$ in Eq. (2.52) has the following form:

$$S[\xi] = \begin{bmatrix} N_1 & 0 & 0 & 0 & N_2 & 0 & 0 & 0 & N_3 & 0 & 0 & 0 \\ 0 & N_1 & 0 & 0 & 0 & N_2 & 0 & 0 & 0 & N_3 & 0 & 0 \\ 0 & 0 & \bar{N}_1 & \bar{M}_1 & 0 & 0 & \bar{N}_2 & \bar{M}_2 & 0 & 0 & \bar{N}_3 & \bar{M}_3 \end{bmatrix} \quad (2.55)$$

where

$$\begin{aligned} N_1 &= -\frac{(1-\xi)\xi}{2} & N_2 &= \frac{(1+\xi)\xi}{2} & N_3 &= 1 - \xi^2 \\ \bar{N}_1 &= \frac{3\xi^5}{4} - \frac{\xi^4}{2} - \frac{5\xi^3}{4} + \xi^2 & \bar{M}_1 &= \frac{l_e}{2} \left(\frac{\xi^5}{4} - \frac{\xi^4}{4} - \frac{\xi^3}{4} + \frac{\xi^2}{4} \right) \\ \bar{N}_2 &= -\frac{3\xi^5}{4} - \frac{\xi^4}{2} + \frac{5\xi^3}{4} + \xi^2 & \bar{M}_2 &= \frac{l_e}{2} \left(\frac{\xi^5}{4} + \frac{\xi^4}{4} - \frac{\xi^3}{4} - \frac{\xi^2}{4} \right) \\ \bar{N}_3 &= \xi^4 - 2\xi^2 + 1 & \bar{M}_3 &= \frac{l_e}{2} (\xi^5 - 2\xi^3 + \xi) \end{aligned} \quad (2.56)$$

These are the traditional quadratic Hermite polynomial shape functions which can be derived from the basic concept of the finite element method [70]. The nodal values, V^p , are in the (x_1, y_2^p, y_3^p) coordinate system and need to be transformed into the SG coordinate system, (x_1, y_2, y_3) , because the constraints in Eq. (2.15), Eq. (2.16), Eq. (2.29), Eq. (2.39), and Eq. (2.47) are imposed in that coordinate system. Hence we introduce a transformation matrix T [69], which is:

$$T = \begin{bmatrix} \tilde{\Omega} & [0]_{4 \times 4} & [0]_{4 \times 4} \\ [0]_{4 \times 4} & \tilde{\Omega} & [0]_{4 \times 4} \\ [0]_{4 \times 4} & [0]_{4 \times 4} & \tilde{\Omega} \end{bmatrix} \quad \tilde{\Omega} = \begin{bmatrix} 1 & 0 & 0 & 0 \\ 0 & \dot{y}_2 & \dot{y}_3 & 0 \\ 0 & -\dot{y}_3 & \dot{y}_2 & 0 \\ 0 & 0 & 0 & 1 \end{bmatrix} \quad (2.57)$$

and

$$V^p = TV^g \quad (2.58)$$

where V^g represents the nodal values in the (x_1, y_2, y_3) coordinate system. On substituting Eq. (2.58) into Eq. (2.52), w^p can be represented in terms of V^g and a new shape function matrix, \bar{S} [69], is obtained.

$$w^p = \bar{S}V^g \quad (2.59)$$

where,

$$\bar{S}[\xi] = \begin{bmatrix} N_1 & 0 & 0 & 0 & N_2 & 0 & 0 & 0 & N_3 & 0 & 0 & 0 \\ 0 & N_1\dot{y}_2 & N_1\dot{y}_3 & 0 & 0 & N_2\dot{y}_2 & N_2\dot{y}_3 & 0 & 0 & N_3\dot{y}_2 & N_3\dot{y}_3 & 0 \\ 0 & -\bar{N}_1\dot{y}_3 & \bar{N}_1\dot{y}_2 & \bar{M}_1 & 0 & -\bar{N}_2\dot{y}_3 & \bar{N}_2\dot{y}_2 & \bar{M}_2 & 0 & -\bar{N}_3\dot{y}_3 & \bar{N}_3\dot{y}_2 & \bar{M}_3 \end{bmatrix} \quad (2.60)$$

In order to ensure the continuity conditions in Eq. (2.50), a change of variable of V^g is introduced as:

$$V^g = \bar{V}^g + \alpha\epsilon \quad (2.61)$$

where

$$\alpha = \begin{bmatrix} [0]_{3 \times i} \\ \beta_1 \\ [0]_{3 \times i} \\ \beta_2 \\ [0]_{3 \times i} \\ \beta_3 \end{bmatrix}$$

and β_j depends on the global model under consideration. For the case of the beam model, $i = 4$.

$$\beta_j = [0 \quad 0 \quad 0 \quad 0]$$

For the case of the plate model $i = 6$.

$$\beta_j = \begin{bmatrix} 0 & \dot{y}_3\dot{y}_2 & 0 & 0 & \dot{y}_3\dot{y}_2x_3|_j & 0 \end{bmatrix}$$

For the case of 3D solid model $i = 6$.

$$\beta_j = \begin{bmatrix} 0 & \dot{y}_3 \dot{y}_2 & -\dot{y}_3 \dot{y}_2 & -\dot{y}_2^2 & 0 & 0 \end{bmatrix}$$

Here $x_3|_j$ represents the x_3 value of node j numbered in the local elemental system. On applying the transformations in Eq. (2.59) and Eq. (2.61), we get the following nodal variables:

$$\bar{V}^g = \left[w_{11} \quad w_{21} \quad w_{31} \quad \bar{\theta}_1 \quad w_{12} \quad w_{22} \quad w_{32} \quad \bar{\theta}_2 \quad w_{13} \quad w_{23} \quad w_{33} \quad \bar{\theta}_3 \right]^T \quad (2.62)$$

where, w_{ij} refers to the value of the fluctuating function at the node j along direction i . Values of $i = (1, 2, 3)$ correspond to (x_1, y_2, y_3) respectively. $\bar{\theta}_j$ refers to the value of $\bar{\theta}$ in Eq. (2.50) at node j .

The integral constraints are to be applied on w_i which can be represented in terms of w_i^p as:

$$\begin{Bmatrix} w_1 \\ w_2 \\ w_3 \end{Bmatrix} = \Omega^T \begin{Bmatrix} w_1^p \\ w_2^p \\ w_3^p \end{Bmatrix} \quad (2.63)$$

The integral constraints can be written in the following form:

$$\langle \Psi w_g \rangle = 0 \quad (2.64)$$

where $w_g = [w_1 \quad w_2 \quad w_3]^T$ and Ψ for the case of the beam model is:

$$\Psi = \begin{bmatrix} 1 & 0 & 0 \\ 0 & 1 & 0 \\ 0 & 0 & 1 \\ 0 & -y_3[\xi] & y_2[\xi] \end{bmatrix} \quad (2.65)$$

and for the case of the plate model and the equivalent 3D model is a 3×3 identity matrix. The Euler–Bernoulli beam model, the Kirchhoff–Love plate model, and the equivalent 3D model are obtained from the zeroth-order approximation of the strain energy [5], hence substituting Eq. (2.25) (or Eq. (2.35) or Eq. (2.45)), Eq. (2.52), and Eq. (2.58) in Eq. (2.51),

imposing the continuity conditions from Eq. (2.61), and the integral constraints in the form of Lagrange multiplier, the overall functional to be minimized is:

$$2U_0 = \bar{V}^T \mathbf{E} \bar{V} + 2\bar{V}^T \bar{\mathbf{D}}_{\mathbf{h}\epsilon} \epsilon + \epsilon^T \bar{\mathbf{D}}_{\epsilon\epsilon} \epsilon + \lambda^T \mathbf{D}_{\mathbf{h}\lambda} \bar{V} + \lambda^T \mathbf{F}_{\mathbf{h}\lambda} \epsilon \quad (2.66)$$

where \bar{V} contains the nodal values assembled from \bar{V}^g ; \mathbf{E} , $\bar{\mathbf{D}}_{\mathbf{h}\epsilon}$, $\bar{\mathbf{D}}_{\epsilon\epsilon}$, $\mathbf{D}_{\mathbf{h}\lambda}$, and $\mathbf{F}_{\mathbf{h}\lambda}$ are the global stiffness matrix, global forcing matrix, global contribution of \mathbf{P}_0 , global constraint matrix and its corresponding forcing matrix respectively which are:

$$\begin{aligned} \mathbf{E} &= \langle [\Gamma_h \bar{S}]^T K [\Gamma_h \bar{S}] \rangle \\ \bar{\mathbf{D}}_{\mathbf{h}\epsilon} &= \langle [\Gamma_h \bar{S}]^T K \mathbf{P}_0 + ([\Gamma_h \bar{S}]^T K [\Gamma_h \bar{S}]) \alpha \rangle \\ \bar{\mathbf{D}}_{\epsilon\epsilon} &= \langle \mathbf{P}_0^T K \mathbf{P}_0 + \alpha^T ([\Gamma_h \bar{S}]^T K [\Gamma_h \bar{S}]) \alpha + \alpha^T ([\Gamma_h \bar{S}]^T K \mathbf{P}_0) + (\mathbf{P}_0^T K [\Gamma_h \bar{S}]) \alpha \rangle \\ \mathbf{D}_{\mathbf{h}\lambda} &= \langle \Omega^T \bar{S} \rangle \\ \mathbf{F}_{\mathbf{h}\lambda} &= \langle (\Omega^T \bar{S}) \alpha \rangle \end{aligned} \quad (2.67)$$

Γ_h needs to be transformed into the elemental coordinate system as:

$$\Gamma_h = \begin{bmatrix} 0 & 0 & 0 \\ 0 & \frac{2}{l_e} \frac{d}{d\xi} & 0 \\ \frac{2}{l_e} \frac{d}{d\xi} & 0 & 0 \\ 0 & 0 & 0 \\ 0 & 0 & -\left(\frac{2}{l_e}\right)^2 \frac{d^2}{d\xi^2} \\ 0 & 0 & 0 \end{bmatrix} \quad (2.68)$$

The periodic boundary conditions can be imposed by setting the equality constraints on the periodic edges before solving the system of linear equations.

Taking the variation of Eq. (2.66) with respect to \bar{V} and λ and imposing the periodic boundary conditions, the following linear system of equations is obtained:

$$\begin{bmatrix} \mathbf{E} & (\bar{\mathbf{D}}_{\mathbf{h}\lambda})^T \\ \bar{\mathbf{D}}_{\mathbf{h}\lambda} & [0]_{3 \times 3} \end{bmatrix} \begin{Bmatrix} \bar{V} \\ \lambda \end{Bmatrix} = - \begin{bmatrix} \bar{\mathbf{D}}_{\mathbf{h}\epsilon} \\ \mathbf{F}_{\mathbf{h}\lambda} \end{bmatrix} \begin{Bmatrix} \epsilon \end{Bmatrix} \quad (2.69)$$

Eq. (2.69) is solved to find the solution for the zeroth-approximation of \bar{V}^g which is

$$\bar{V} = \hat{V}_0 \epsilon \quad (2.70)$$

Having solved for \bar{V}^g , the final stiffness matrix can be found by plugging it back into Eq. (2.66) and discarding the Lagrange multiplier term. The homogenized stiffness matrix $\bar{\mathbf{K}}$ is of the form:

$$\bar{\mathbf{K}} = \hat{V}_0^T \bar{\mathbf{D}}_{\mathbf{h}\epsilon} + \bar{\mathbf{D}}_{\epsilon\epsilon} \quad (2.71)$$

The zeroth-order approximation of the strain energy density for the homogenized beam model being:

$$\Pi_0 = \frac{1}{2} \epsilon^T \bar{\mathbf{K}} \epsilon = \frac{1}{2} \begin{pmatrix} \gamma_{11} \\ \kappa_1 \\ \kappa_2 \\ \kappa_3 \end{pmatrix}^T \begin{bmatrix} C_{11}^b & C_{12}^b & C_{13}^b & C_{14}^b \\ C_{12}^b & C_{22}^b & C_{23}^b & C_{24}^b \\ C_{13}^b & C_{23}^b & C_{33}^b & C_{34}^b \\ C_{14}^b & C_{24}^b & C_{34}^b & C_{44}^b \end{bmatrix} \begin{pmatrix} \gamma_{11} \\ \kappa_1 \\ \kappa_2 \\ \kappa_3 \end{pmatrix} \quad (2.72)$$

The zeroth-order approximation of the strain energy density for the homogenized plate model being:

$$\Pi_0 = \frac{1}{2} \epsilon^T \bar{\mathbf{K}} \epsilon = \frac{1}{2} \begin{pmatrix} \epsilon_{11} \\ \epsilon_{22} \\ 2\epsilon_{12} \\ \kappa_{11} \\ \kappa_{22} \\ 2\kappa_{12} \end{pmatrix}^T \begin{bmatrix} A_{11} & A_{12} & A_{16} & B_{11} & B_{12} & B_{16} \\ A_{12} & A_{22} & A_{26} & B_{21} & B_{22} & B_{26} \\ A_{16} & A_{26} & A_{66} & B_{61} & B_{62} & B_{66} \\ B_{11} & B_{21} & B_{61} & D_{11} & D_{12} & D_{16} \\ B_{12} & B_{22} & B_{62} & D_{12} & D_{22} & D_{26} \\ B_{16} & B_{26} & B_{66} & D_{16} & D_{26} & D_{66} \end{bmatrix} \begin{pmatrix} \epsilon_{11} \\ \epsilon_{22} \\ 2\epsilon_{12} \\ \kappa_{11} \\ \kappa_{22} \\ 2\kappa_{12} \end{pmatrix} \quad (2.73)$$

The zeroth-order approximation of the strain energy density for the homogenized 3D solid model being:

$$\Pi_0 = \frac{1}{2} \epsilon^T \bar{\mathbf{K}} \epsilon = \frac{1}{2} \left\{ \begin{array}{c} \Gamma_{11} \\ \Gamma_{22} \\ \Gamma_{33} \\ 2\Gamma_{23} \\ 2\Gamma_{13} \\ 2\Gamma_{12} \end{array} \right\}^T \left[\begin{array}{cccccc} C_{11} & C_{12} & C_{13} & C_{14} & C_{15} & C_{16} \\ C_{12} & C_{22} & C_{23} & C_{24} & C_{25} & C_{26} \\ C_{13} & C_{23} & C_{33} & C_{34} & C_{35} & C_{36} \\ C_{14} & C_{24} & C_{34} & C_{44} & C_{45} & C_{46} \\ C_{15} & C_{25} & C_{35} & C_{45} & C_{55} & C_{56} \\ C_{16} & C_{26} & C_{36} & C_{46} & C_{56} & C_{66} \end{array} \right] \left\{ \begin{array}{c} \Gamma_{11} \\ \Gamma_{22} \\ \Gamma_{33} \\ 2\Gamma_{23} \\ 2\Gamma_{13} \\ 2\Gamma_{12} \end{array} \right\} \quad (2.74)$$

3. RESULTS

For validation, the theory proposed has been implemented into a computer code called MSG thin-walled (MSG-TW). Multiple examples have been presented, which have geometric and material complexity associated with them. The results have been compared with existing literature and equivalent properties obtained from MSG solid model. As MSG solid model uses the 3D strain energy without the thin-walled approximation, the results obtained from it have been used as the benchmark [71].

3.1 Equivalent beam properties

For the case of beam properties, in order to showcase the versatility of MSG-TW, we have presented two different choices of reference lines, MSG-TW (Centric), and MSG-TW (Off-Centric), for cases which can have both. MSG-TW (Centric) obtains results by choosing the center of the segment as the reference line (a partially populated plate stiffness matrix) and MSG-TW (Off-Centric) obtains results by choosing a reference line which does not correspond to the center of the segment (a completely populated plate stiffness matrix)

3.1.1 Isotropic strip

The first example is an isotropic strip with width c and thickness h . The material properties are E the Young's modulus and ν the Poisson's ratio. This example is chosen to show that MSG-TW can obtain beam properties for trivial cases. The set of equations obtained can be solved in an analytical fashion without the use of FEM mentioned previously, yielding analytical expression for the stiffness properties which are:

$$C_{11}^b = Ech \quad C_{22}^b = \frac{Ech^3}{6(1+\nu)} \quad C_{33}^b = \frac{Ech^3}{12} \quad C_{44}^b = \frac{Ec^3h}{12} \quad (3.1)$$

The geometric properties have been presented in Figure 3.1 and the results from the MSG-TW code are shown in Table 3.1, where the material properties have the following values: $E = 68.9$ GPa, $\nu = 0.33$, $c = 10$ cm and $h = 0.5$ cm.

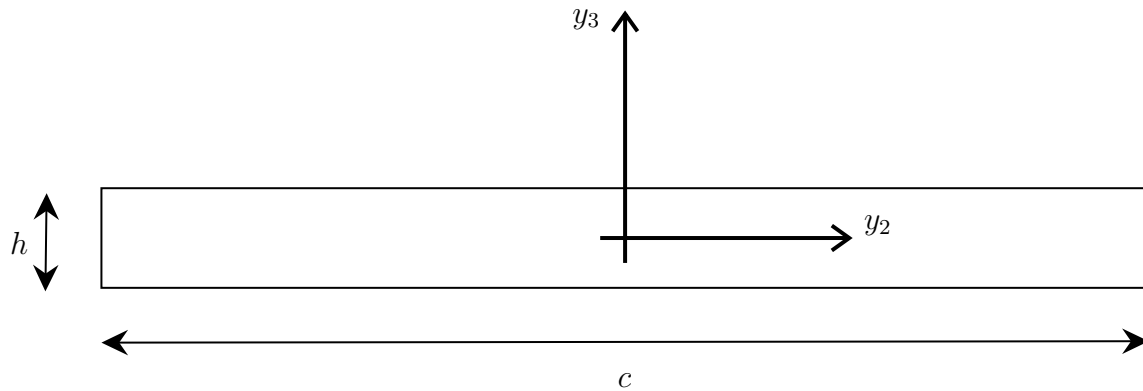


Figure 3.1. Isotropic Strip.

Table 3.1. Stiffness value for an isotropic strip section: (a) MSG-TW (Centric), (b) Harursampath et al. [20], (c) Yu et al. [18], and (d) MSG solid.

Stiffness	(a)	(b)	(c)	(d)
$C_{11}^b (10^7 \text{N})$	3.445	3.445	3.445	3.445
$C_{22}^b (\text{Nm}^2)$	107.926	107.926	107.926	107.657
$C_{33}^b (\text{Nm}^2)$	71.770	71.770	71.770	71.770
$C_{44}^b (10^4 \text{Nm}^2)$	2.871	2.871	2.871	2.871

Table 3.2. Stiffness value for an isotropic I-section: (a) MSG-TW (Centric), (b) MSG-TW (Off-Centric), (c) Harursampath et al. [20], (d) Yu et al. [18], and (e) MSG solid.

Stiffness	(a)	(b)	(c)	(d)	(e)
$C_{11}^b (10^8 \text{N})$	2.067	1.998	2.067	2.067	1.998
$C_{22}^b (10^3 \text{Nm}^2)$	2.590	2.562	7.732	2.590	2.550
$C_{33}^b (10^5 \text{Nm}^2)$	4.031	3.875	3.875	4.031	3.875
$C_{44}^b (10^5 \text{Nm}^2)$	1.154	1.153	1.153	1.154	1.153

The results show good agreement with MSG solid for all cases and the analytical expression obtained can be found in a typical solid mechanics textbook. For performing the sectional analysis in the proposed finite element method, 1 element with 3 nodes was used and each node having 4 dofs which is computationally cheap in comparison to MSG solid where 5 2D quadratic elements were used with a total of 28 nodes and each node having 3 dofs.

3.1.2 Isotropic I-section

The next example is an isotropic I-section with the flange and the web having length, $c = 10$ cm and thickness $h = 1$ cm and having material properties $E = 68.9$ GPa and $\nu = 0.33$. The sectional properties obtained have been shown in Table 3.2 as MSG-TW (Centric).

Errors associated with the values are significant in comparison to MSG solid which can be attributed to the choice of the reference line. Such theories should converge to the original value as the thickness decreases (c/h increases) which can be seen in the convergence trend plotted in Figure 3.2. As the aspect ratio (c/h) increases the value converges to the original value but even at an aspect ratio of 1/40, the value of C_{33}^b still has an error close to 2%.

These errors are mainly due to the choice of the reference line of the plate segment. For the case of MSG-TW (Centric) as shown in Figure 3.3, the red arrows show the directions along which the laminate is stacked in the original 3D structure. It can be seen the shaded areas are being added twice which causes more errors in C_{33}^b than in C_{44}^b . This is because the double counted area has a smaller area moment of inertia in the y_2 direction than that

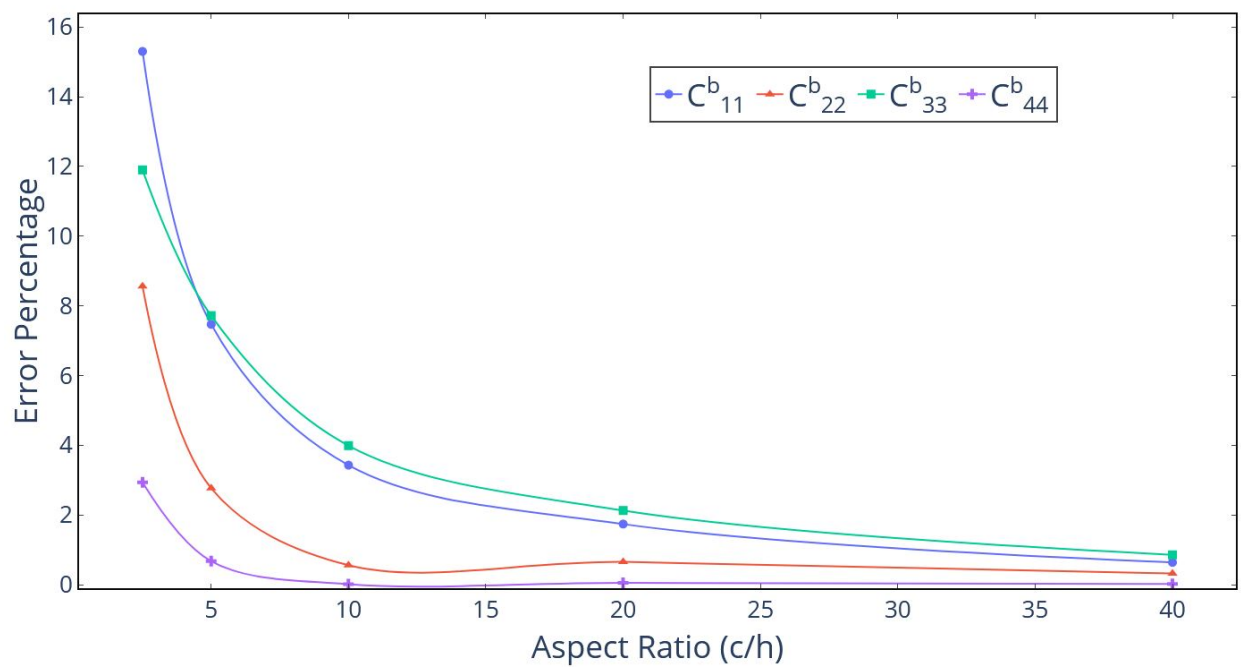


Figure 3.2. Convergence study of isotropic I-section.

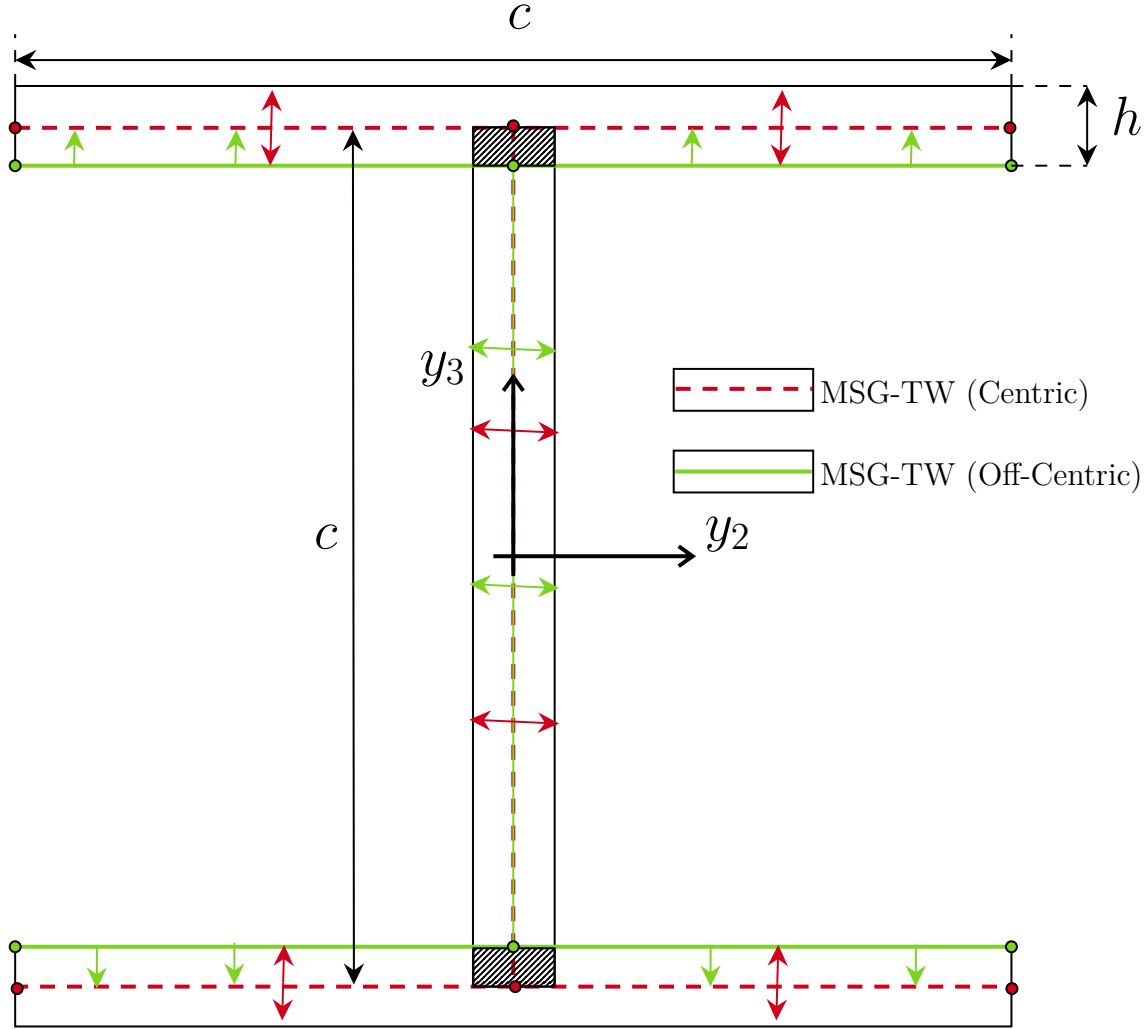


Figure 3.3. Overlaps in an isotropic I-section.

in y_3 direction. As seen in Table 3.2 in MSG-TW (Off-Centric), the results improve a lot in comparison to MSG-TW (Off-Centric). This is because no overlapping is present as seen by the green arrows in Figure 3.3. This off-centric choice of reference line leads to a completely populated plate stiffness matrix for each segments except the web.

3.1.3 Anisotropic I-section

The next example is a composite I-section which has been extensively studied in the literature and can provide a benchmark comparison for the formulation. The anisotropic I-section presented in [72] has been used as it has been compared in other works [19], [20].

The schematic of the section is shown in Figure 3.4. The material properties used have been

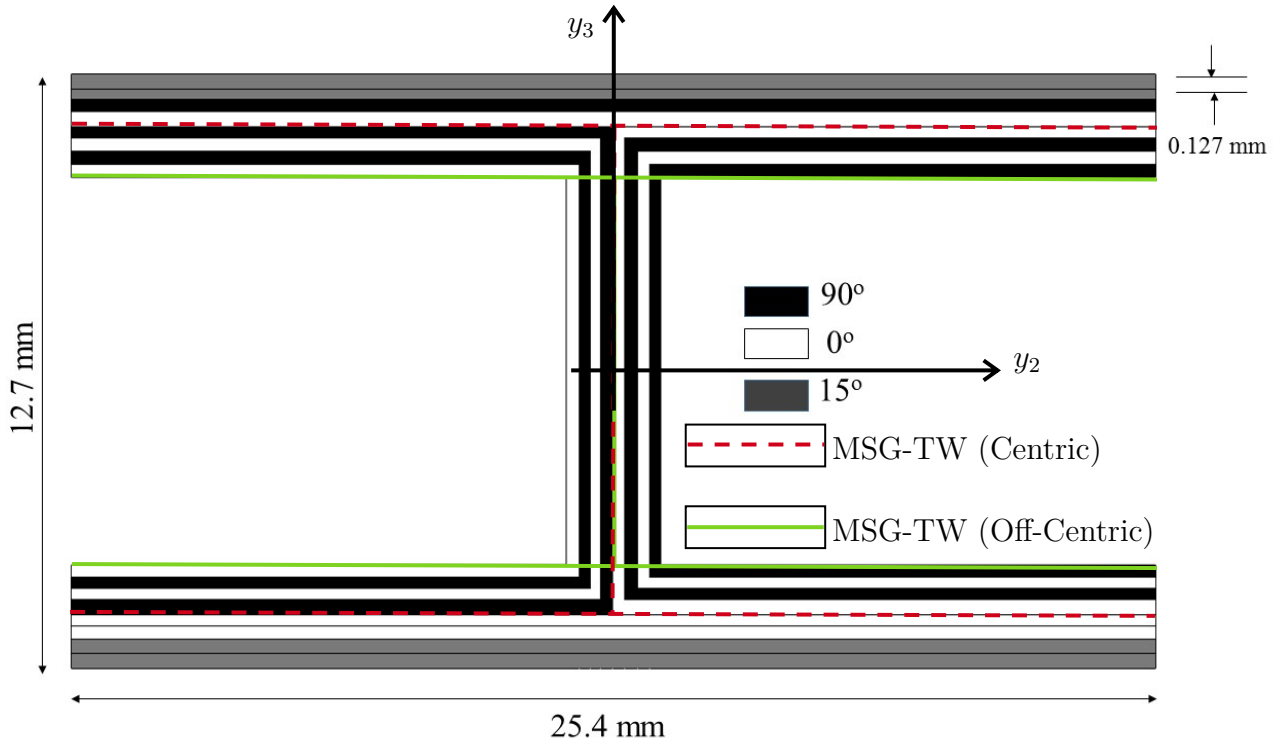


Figure 3.4. Thin-walled anisotropic I section.

obtained from [72] as

$$E_1 = 141.963 \text{ GPa}, \quad E_2 = E_3 = 9.79 \text{ GPa},$$

$$G_{12} = G_{13} = G_{23} = 6.136 \text{ GPa}, \quad \nu_{12} = \nu_{13} = \nu_{23} = 0.42$$

The explicit orientations of the layers, in the (y_2, y_3) coordinate system, at different sections are

- Right side top flange: $[(90^\circ/0^\circ)_3 / (15^\circ)_2]$
- Left side top flange: $[(0^\circ/90^\circ)_3 / (15^\circ)_2]$
- Right side bottom flange: $[(90^\circ/0^\circ)_3 / (15^\circ)_2]$
- Left side bottom flange: $[(0^\circ/90^\circ)_3 / (15^\circ)_2]$

- Web: $[(90^\circ/0^\circ)_4]$

The layers are 0.127 mm thick and the total height and the width of the section are 12.7 mm and 25.4 mm respectively. The ratio of the height of each segment to the cross-sectional dimensions is small which qualifies it as a thin-walled section. The results obtained from using MSG-TW beam model are compared with the previous works in Table 3.3 and are in better agreement with MSG solid, in comparison to [20]. Chandra et al. [72] assumes that the in-plane axial strain along x_2^p , ϵ_{22} , vanish. The results obtained are more stiffer in comparison to other methods. It should be noted the results of MSG-TW (Centric) are exactly the same as [19]. Here as well, the choice of reference line reflects the error associated with the final results and it can be seen a careful choice of off-centric reference lines can provide better results in comparison to keeping the center lines as the reference lines.

Table 3.3. Stiffness value for an anisotropic I section: (a) MSG-TW(Centric),(b) MSG-TW(Off-Centric) (c) Harursampanth et al. [20], (d) Chandra et al. [72], and (e) MSG solid.

Stiffness	(a)	(b)	(c)	(d)	(e)
$C_{11}^b(10^6\text{N})$	5.134	5.055	5.133	5.525	5.022
$C_{14}^b(\text{Nm})$	65.347	60.975	15.072	0.000	56.887
$C_{22}^b(\text{Nm}^2)$	0.178	0.176	0.178	0.193	0.177
$C_{33}^b(\text{Nm}^2)$	155.475	153.000	154.540	153.937	152.290
$C_{44}^b(\text{Nm}^2)$	227.226	227.219	227.146	248.526	225.120

For performing the sectional analysis in MSG solid, 3,792 2D quadratic elements were used with a total of 12,341 nodes and each node having 3 dofs. In contrast, for performing the sectional analysis using the current approach, 8 1D elements were used to obtain the plate stiffness matrices for the 5 different segments in the cross-section and 5 1D elements were used, with each element having 3 nodes and each node having 4 dofs.

A clear computational advantage can be seen of the current approach over MSG solid, and as seen from the sectional properties calculated in Table 3.3, it is in better agreement as compared to existing thin-walled beam theories. The current theory also captures the axial-bending coupling (C_{14}^b) which was not being captured in [72] and less accurate in [20].

3.1.4 Circular tube

The next example is a composite circular tube. This example showcases the ability of MSG-TW to obtain the effective beam properties of a cross-sections which have an inherent curvature associated with their reference lines. The schematic of the circular tube has been shown in Figure 3.5. The analytical solution to the cross-sectional properties considering that

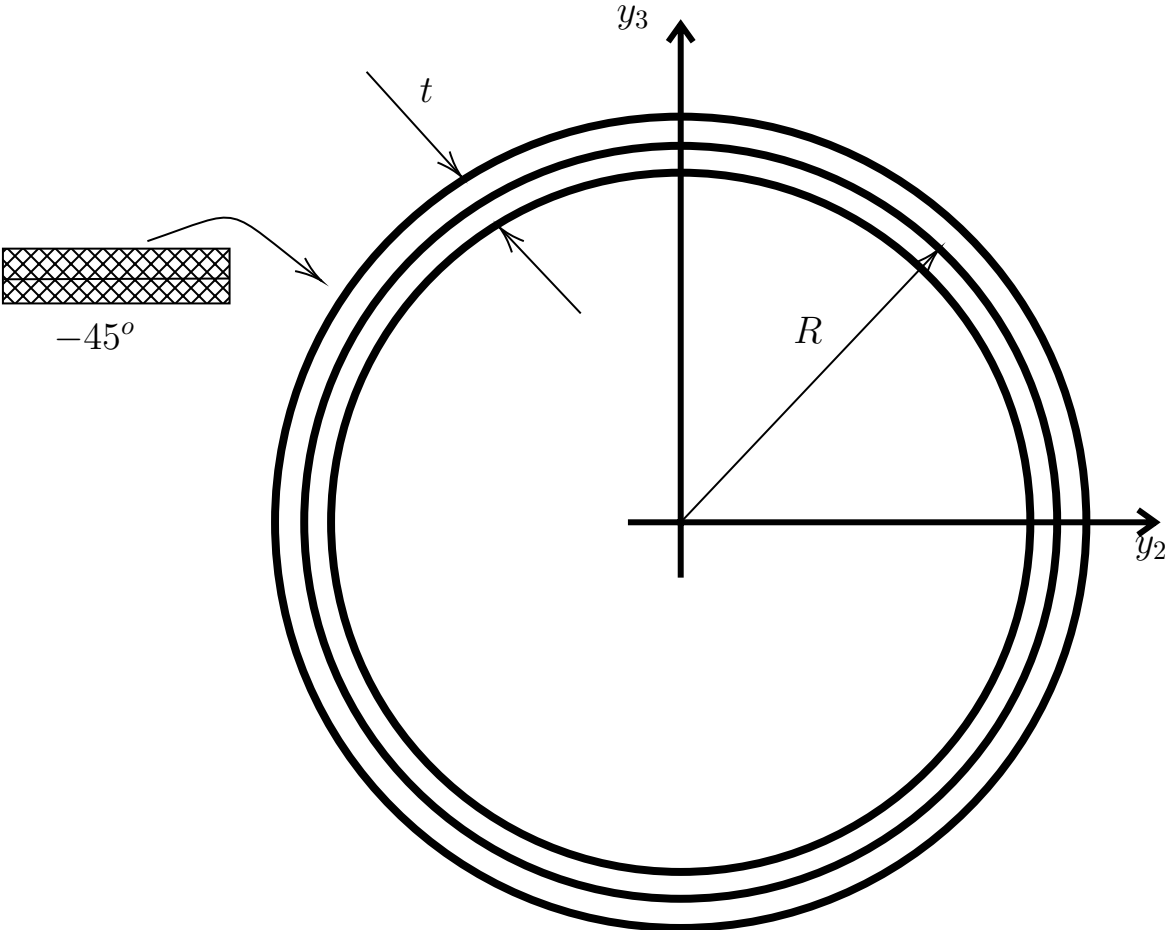


Figure 3.5. Thin-walled composite circular tube section.

Table 3.4. Stiffness value for an isotropic I-section: (a) MSG-TW (Centric), (b) Yu et al. [18], and (c) MSG solid.

Stiffness	(a)	(b)	(c)
$C_{11}^b (10^7 \text{N})$	4.7727	4.7729	4.7738
$C_{12}^b (10^5 \text{Nm})$	-9.3591	-9.3607	-9.3906
$C_{22}^b (10^5 \text{Nm}^2)$	1.4943	1.4903	1.4932
$C_{33}^b (10^5 \text{Nm}^2)$	1.0705	1.0728	1.0741

the tube section is made of a single shell can be explicitly obtained from the formulation presented in [18] and written as:

$$\begin{aligned}
C_{11}^b &= 2\pi R \left(A_{11} - \frac{A_{16}^2}{A_{66}} \right) \\
C_{12}^b &= \frac{\pi R}{A_{66}} (-3B_{62}A_{16} - 2RA_{16}A_{26} + 3B_{12}A_{66} + 2RA_{12}A_{66}) \\
C_{22}^b &= \frac{\pi R}{2A_{66}} \left(-3B_{26}(3B_{62} + 2RA_{26}) + 9D_{22}A_{66} - 6R(B_{62}A_{26} - 2B_{22}A_{66}) - 4R^2(A_{26}^2 - A_{22}A_{66}) \right) \\
C_{33}^b &= C_{44}^b = \frac{\pi R}{\mathbb{Z}} \left(\Delta_D + 2R\mathbb{A} + R^2\mathbb{B} - 2R^3\mathbb{C} - R^4\mathbb{D} + 4R^5\mathbb{E} + 4R^6\Delta_A \right)
\end{aligned} \tag{3.2}$$

The complete derivations and the expanded expressions for Δ_D , \mathbb{A} , \mathbb{B} , \mathbb{C} , \mathbb{D} , \mathbb{E} and Δ_A are presented in Appendix B. From Eq. (3.2), it can be seen that a circular tube with a single type of composite layup has tension-torsion coupling associated with it. So in order to showcase the capability of MSG-TW to capture this effect a single ply composite layup is chosen which has a fiber angle of -45° and the material properties associated with the ply is:

$$\begin{aligned}
E_1 &= 37 \quad \text{GPa}, & E_2 &= E_3 = 9 \quad \text{GPa}, \\
G_{12} &= G_{13} = G_{23} = 4 \quad \text{GPa}, & \nu_{12} &= \nu_{13} = \nu_{23} = 0.28.
\end{aligned}$$

The sectional properties obtained for the case of $R = 7.15$ cm and $t = 8.682$ mm have been shown in Table 3.4. Here we have only presented C_{33}^b , as for the case of a circular tube, $C_{33}^b = C_{44}^b$. We can see that, MSG-TW model is able to capture the tension-torsion coupling terms with high degree of accuracy.

As seen for the case of the Isotropic I section, the error percentage of the beam properties with respect to MSG solid model decreases as the aspect ratio of $2R/t$ increases. This

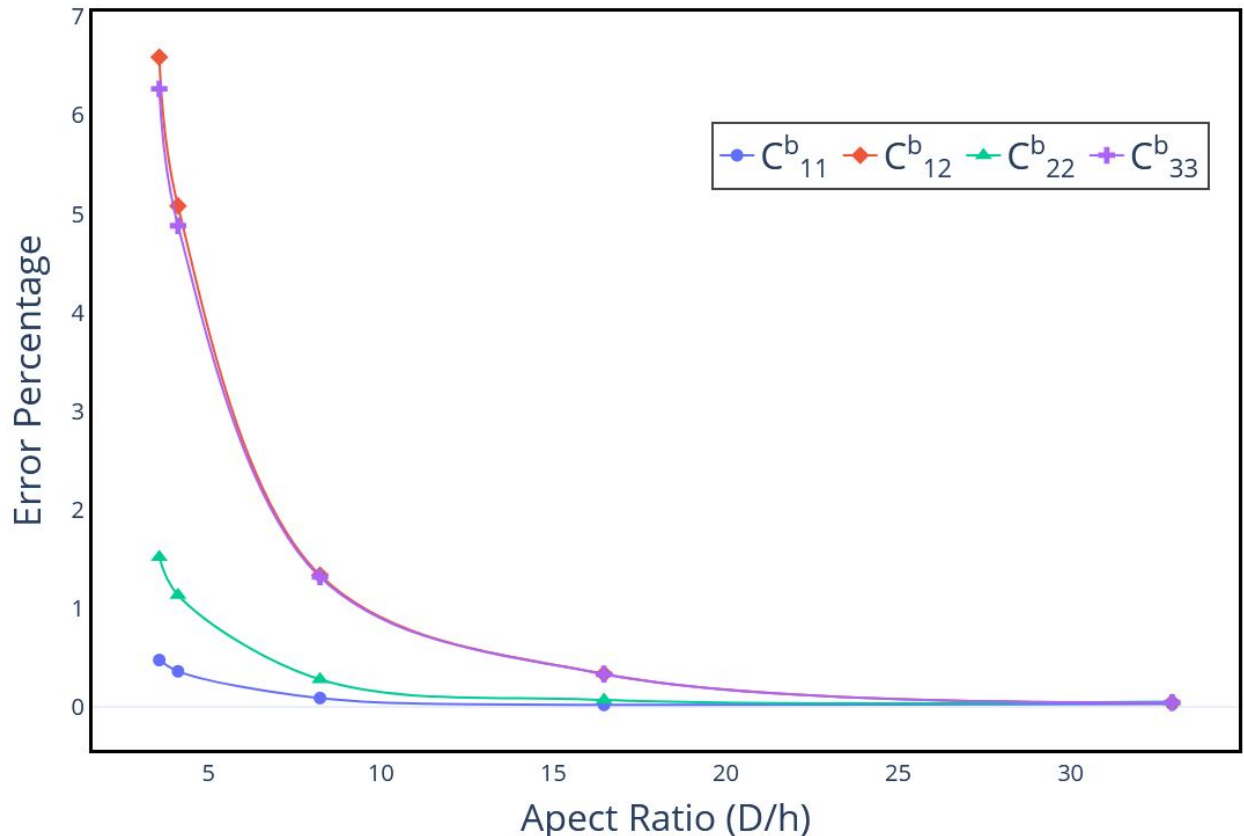


Figure 3.6. Convergence study of composite circular tube with respect to aspect ratio.

convergence trend can be seen in Figure 3.6. Since MSG-TW utilizes straight segments to capture the curvature effects of a shell, we can see in Figure 3.7 that as we increase the number of segments to describe the geometry of the shell, the difference between the numerical and analytical values decreases. This plot was made keeping the values of $R = 7.15$ cm and $t = 8.682$ mm. This supports the claim that we can indeed represent a curved geometry with sufficient straight line segments.

For performing the sectional analysis in MSG solid, 2880 2D quadratic elements were used with a total of 6120 nodes and each node having 3 dofs. In contrast, for performing the sectional analysis using the current approach, 1 1D elements was used to obtain the plate stiffness matrix and 200 1D elements were used to obtain the results in Table 3.4, with each element having 3 nodes and each node having 4 dofs.

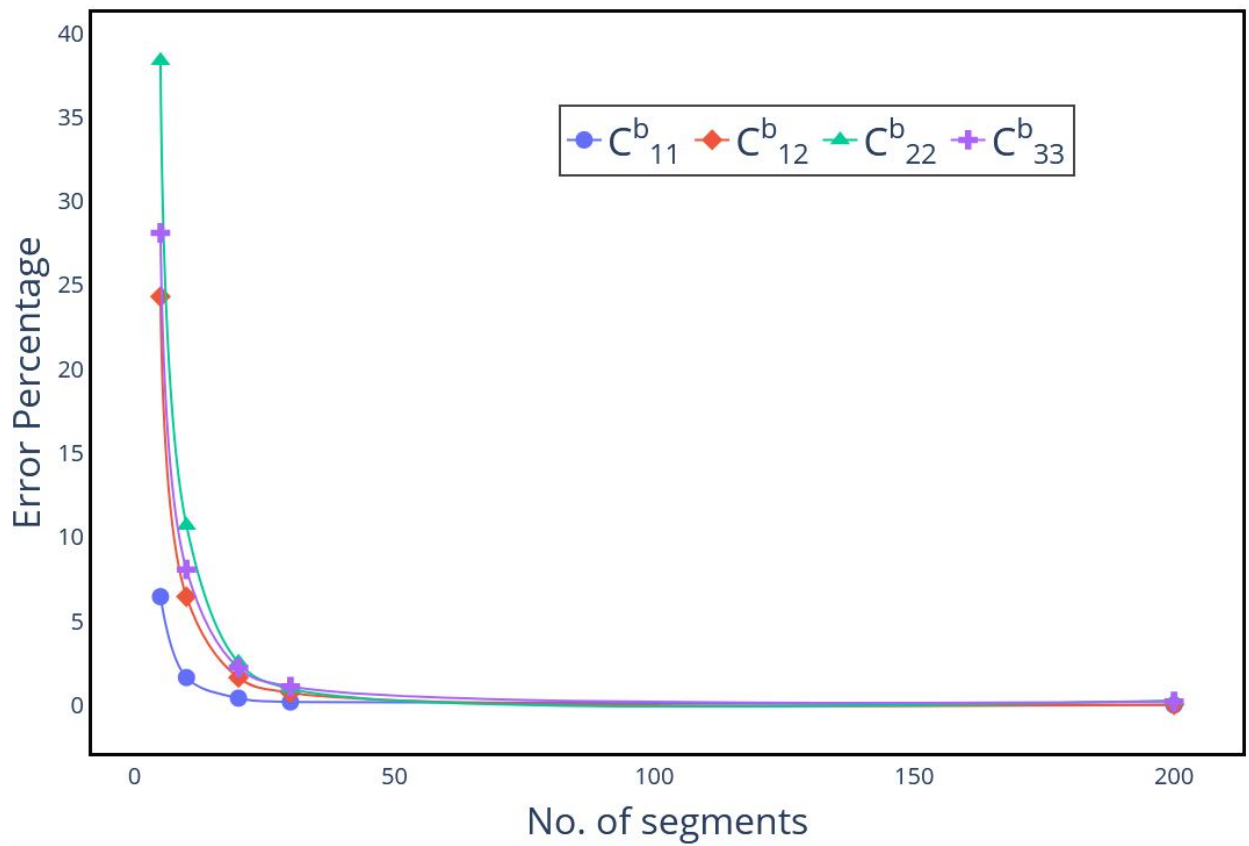


Figure 3.7. Convergence study of composite circular tube with respect to number of segments.

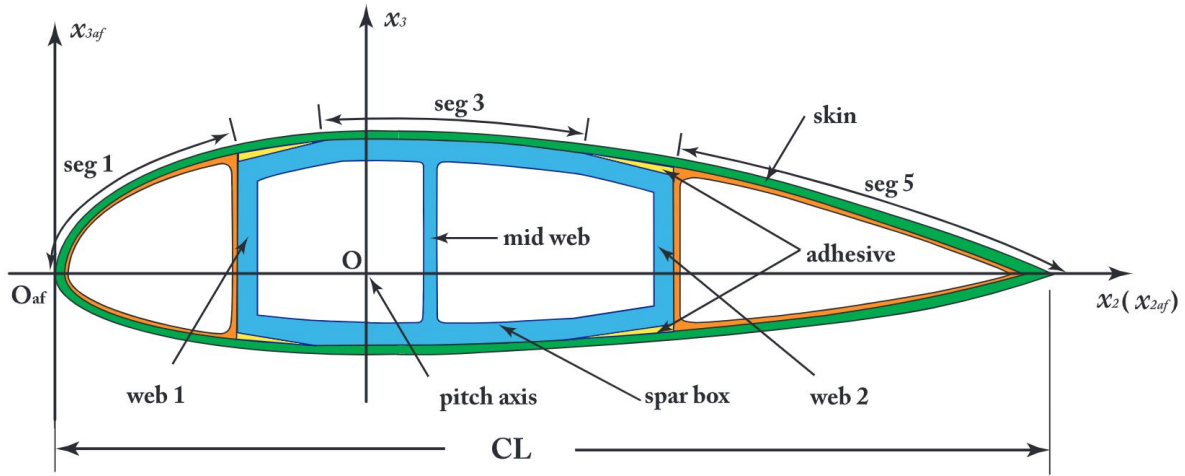


Figure 3.8. Realistic composite wind turbine multi-cell section [73].

3.1.5 Realistic wind turbine blade section

The next example is a realistic composite wind turbine blade with five varying skin segments and two webs. This example has been taken from [73]. The schematic of a typical wind turbine blade is shown in Figure 3.8 and the corresponding reference line used for MSG-TW (Off-Centric) in Figure 3.9. An MH 104 airfoil is used and the cross-sectional details such as chord length, the web location, the y_2 coordinates of representative points for defining the skin segments as well as the material properties and orientation have been taken from [73].

The lamination properties used for this example are the “Laminate layer schema for station 1” mentioned in [73]. The only differences between the current example and the one mentioned in [73] are the laminate thickness of each layer and origin of the coordinate system. The thickness of all the layers are all 5 times smaller than that in [73] and the origin is kept at \mathbf{O}_{af} .

The reference line chosen in the current example is the outside of the skin segments which automatically means a MSG-TW (Off-centric) model is used. The results obtained have been compared with MSG solid in Table 3.5. It can be seen here that the beam stiffness is completely populated and the MSG-TW can capture all the diagonal as well as the

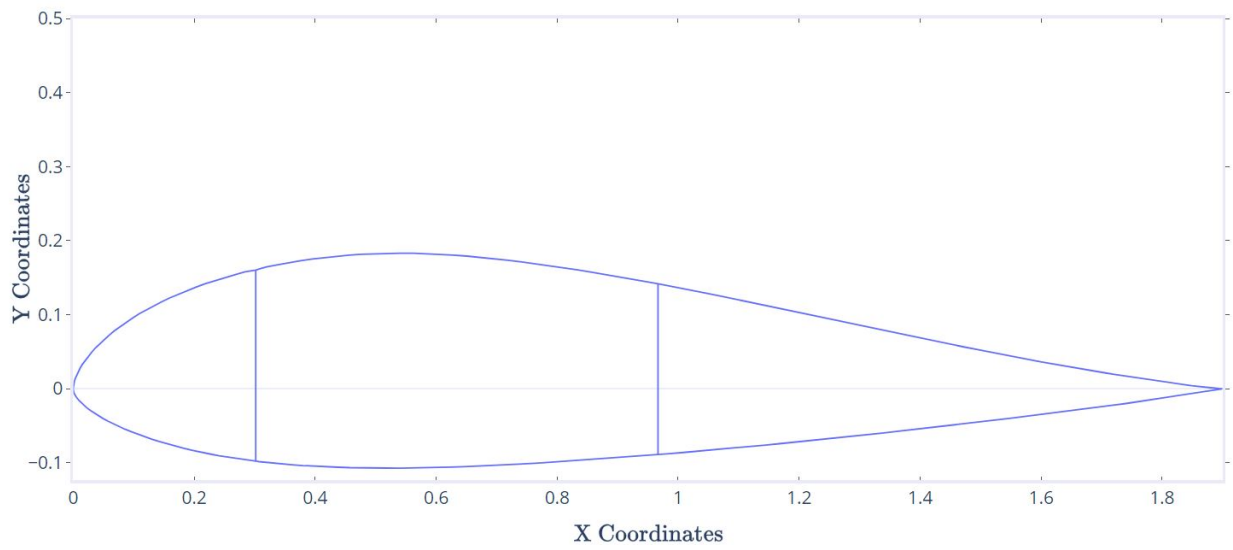


Figure 3.9. MSG-TW model for realistic composite wind turbine multi-cell section [73].

coupling terms to a reasonable amount of accuracy with the maximum difference being in C_{24}^b (bending-torsion coupling), which is 7.69 %. Although MSG-TW induces an error in the beam stiffness components in comparison to MSG solid, the enormous computational savings achieved make MSG-TW more useful in critical applications such as preliminary design of the cross-section.

Table 3.5. Stiffness value for realistic wind turbine blade section: (a) MSG solid (b) MSG-TW(Off-Centric), and (c) Error %.

Stiffness	(a)	(b)	(c)
$C_{11}^b(10^8\text{N})$	5.48	5.68	3.59
$C_{12}^b(10^6\text{Nm})$	-8.28	-8.76	5.83
$C_{13}^b(10^7\text{Nm})$	1.60	1.65	3.29
$C_{14}^b(10^8\text{Nm})$	3.89	4.03	3.73
$C_{22}^b(10^6\text{Nm}^2)$	6.02	6.12	1.6
$C_{23}^b(10^5\text{Nm}^2)$	-3.45	-3.60	4.56
$C_{24}^b(10^6\text{Nm}^2)$	4.73	5.09	7.69
$C_{33}^b(10^6\text{Nm}^2)$	6.46	6.68	3.49
$C_{34}^b(10^6\text{Nm}^2)$	-9.58	-9.89	3.37
$C_{44}^b(10^8\text{Nm}^2)$	3.63	3.78	4.09

For performing the sectional analysis in MSG solid, 11,023 2D linear elements were used with a total of 20,207 nodes and each node having 3 dofs. In contrast, for performing the sectional analysis using MSG-TW, a maximum of 5 1D elements were used to obtain the plate stiffness matrices for the 5 different segments in the cross-section and 128 1D elements were used, with each element having 3 nodes and each node having 4 dofs.

3.1.6 Isotropic multi-cell box section

The final beam example is an isotropic multi-cell box section. This showcases the application of MSG-TW to more than two cells which has been already presented in [26] but because of the analytical nature of the work generalization of the theory was not easy. MSG-TW works for more than two cells which are oriented in any arbitrary direction inside the box beam. The material properties used for the example are the same as used for the previous isotropic cases and a schematic diagram of the beam cross-section has been shown in Figure 3.10. The results obtained have been compared with MSG solid in Table 3.6.

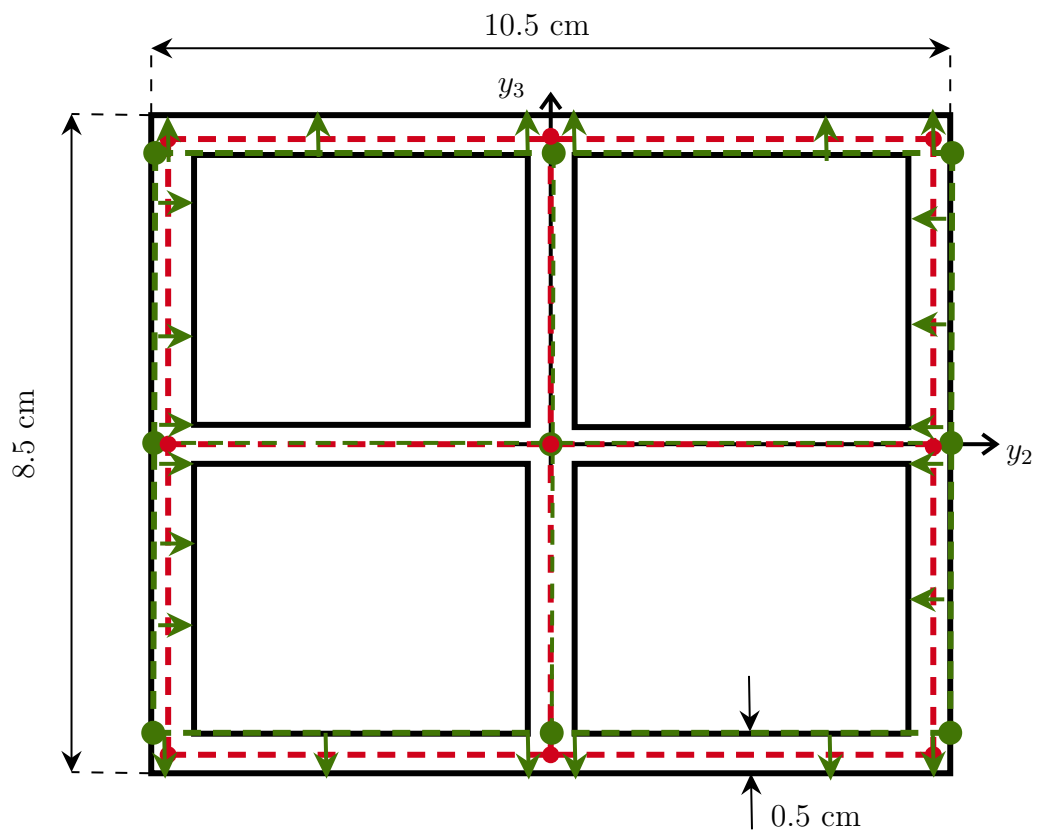


Figure 3.10. Isotropic multi-cell section.

Table 3.6. Stiffness value for an isotropic multi-cell section: (a) MSG-TW (Centric), (b) MSG solid, and (c) Error %.

Stiffness	(a)	(b)	(c)
$C_{11}^b (10^8 \text{N})$	1.86	1.81	2.92
$C_{22}^b (10^4 \text{Nm}^2)$	9.52	9.55	0.3
$C_{33}^b (10^5 \text{Nm}^2)$	1.55	1.52	1.54
$C_{44}^b (10^5 \text{Nm}^2)$	2.24	2.20	1.73

For performing the sectional analysis in MSG solid, 2,885 2D linear elements were used with a total of 3,354 nodes and each node having 3 dofs. In contrast, for performing the sectional analysis using MSG-TW, 1 1D elements was used to obtain the plate stiffness matrices for the segment in the cross-section and 12 1D elements were used, with each element having 3 nodes and each node having 4 dofs.

3.2 Equivalent plate properties

As done for the beam model, MSG-TW plate model also considers the off-centric reference lines and the effects of this consideration are more staggering for the case of the plate model as some results cannot be obtained by using centric reference lines which are assumed by most method in the literature.

3.2.1 Isotropic corrugated plate

The first example is an isotropic corrugated plate, the dimensions and material properties of the SG has been shown in Figure 3.11. This example has been studied in [27] and [44]. Xia et al. [27] and Ye and Yu [44] provide analytical expressions for the equivalent plate properties and are more computationally advantageous than MSG-TW but due to the choice of local plate stiffness matrix in [27] and isotropic material in [44] they cannot be applied to general cases. This example is chosen to show that MSG-TW can obtain values for simple cases.

The non-zero components of the equivalent plate stiffness matrix obtained are presented in Table 3.7. It can be seen that MSG-TW provides results as accurate as the results obtained from [27] and [44]. The stiffness properties associated with bending in both directions (D_{11} ,

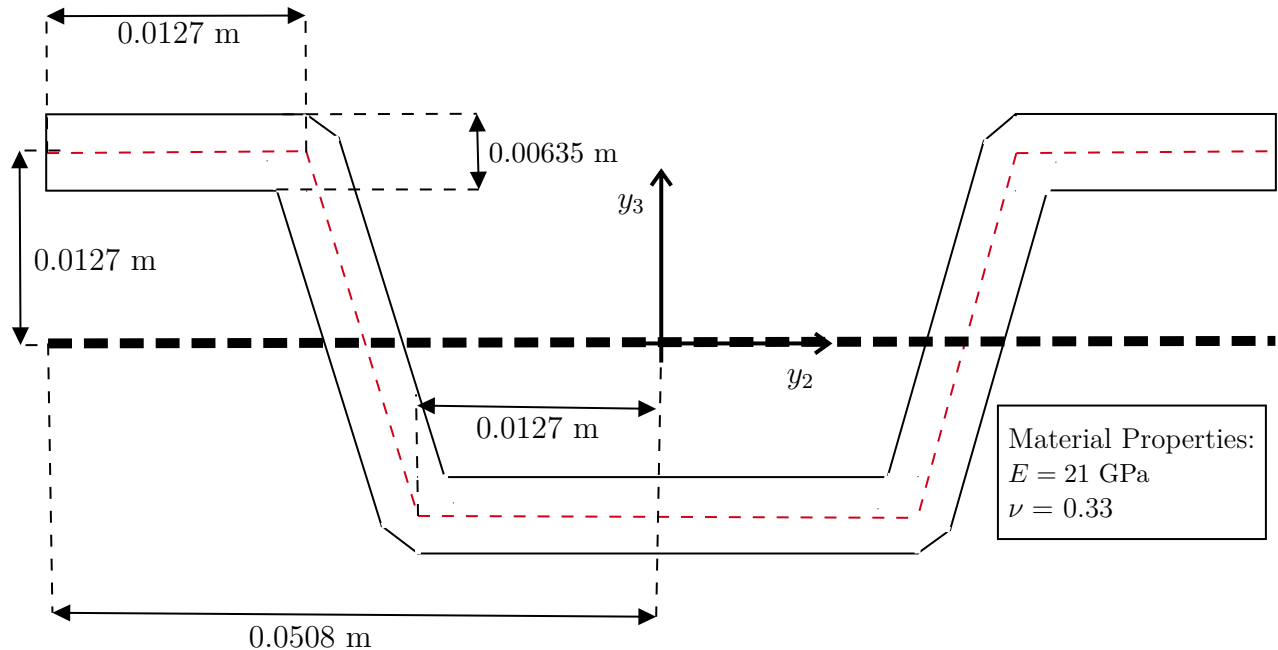


Figure 3.11. Isotropic corrugated plate.

D_{12} and D_{22}) are very close to the values obtained by the MSG solid and in [44] it has been shown that these values replicate the original deformation of the structure to a high degree of accuracy. The values obtained for the in-plane stiffness properties along the corrugation (A_{22} and A_{12}) have a 2% difference from the values obtained in [44]. This difference is because in [44], the author has missed a constant while obtaining Eq. (52) from Eq. (50) in [44] and this constant relates to ϵ_{22} . In order to perform the analysis using MSG-TW, 5 elements with 3 nodes each were used and each node having 4 dofs which is computationally much cheaper in comparison to MSG solid model where 881 2D quadratic elements were used with a total of 2,884 nodes and each node having 3 dofs.

3.2.2 Isotropic corrugated panel (with irregular thickness)

The next example is an isotropic corrugated panel as shown (along with the material used) in Figure 3.12, the results of which have also been presented in [2]. This particular example presents the case of having a discontinuity in the plate reference line if the center of the segment is chosen as the reference line (as can be seen by the red dotted line in

Table 3.7. Equivalent plate properties for an isotropic corrugated plate: (a) MSG-TW, (b) Xia et al. [27], (c) Ye et al. [44] and (d) MSG solid.

Stiffness	(a)	(b)	(c)	(d)
A_{11} (MN/m)	161.332	161.332	161.479	160.91
A_{12} (MN/m)	1.215	1.216	1.245	1.380
A_{22} (MN/m)	4.052	4.052	4.150	4.173
A_{66} (MN/m)	42.488	42.489	42.489	42.278
D_{11} (KN·m)	16.242	17.809	16.251	16.473
D_{12} (N·m)	122.375	122.375	122.375	138.34
D_{22} (N·m)	407.913	407.917	407.917	419.21
D_{66} (N·m)	208.033	208.032	208.033	203.94

Figure 3.3. The analytical methods adopted in [27] and [44] cannot deal with this situation because these methods decouple the extension and bending behaviour for isotropic plates, which translates to the center of the segment being the reference line.

MSG-TW can tackle this case by having an off-centric reference line as shown by the green dotted lines in Figure 3.12 because a completely populated plate stiffness can be considered in MSG-TW.

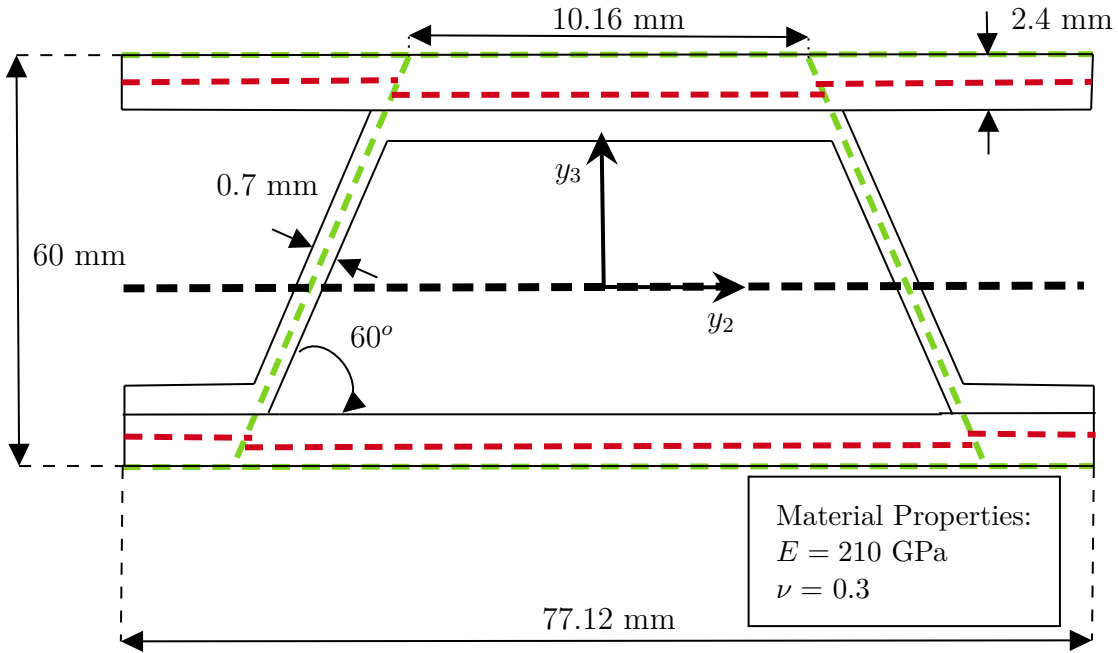


Figure 3.12. Isotropic corrugated panel (with irregular thickness).

Buannic et al. [2] obtains the results by performing an RVE analysis using plate elements and a 3D RVE. The results obtained from MSG-TW have been compared with [2] and also with MSG solid in Table 3.8, where (E_1^m, E_2^m, G_{12}^m) are the membrane moduli and (E_1^f, E_2^f, G_{12}^f) are the bending moduli. Here 2 is the direction of the corrugation. It should be noted that instead of comparing the plate stiffness matrix, the membrane and bending moduli have been compared for this case as presented in [2]. The results obtained are close to the ones obtained from MSG solid. The value obtained for the membrane moduli in the corrugation direction (E_2^m) by the present method is more accurate than the one obtained in [2].

Table 3.8. Membrane and bending moduli for an isotropic corrugated panel (a) MSG-TW, (b) Buannic et al. [2] and (c) MSG solid.

Moduli	(a)	(b)	(c)
E_1^m (GPa)	209.77	208.1	208.98
E_2^m (GPa)	256.55	252.8	257.09
G_{12}^m (GPa)	83.596	84.54	84.27
ν_{12}^m	0.245	0.2469	0.2434
E_1^f (10^3 GPa)	82.61	81.91	81.199
E_2^f (10^3 GPa)	87.44	88.20	89.09
G_{12}^f (10^3 GPa)	32.074	31.68	31.851
ν_{12}^f	0.274	0.2786	0.2767

In order to perform the analysis using MSG-TW, 8 elements with 3 nodes each were used and each node having 4 dofs which is computationally much cheaper in comparison to MSG solid where 3,143 2D quadratic elements were used with a total of 10,531 nodes and each node having 3 dofs. Buannic et al. [2] used 26 2D quadratic plate elements with a total of 130 nodes which is computationally more expensive than the current method.

3.2.3 Anisotropic corrugated plate

The final example is an anisotropic corrugated plate, the geometry of which has been shown in Figure 3.13. This particular example has been presented in [74], where an analytical approach is used to obtain the equivalent plate properties. All the segments associated with

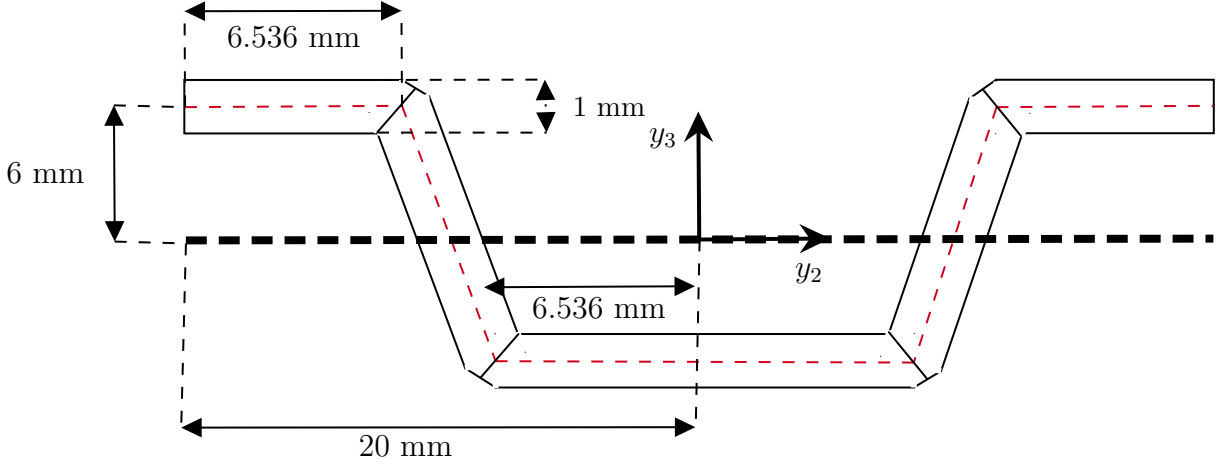


Figure 3.13. Anisotropic corrugated sheet.

this SG have the same layup sequence which is $[\pm 45]_{2s}$ and the material used has the following properties:

$$\begin{aligned}
 E_1 = E_3 = 10.5 \quad \text{GPa}, \quad E_2 = 148 \quad \text{GPa}, \quad G_{12} = G_{23} = 5.61 \quad \text{GPa}, \\
 G_{13} = 3.17 \text{GPa}, \quad \nu_{12} = 0.0213, \quad \nu_{13} = 0.59, \quad \nu_{23} = 0.3
 \end{aligned}$$

The non-zero components of the equivalent plate stiffness matrix obtained are presented in Table 3.9. The stiffness values associated with the bending modes obtained by using MSG-TW are close to the values obtained via MSG solid. MSG-TW is able to capture the bending-torsion stiffness components (D_{16} and D_{26}) which were not being captured in [74]. D_{11} is more accurately captured by MSG-TW than [74]. The model presented in [74] assumes the bending-torsion stiffness terms at the SG level as zero, i.e., D_{16} and D_{26} are zero, which is avoided in the present work.

The in-plane components, especially the off-diagonal terms A_{12} , A_{16} and A_{26} , show deviation from the values obtained via the MSG solid model. These terms are close to what has been obtained in [74]. This difference can be attributed to the in-plane components having contribution from transverse shear deformation of each segment. Since these terms are neglected in CLPT, we see a discrepancy in the results. It is believed that if a higher-order

Table 3.9. Equivalent plate properties for an anisotropic corrugated sheet: (a) MSG-TW, (b) Park et al. [74] and (c) MSG solid.

Stiffness	(a)	(b)	(c)
A_{11} (MN/m)	26.688	26.684	26.543
A_{12} (MN/m)	93.539	92.023	51.393
A_{16} (MN/m)	0	0	-19
A_{22} (MN/m)	122.881	120.819	112.633
A_{26} (MN/m)	0	0	22.9
A_{66} (MN/m)	28.43	28.442	28.138
D_{11} (KN·m)	0.633	1.5	0.632
D_{12} (N·m)	2.218	2.219	2.91
D_{16} (N·m)	1.081	0	1.29
D_{22} (N·m)	2.913	2.914	2.76
D_{62} (N·m)	1.081	0	0.998
D_{66} (N·m)	4.297	4.297	4.18

plate theory like the Reissner-Mindlin (RM) theory is used to represent the strain energy associated with the SG, the results will be more accurate.

To validate the existence of the bending-torsion coupling terms in the equivalent plate stiffness matrix, a direct numerical simulation (DNS) was performed on a large corrugated plate with dimensions much larger than the SG and compared with an equivalent plate (of the same dimensions) for which plate properties were the ones presented in Table 3.9. The mode shapes associated with the fundamental frequency was obtained from this analysis and the mode shapes can be seen in Figure 3.14. The values of the fundamental frequencies obtained from the various models are:

- DNS: 10.901 Hz
- MSG: 10.752 Hz
- MSG-TW: 10.947 Hz
- Park et al. [74]: 12.714 Hz

As seen in Figure 3.14a, the mode shape obtained from the DNS is that of a coupled bending-torsion one, which is captured by the equivalent plate models associated with MSG solid model and MSG-TW but the mode shape obtained from the equivalent plate model

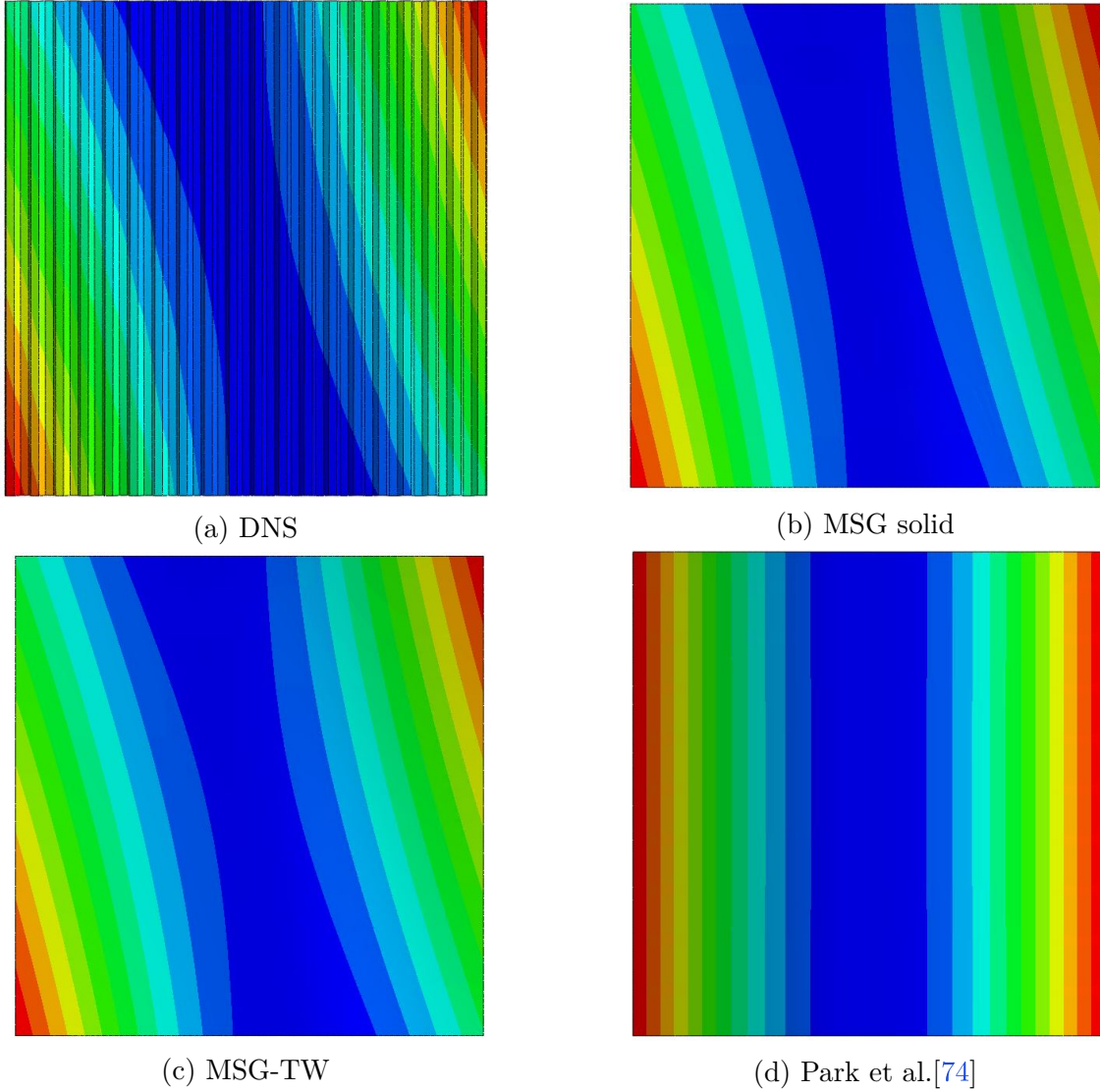


Figure 3.14. Mode shape corresponding to fundamental frequency of the plate.

associated with Park et al. [74] is that of a pure bending one. This shows that the bending-torsion coupling exists and it is captured by MSG solid and MSG-TW.

In order to perform the analysis using MSG-TW, 5 elements with 3 nodes each were used and each node having 4 dofs which is computationally much cheaper in comparison to MSG solid where 32,020 2D quadratic elements were used with a total of 98,261 nodes and each node having 3 dofs.

3.3 Equivalent 3D properties

For the case of equivalent 3D properties, as done for the case of beam and plates multiple examples have been presented to showcase the versatility of MSG-TW. These examples have been compared with existing literature results.

3.3.1 Isotropic cellular solid with varying flange angle

The first example is an isotropic honeycomb like cellular solid (Figure 1.5), the SG and the associated geometric parameters of which have been shown in Figure 3.15. This example has been presented in [52], [64], and [55]. Depending on the angle θ , in Figure 3.15, the SG can give rise to a hexagonal lattice ($\theta > 0$), a square lattice ($\theta = 0$) or a re-entrant lattice ($\theta < 0$).

The models in [52], [64], and [55] provide analytical expressions for the equivalent 2D properties and are more computationally advantageous than MSG-TW but due to the choice of defining every segment as a beam they are unable to provide out-of-plane properties associated with the structure. These models only consider isotropic material properties and hence cannot be applied to general cases. The model in [62] uses a numerical approach but chooses to define every segment as a beam and hence has the same shortcomings as [52], [64], and [55].

The variation of the in-plane properties obtained using the proposed method with respect to the angle θ , keeping the values of other geometric parameters as constants is presented in Figures 3.16 - 3.19. In the example, $l = 10$ cm, $h = 10$ cm and $t = 0.5$ cm. The material used in the example is aluminium which has Young's modulus, $E = 68.9$ Gpa, and Poisson's ratio, $\nu = 0.33$.

The in-plane properties in Figures 3.16 - 3.19 have also been compared with [52], [55], [62], and the MSG solid model. The model proposed in Gibson and Ashby [52] only considers the bending energy associated with the individual segments but as the value of angle θ moves close zero, the different segments have a stretching dominant behaviour in comparison to bending and hence, a singularity is observed in the model for the value of equivalent Young's modulus in x_2 direction (Figure 3.16) at zero value of θ . The values of equivalent Young's

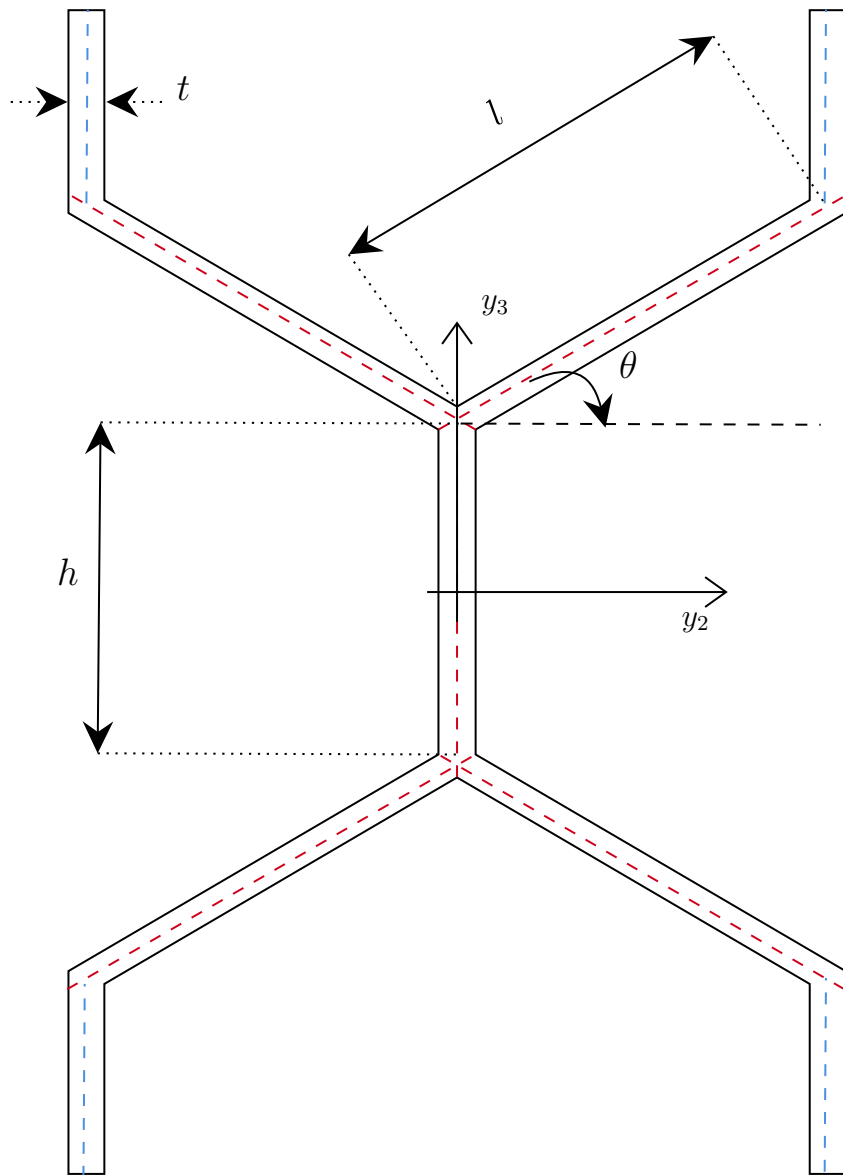


Figure 3.15. Cellular solid structure.

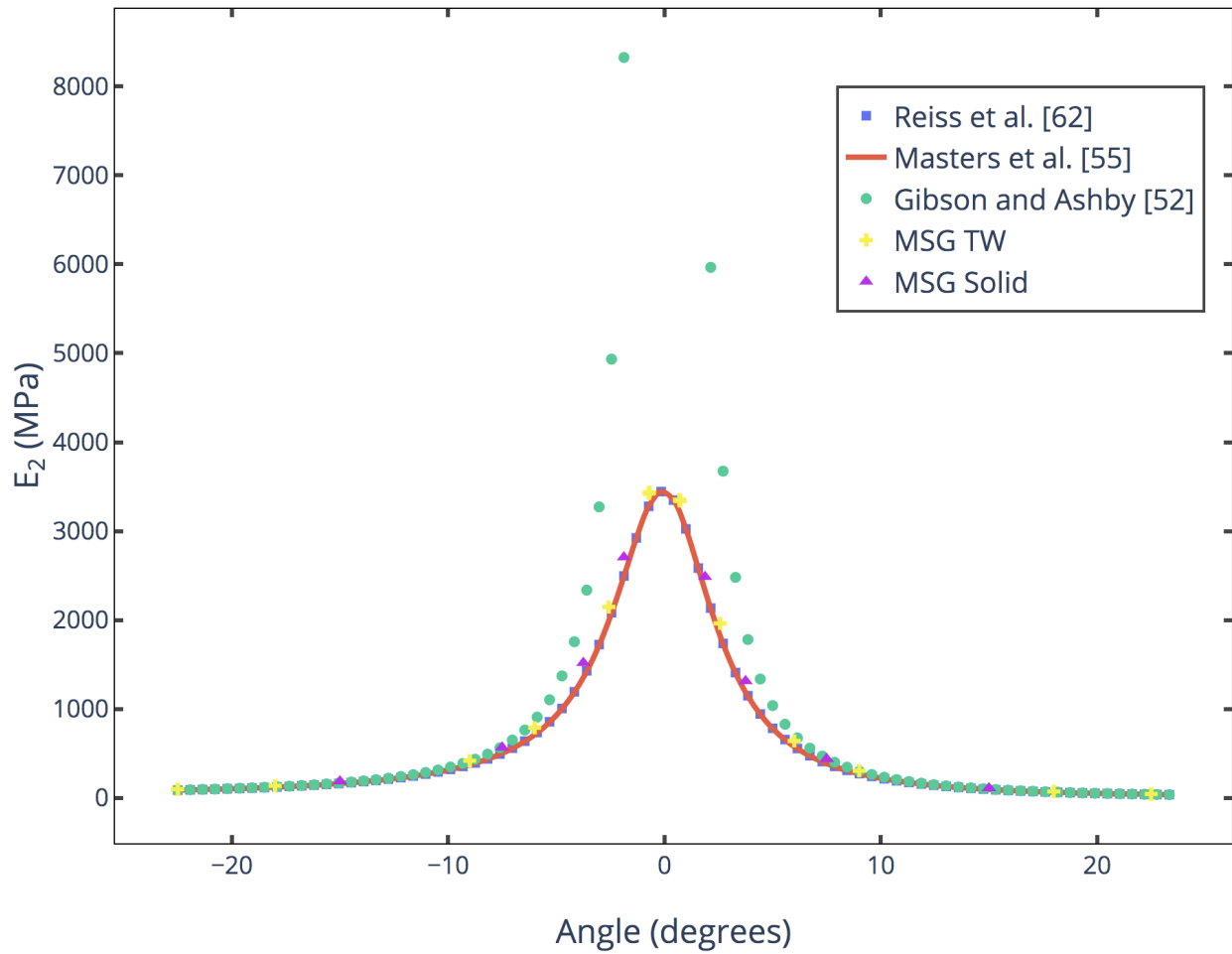


Figure 3.16. Equivalent Young's modulus of a cellular solid structure in x_2 direction.

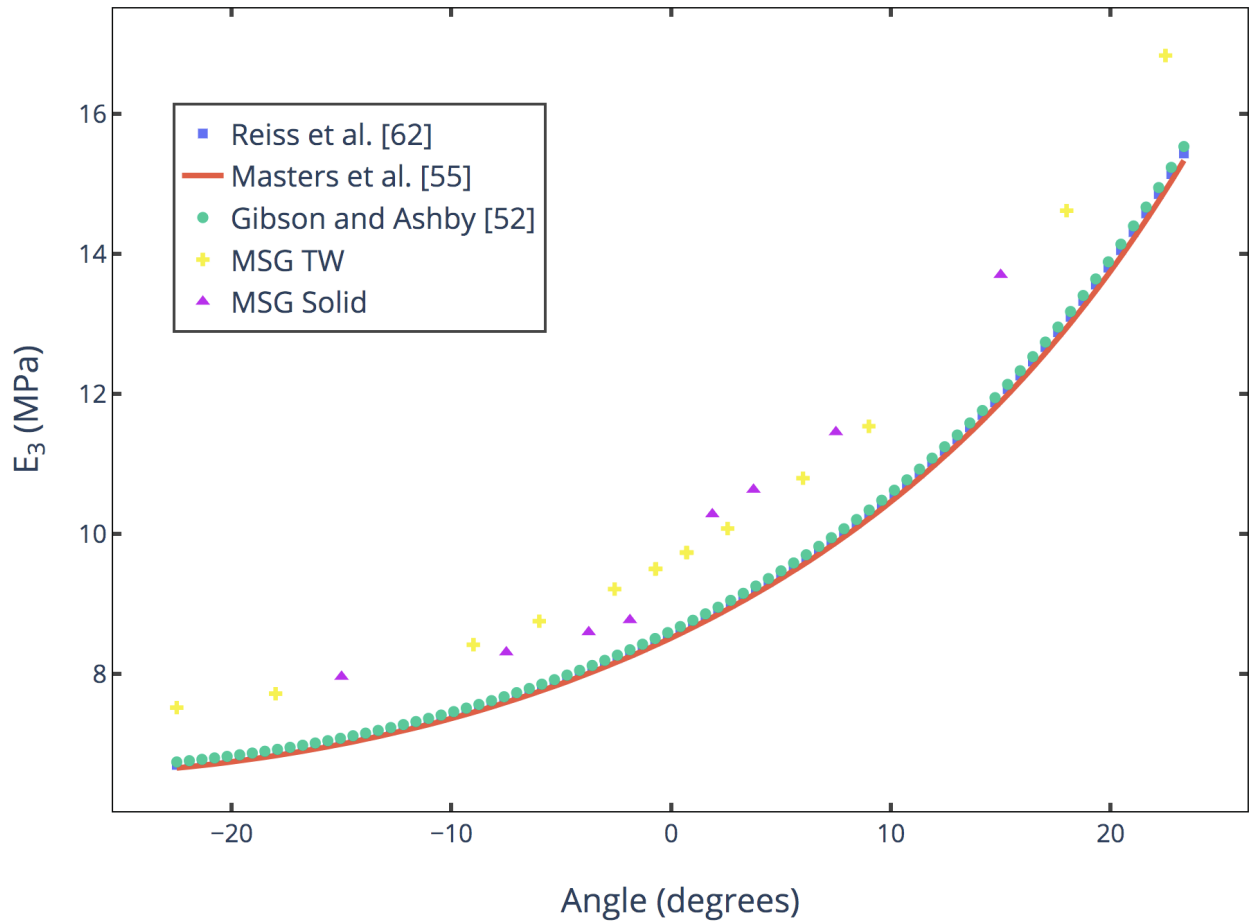


Figure 3.17. Equivalent Young's modulus of a cellular solid structure in x_3 direction.

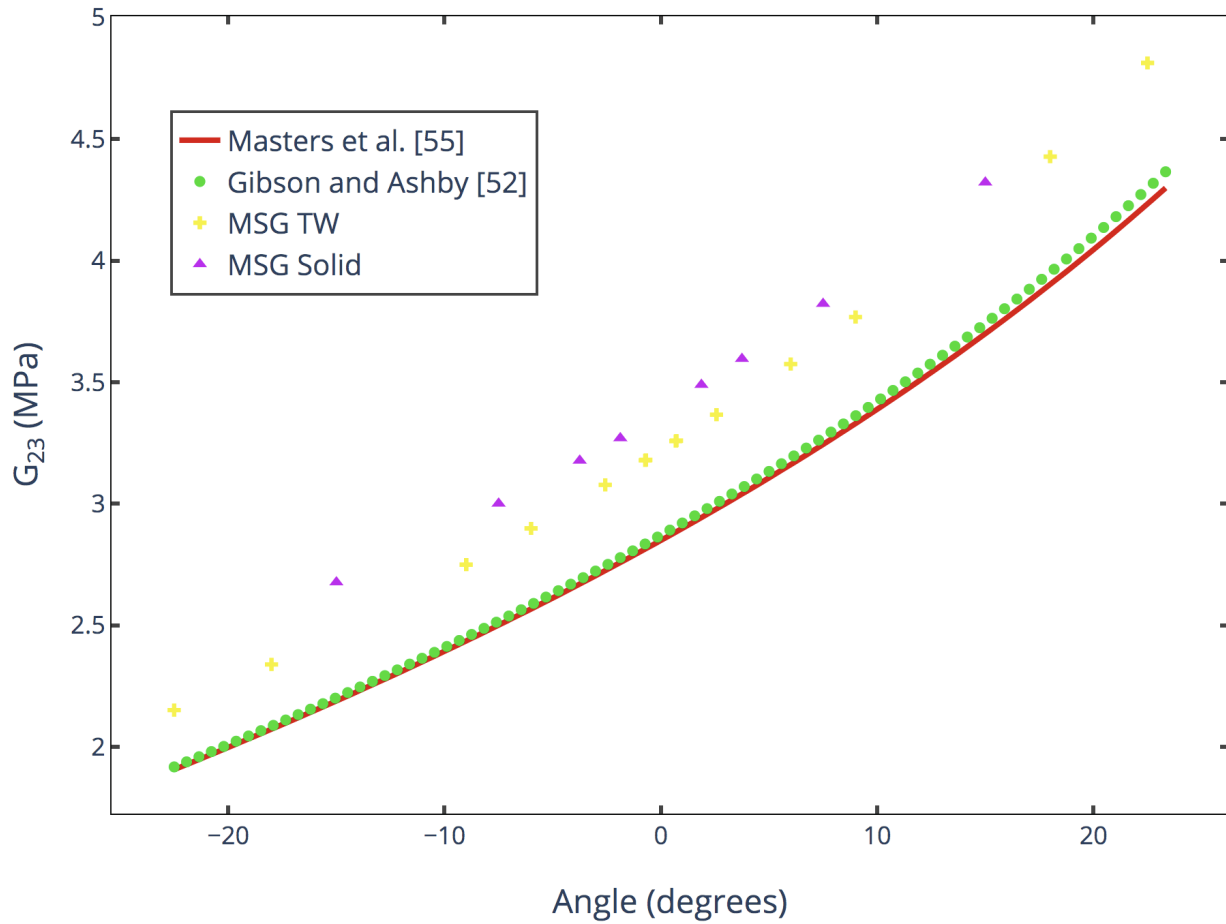


Figure 3.18. Equivalent shear modulus of a cellular solid structure in $x_2 - x_3$ direction.

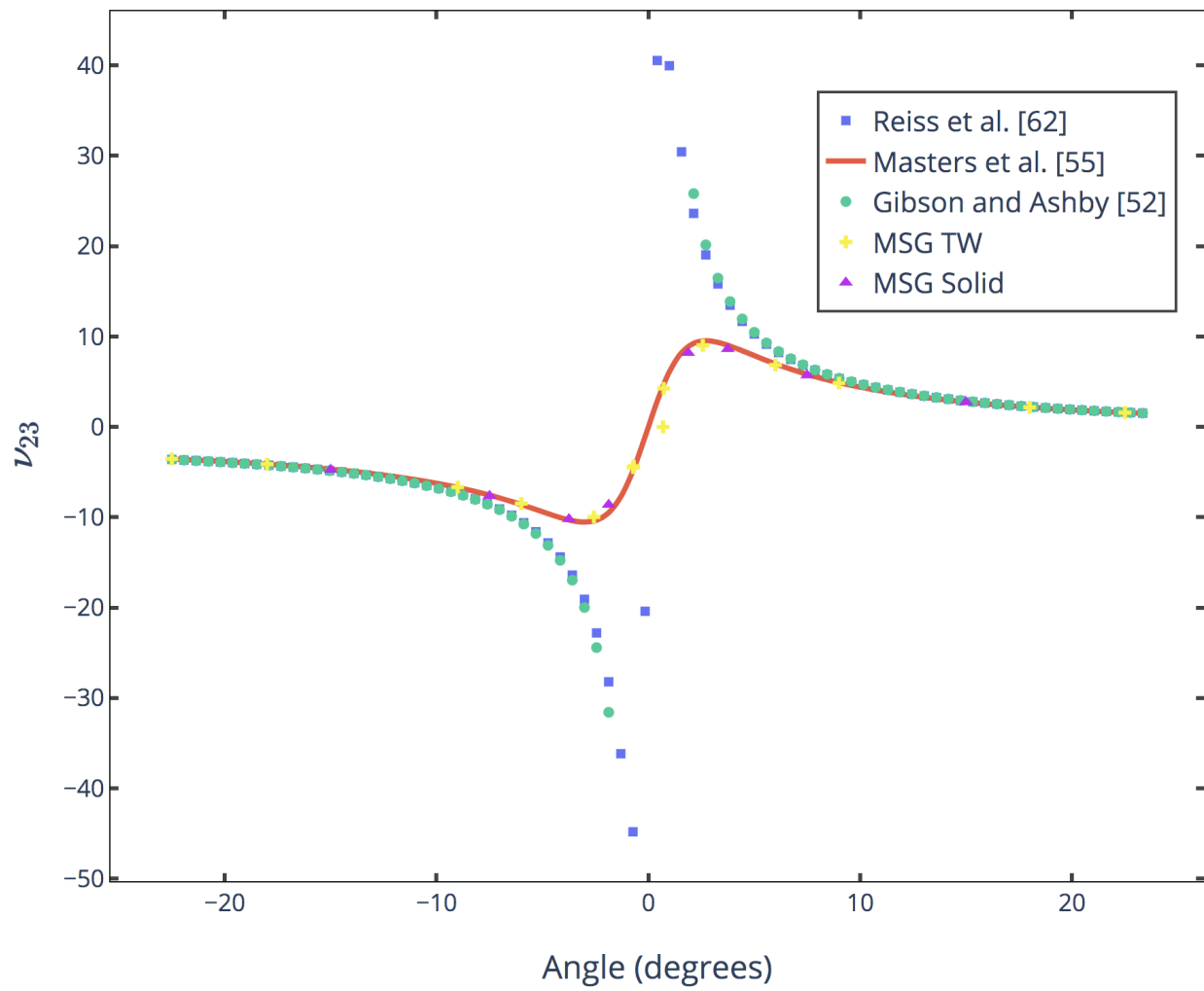


Figure 3.19. In-plane Poisson's ratio of a cellular solid structure.

Table 3.10. Equivalent 3D stiffness matrix of a cellular solid structure for $\theta = 15^\circ$ (a) MSG-TW, (b) MSG solid model, and (c) Error %.

Stiffness (MPa)	(a)	(b)	(c)
C_{11}	4736.9	4678.9	1.23
C_{12}	1089.4	1105.5	1.46
C_{13}	381.81	386.88	1.31
C_{22}	2446.39	2488.9	1.71
C_{23}	847.44	860.89	1.56
C_{33}	306.99	311.48	1.44
C_{44}	4.3215	4.1919	2.99
C_{55}	564.15	573.11	1.56
C_{66}	997.52	1000.1	0.26

modulus in x_3 direction (Figure 3.17) and equivalent shear modulus in $x_2 - x_3$ direction (Figure 3.17) are higher for the case of MSG-TW and MSG solid model in comparison to [52], [62], and [55]. This is due to considering the additional segments (highlighted with blue line in Figure 3.15) present in the SG of the MSG solid and MSG-TW models in comparison to [52], [62], and [55]. The non-zero components of the equivalent 3D stiffness matrix obtained using MSG-TW are compared with MSG solid model for $\theta = 15^\circ$ rad and $\theta = -15^\circ$ rad in Table 3.10 and Table 3.11. It can be seen that MSG-TW model provides stiffness values close to that obtained by the MSG solid model with the maximum error in the C_{44} values. This difference can be attributed to the shear modulus having contribution from the transverse shear deformation of each segment. Since these terms are neglected in classical laminated plate theory (CLPT), we see a discrepancy in the results. It is believed that if a higher-order plate theory like the RM theory is used to represent the strain energy associated with each segment in the SG, the results will be more accurate.

In order to perform the analysis using MSG-TW, 10 elements with 3 nodes each were used and each node having 4 dofs which is computationally much cheaper in comparison to MSG solid where 3,428 2D quadratic elements were used with a total of 11,587 nodes and each node having 3 dofs.

Table 3.11. Equivalent 3D stiffness matrix of a cellular solid structure for $\theta = -15^\circ$ (a) MSG-TW, (b) MSG solid model, and (c) Error %.

Stiffness (MPa)	(a)	(b)	(c)
C_{11}	7507.4	7352.9	2.10
C_{12}	1094.1	1075.2	1.75
C_{13}	-220.53	-213.94	3.08
C_{22}	4154.9	4080.0	1.83
C_{23}	-847.45	-821.77	3.12
C_{33}	180.75	173.48	4.19
C_{44}	2.6775	2.4705	7.73
C_{55}	332.17	346.01	4.00
C_{66}	1694.2	1706.4	0.71

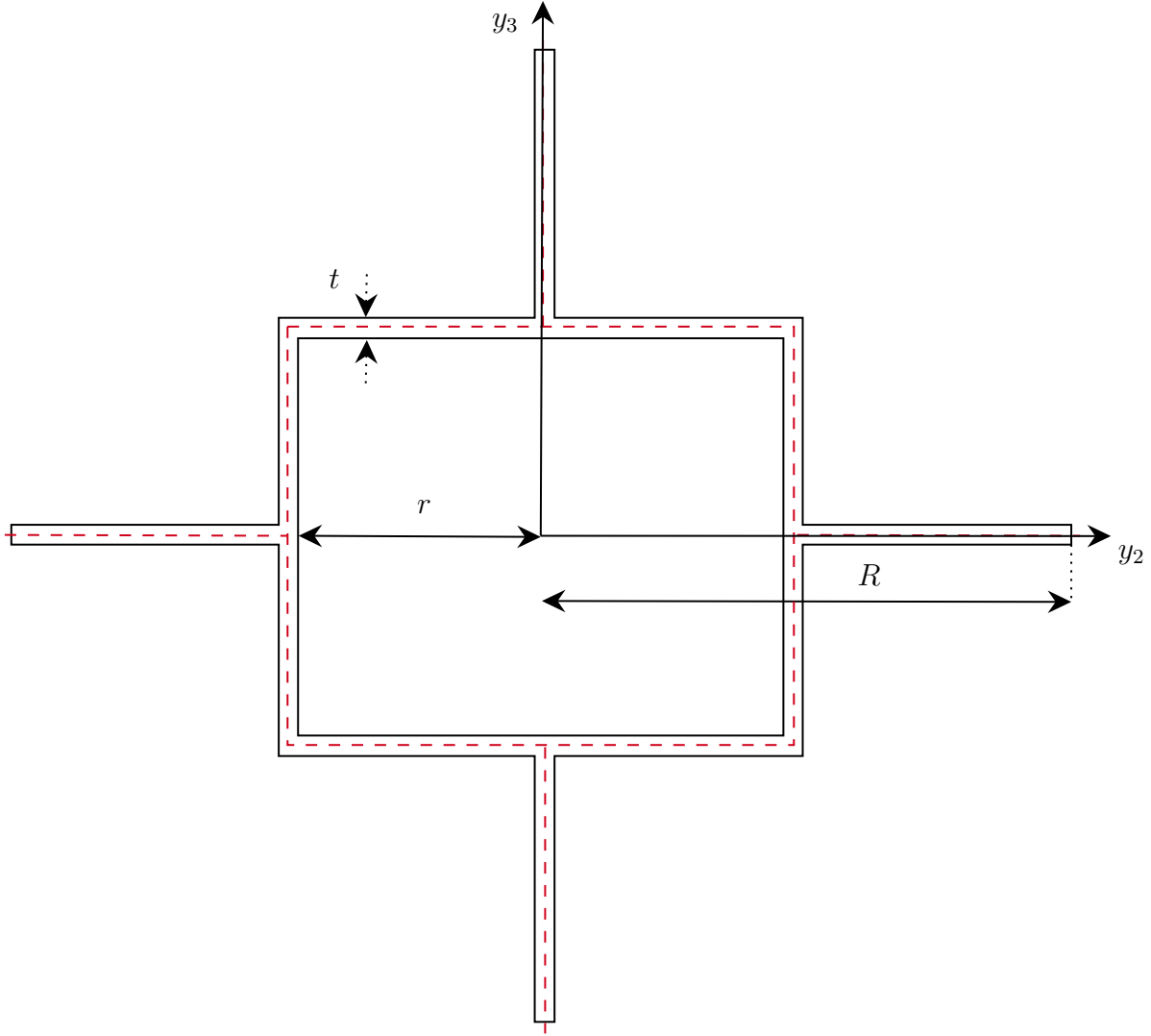


Figure 3.20. Schematic of a hierarchical square SG.

3.3.2 Hierarchical square

The next example is a hierarchical square which has been presented in [67]. Mousanezhad et al. [67] uses the Castigliano's second theorem to obtain the equivalent 2D equivalent properties. This method is a simplified use of the energy approach and provides good results for SG with complex geometries but is only limited to isotropic materials. The SG and the associated geometric parameters have been shown in Figure 3.20.

As elaborated in [67], the ratio r/R is the de-facto measure of the magnitude of alteration, the variations of the effective properties verses the ratio r/R have been presented

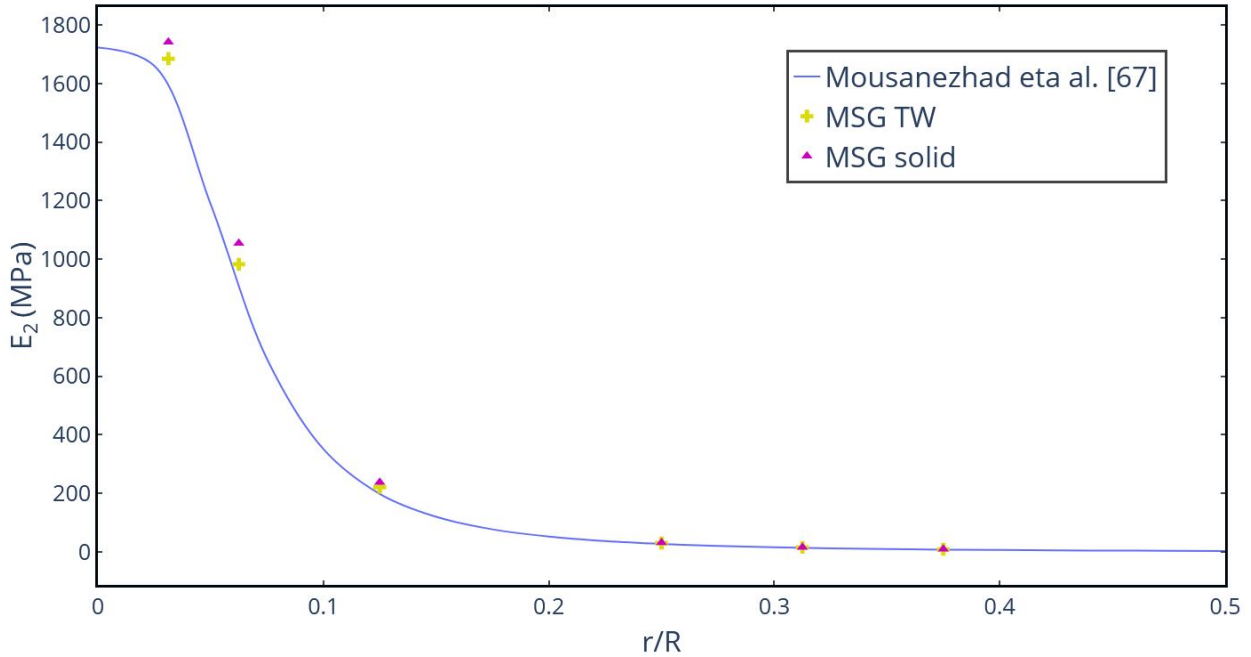


Figure 3.21. Equivalent Young's modulus of a hierarchical square.

in Figures 3.21 - 3.23. The material used in this example is aluminium which has Young's modulus $E = 68.9$ GPa, and Poisson's ratio $\nu = 0.33$. The geometric parameters of t and R have been kept fixed, having values of 5 mm and 10 cm respectively. These results have been compared with the results obtained from [67]. The results obtained are close to the ones obtained by the MSG solid model and also show the same behaviour which was provided by the analytical solutions presented in [67]. Mousanezhad et al. [67] considers the beam energy of each segment of the SG which assumes the local in-plane shear components of the energy as zero but as MSG-TW takes these terms into consideration we see a small difference in the elastic modulus obtained. It should be noted that since the SG shows symmetry in the $x_2 - x_3$ plane the effective Young's modulus in both the directions are the same and hence only one of the components has been presented.

The individual components of the equivalent 3D stiffness matrix obtained for the case of $r = 5$ cm, keeping the other values fixed, have been presented in Table 3.12. The results obtained are close to the ones obtained using the MSG solid model with the maximum error being in C_{23} . This difference can be attributed to the usage of the CLPT at the local level.

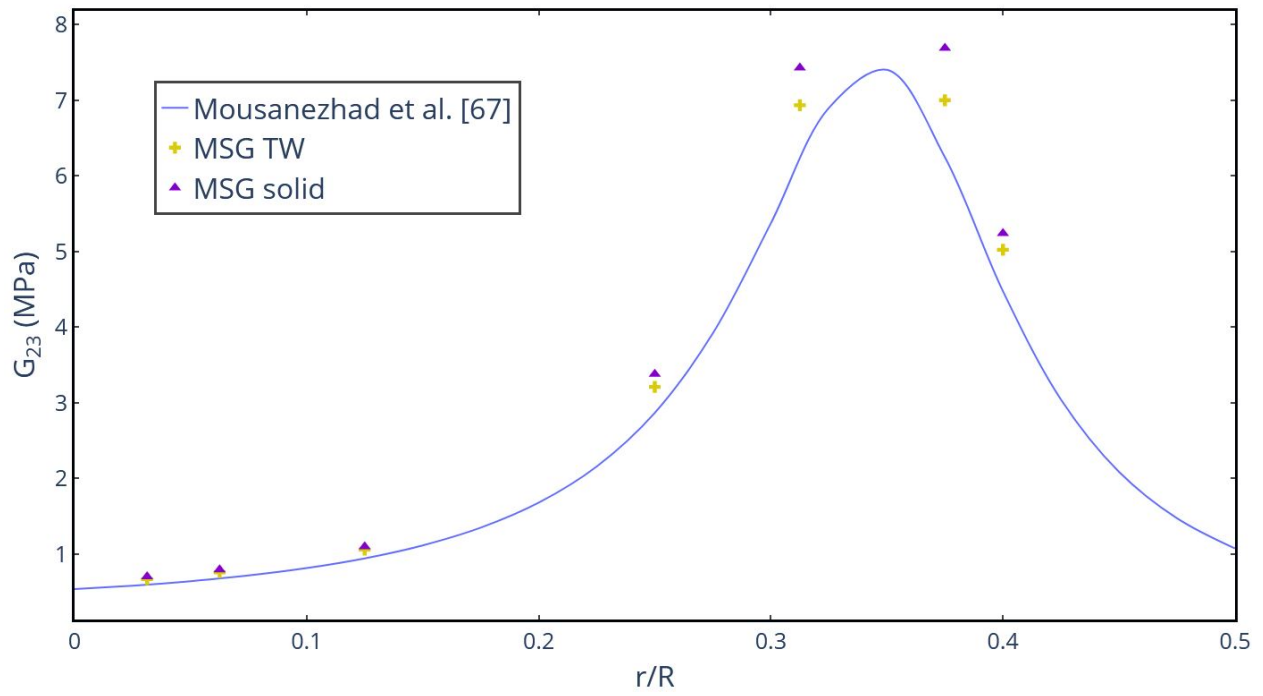


Figure 3.22. Equivalent shear's modulus of a hierarchical square in $x_2 - x_3$ direction.

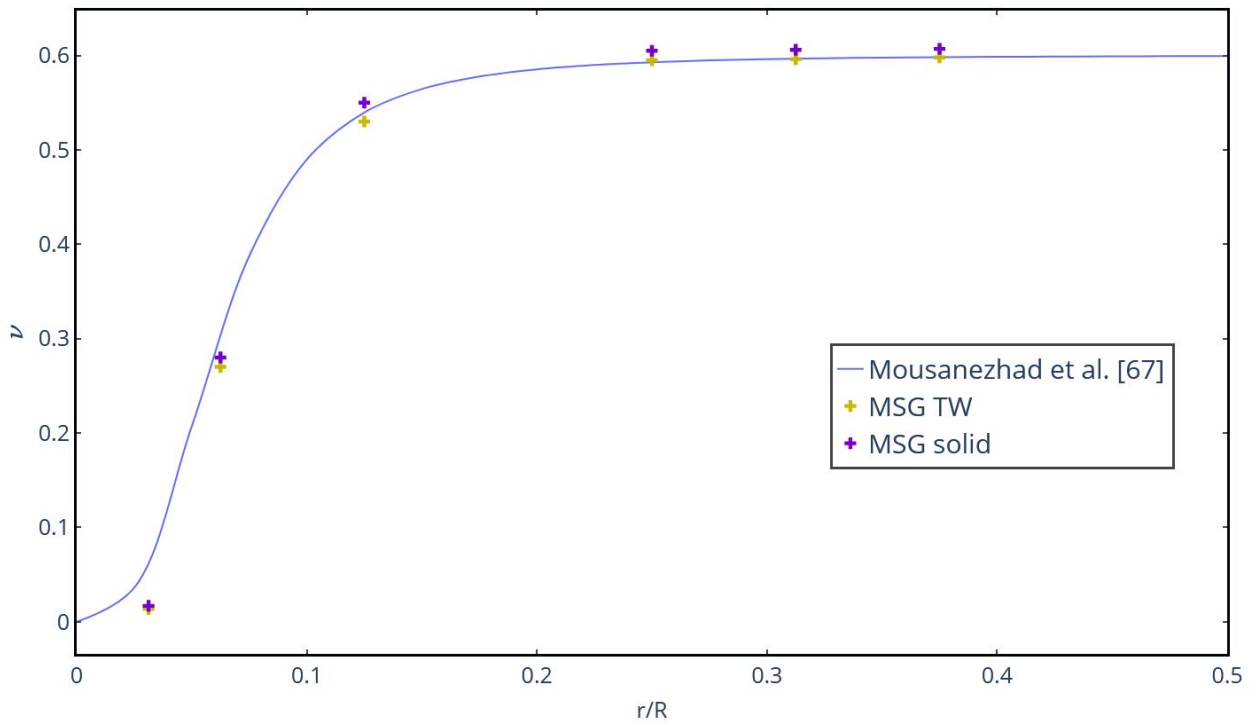


Figure 3.23. In-plane Poisson's ratio of a hierarchical square.

Table 3.12. Equivalent 3D stiffness matrix of a hierarchical square for $r = 5$ cm (a) MSG-TW, (b) MSG solid model, and (c) Error %.

Stiffness (MPa)	(a)	(b)	(c)
C_{11}	5186.39	5099.03	1.71
C_{12}	24.83	26.75	7.16
C_{13}	24.83	26.75	7.16
C_{22}	47.13	50.46	6.60
C_{23}	27.94	30.59	8.65
C_{33}	47.13	50.45	6.60
C_{44}	3.22	3.39	5.00
C_{55}	650.00	670.92	3.12
C_{66}	650.00	670.93	3.12

CLPT does not capture the local out-of-plane shear components of the energy and due to the inherent plate thickness associated with the segments we see the difference in C_{23} .

In order to perform the analysis using MSG-TW, 12 elements with 3 nodes each were used and each node having 4 dofs which is computationally much cheaper in comparison to MSG solid model where 3,362 2D quadratic elements were used with a total of 11,176 nodes and each node having 3 dofs.

3.3.3 Composite square

The final 3D example is a composite square, the geometry and dimensions of which has been shown in Figure 3.24. Every segment in this SG is made up of 8 layers of composite laminate with thickness of 0.127 mm and each laminate has a fiber orientation of 15° . The material used in the laminates has the following properties:

$$E_1 = 141.96 \text{ GPa}, \quad E_2 = E_3 = 9.79 \text{ GPa},$$

$$G_{12} = G_{23} = G_{13} = 6.136 \text{ GPa} \quad \nu_{12} = \nu_{13} = \nu_{23} = 0.42$$

This particular example has been chosen to showcase the full potential of MSG-TW to obtain equivalent 3D stiffness matrices for a SG having anisotropic material properties.

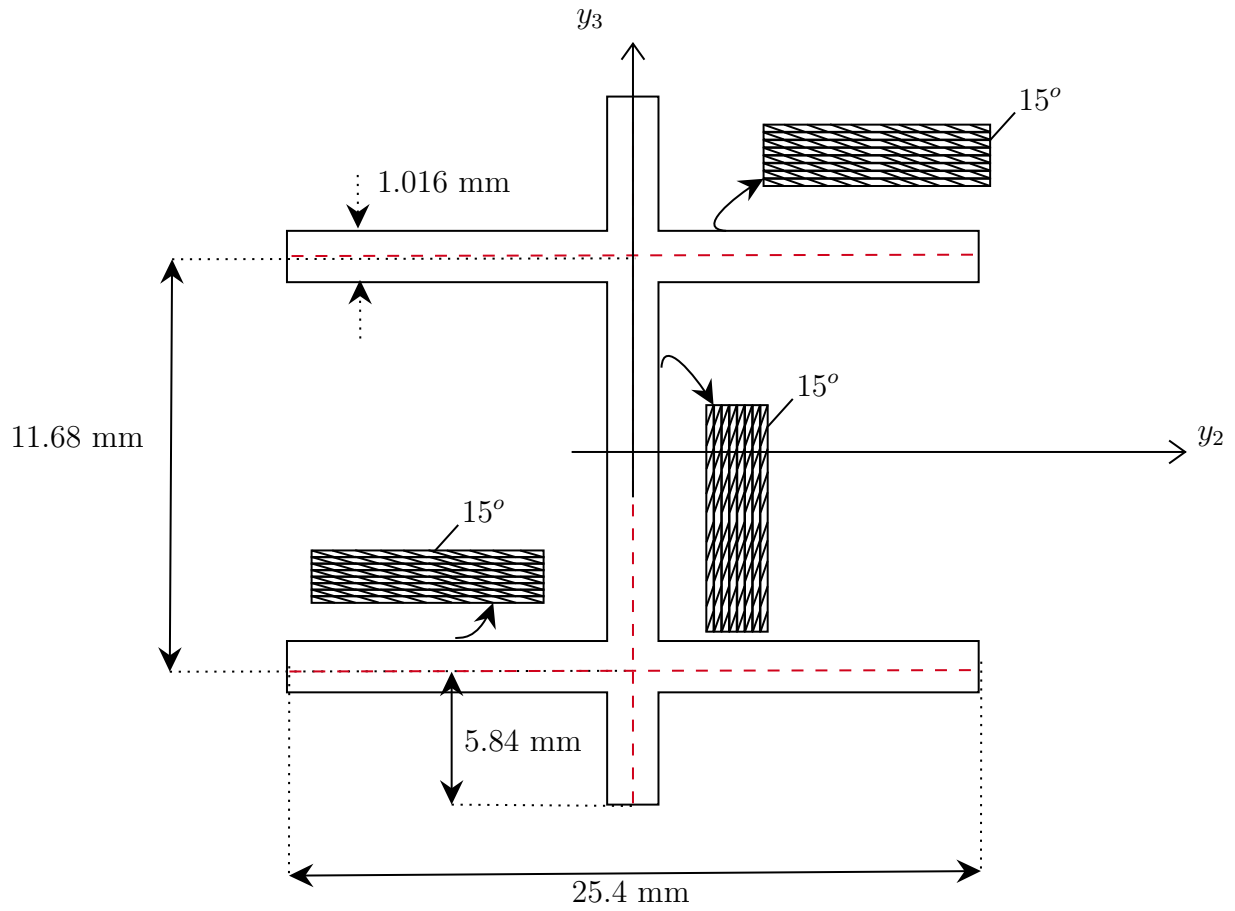


Figure 3.24. Schematic of a composite square SG.

Table 3.13. Equivalent 3D stiffness matrix of a composite square (a) MSG-TW, (b) MSG solid model, and (c) Error %.

Stiffness (MPa)	(a)	(b)	(c)
C_{11}	16133.90	15518.11	3.97
C_{12}	1016.82	1008.76	0.80
C_{13}	468.38	459.01	2.04
C_{15}	-1192.81	-1135.27	5.07
C_{16}	2589.74	2535.23	2.15
C_{22}	983.56	988.88	0.54
C_{23}	3.04E-06	20.44	100
C_{26}	317.09	311.80	1.7
C_{33}	453.06	456.25	0.70
C_{35}	-146.06	-140.04	4.3
C_{44}	1.08	1.16	7.48
C_{55}	547.32	545.43	0.35
C_{66}	1188.20	1188.30	0.01

The non-zero components of the equivalent 3D stiffness matrix obtained for this case are presented in Table 3.13.

The values for the stiffness components obtained by using MSG-TW are close to the values obtained via the MSG solid model except for C_{23} . This difference can be attributed to the in-plane components having contribution from transverse shear deformation of each segment. Since these terms are neglected in CLPT, we see a discrepancy in the results. To validate this claim, the variation of the 3D strain components of E_{22} and $2E_{13}$ (following Abaqus conventions) for an applied global strain of $\Gamma_{33} = 0.01$ were obtained using the MSG solid model, as seen in Figure 3.25 and Figure 3.26. The plots of both the strain components along the reference line of the top flange can be seen in Figure 3.27. As seen in Figures 3.25 - 3.27, the out-of-plane shear strain component ($2E_{13}$) is comparable in magnitude to the in-plane axial strain component (E_{22}) but in the proposed model the out-of-plane shear strain component is neglected by CLPT which leads to an error in C_{23} . It is believed that if a higher-order plate theory like the first-order shear deformation theory is used to describe the strain energy associated with each segment within the SG, the results will be more accurate, which will be studied in future works.

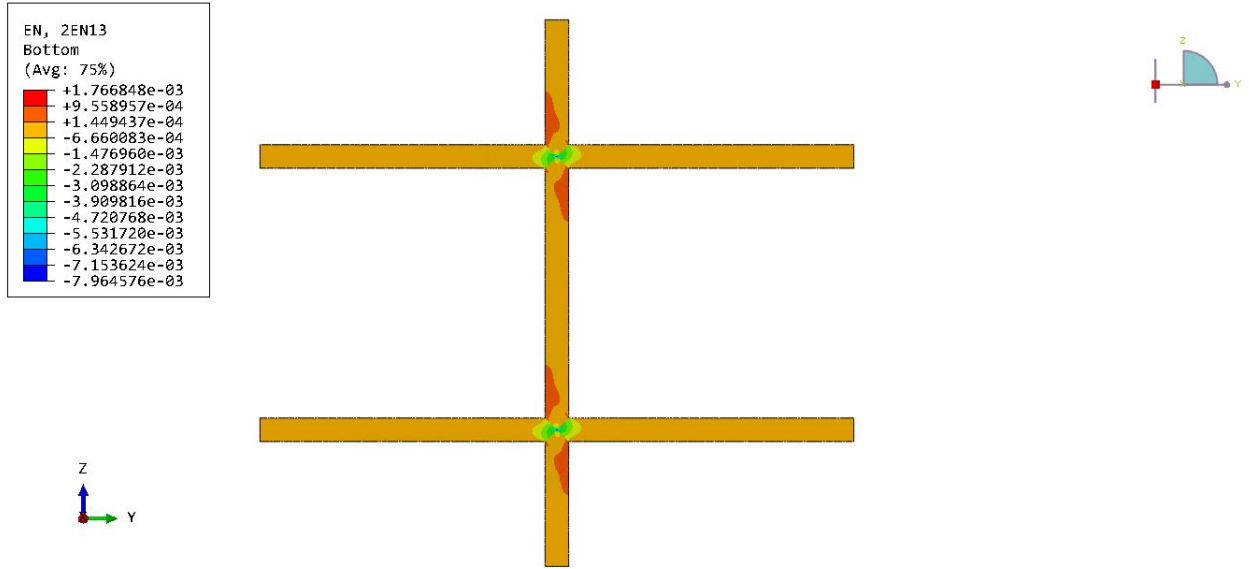


Figure 3.25. Variation of $2E_{13}$ to a global strain of $\Gamma_{33} = 0.01$.

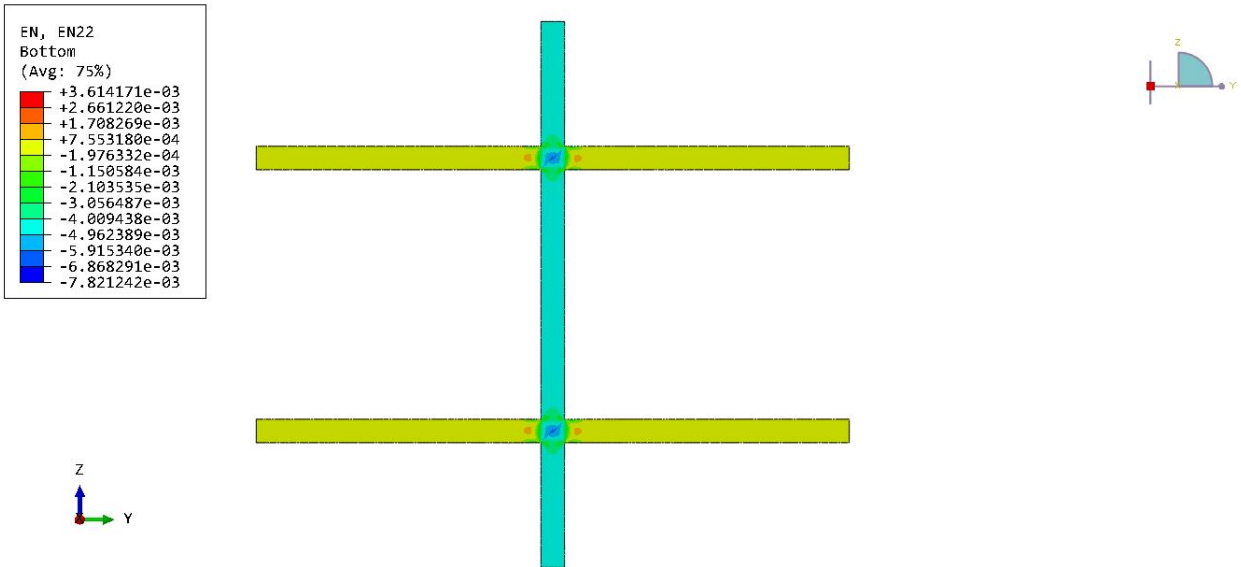


Figure 3.26. Variation of E_{22} to a global strain of $\Gamma_{33} = 0.01$.

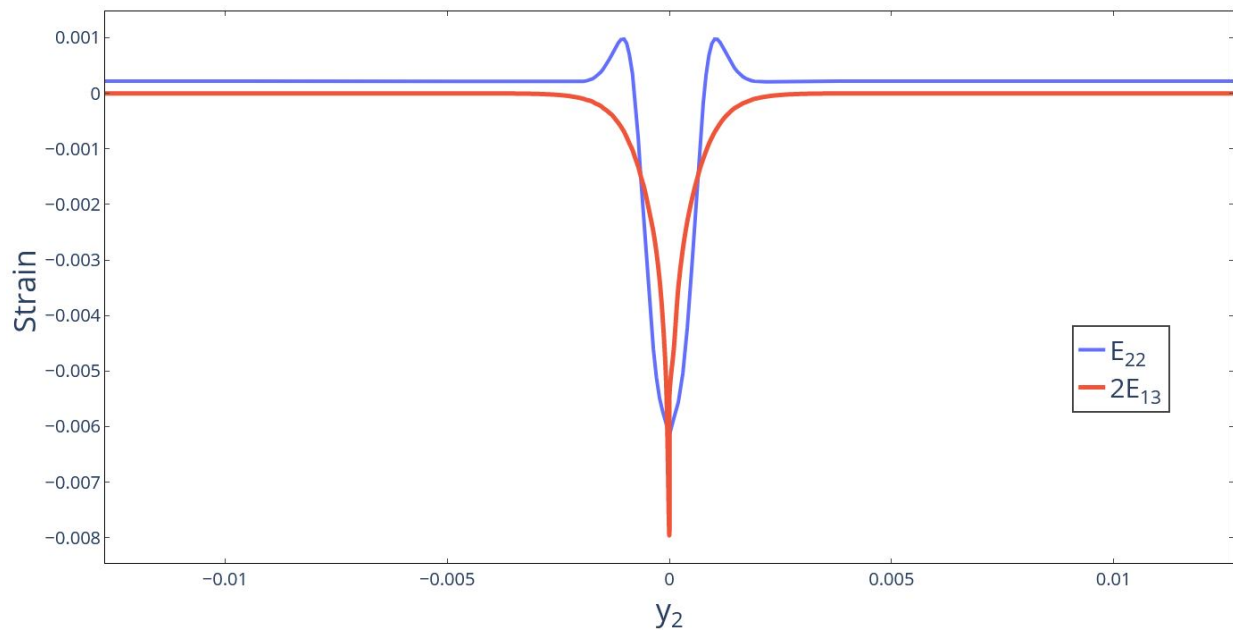


Figure 3.27. Variation of E_{22} and $2E_{13}$ along the reference line of the top flange.

In order to perform the analysis using MSG-TW, 8 elements with 3 nodes each were used and each node having 4 dofs which is computationally much cheaper in comparison to the MSG solid model where 54,159 2D quadratic elements were used with a total of 164,612 nodes and each node having 3 dofs.

4. CONCLUSION AND FUTURE PROSPECTS

4.1 Conclusion

In this dissertation, a general framework for obtaining equivalent properties of thin-walled beams, plates and 3D structures has been presented. This has been achieved by representing the structure gene (SG) as an assembly of straight members whose energy can be adequately represented using the classical lamination plate theory (CLPT). The plate stiffness matrix used to represent the strain energy of each segment of the SG is considered to be fully populated, which makes the proposed model a general purpose theory which can tackle geometrically complex SGs such as multi-cell beam sections and corrugated plates with face sheets. The proposed theory can deal with anisotropic material properties present in the SG and can be used as an alternative to the MSG solid model, where quick results are required without expensive modeling and computational efforts.

Several examples have been studied to demonstrate the versatility of the proposed theory and the results are in good agreement with those available in the literature and the MSG solid model. For the case of thin-walled beams, the results are in good agreement with the cross-sectional properties obtained from VABS with a prominent computational advantage. The present theory can be used as an alternative to VABS, where quick results are required. The current framework does not use additional constraints for closed sections in comparison to open sections hence it can be used for the design of arbitrary thin-walled sections.

For the case of thin-walled corrugated plates, the results are also in good agreement with the equivalent plate properties obtained from the MSG solid model with a prominent computational advantage by meshing the 2D SG using 1D line elements instead of 2D solid elements. The present theory is able to capture the coupled modes of deformation which may exist in corrugated plates made of composite materials.

For the case of thin-walled 3D structures, the results are also in good agreement with the equivalent 3D properties obtained from the MSG solid model with a prominent computational advantage. The theory presented is able to capture the coupled modes of deformation which are inherent to thin-walled SGs which use composite materials. The equivalent 3D properties obtained using the proposed theory provides the out-of-plane properties using

only a 2D SG which makes it more computationally efficient than using a 3D RVE and more general purpose than theories which assume material orthotropy in a 2D RVE.

4.2 Future prospect: MSG-TW using RM plate model

The effective properties which are obtained using MSG-TW only provide accurate results when the height of the plates are small in comparison to the length of the segments since only CLPT is considered at the local segment level. As seen in Figure 3.2 on increasing the thickness of the segments the accuracy decreases. To account for thick segments higher-order theory plate theory such as the Reissner-Mindlin (RM) plate model need to be used at the local segment level.

In order to use the RM plate model, additional dofs are need to describe the energy of each segment. These dofs account for the rotations associated with each material point on the reference surface. The dependence of these additional dofs on the global variables can be obtained by assuming that CLPT as a special case of the RM plate model where the transverse strain are zero ($2\gamma_{13} = 0$, $2\gamma_{23} = 0$). These out-of-plane strain terms can be represented as:

$$\begin{aligned} 2\epsilon_{13}^p &= \phi_2^p + \frac{\partial u_3^p}{\partial x_1^p} \\ 2\epsilon_{23}^p &= -\phi_1^p + \frac{\partial u_3^p}{\partial x_2^p} \end{aligned} \quad (4.1)$$

where, ϕ_2^p represents the rotational dof along x_2^p and ϕ_1^p represents the rotational dof along x_1^p .

These have been illustrated in Figure 4.1. Additionally the bending curvatures (κ_{11}^p , κ_{22}^p , $2\kappa_{12}^p$) can be described in terms of ϕ_1^p and ϕ_2^p as:

$$\begin{aligned} \kappa_{11}^p &= \frac{\partial \phi_2^p}{\partial x_1^p} \\ \kappa_{22}^p &= -\frac{\partial \phi_1^p}{\partial x_2^p} \\ 2\kappa_{12}^p &= \frac{\partial \phi_2^p}{\partial x_2^p} - \frac{\partial \phi_1^p}{\partial x_1^p} \end{aligned} \quad (4.2)$$

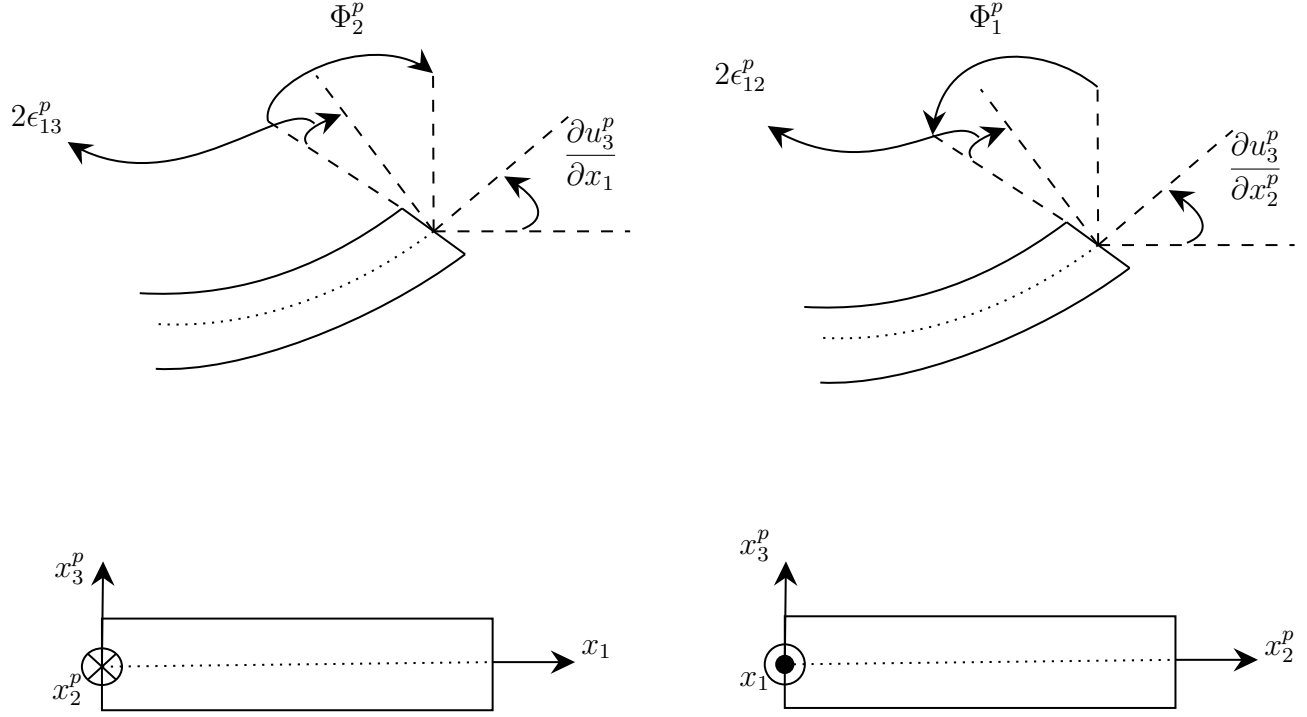


Figure 4.1. Rotational kinematics variables.

For the case of beams, on setting these strain terms to zero we obtain the zeroth order approximation for the displacement fields, $u_i^p \equiv u_i^p(x_1, y_2(y_2^p), y_3(y_2^p))$ and the rotations as:

$$\begin{aligned}
 u_1^p &= \bar{u}_1(x_1) - \varepsilon y_2 \bar{u}'_2(x_1) - \varepsilon y_3 \bar{u}'_3(x_1) \\
 u_2^p &= \dot{y}_2 \bar{u}_2(x_1) + \dot{y}_3 \bar{u}_3(x_1) + \varepsilon (y_2 \dot{y}_3 - y_3 \dot{y}_2) \Phi(x_1) \\
 u_3^p &= -\dot{y}_3 \bar{u}_2(x_1) + \dot{y}_2 \bar{u}_3(x_1) + \varepsilon (y_3 \dot{y}_3 + y_2 \dot{y}_2) \Phi(x_1) \\
 \phi_2^p &= -\dot{y}_2 \bar{u}'_3(x_1) + \dot{y}_3 \bar{u}'_2(x_1) - \varepsilon (y_3 \dot{y}_3 + y_2 \dot{y}_2) \kappa_1(x_1) \\
 \phi_1^p &= \Phi(x_1)
 \end{aligned} \tag{4.3}$$

These kinematic variables can be perturbed using the fluctuating functions, $w_i^p \equiv w_i^p(x_1, y_2, y_3)$ and $\psi_\alpha^p \equiv \psi_\alpha^p(x_1, y_2, y_3)$, as:

$$\begin{aligned}
u_1^p &= \bar{u}_1 - \varepsilon y_2 \bar{u}'_2 - \varepsilon y_3 \bar{u}'_3 + \varepsilon w_1^p \\
u_2^p &= \dot{y}_2 \bar{u}_2 + \dot{y}_3 \bar{u}_3 + \varepsilon (y_2 \dot{y}_3 - y_3 \dot{y}_2) \Phi + \varepsilon w_2^p \\
u_3^p &= -\dot{y}_3 \bar{u}_2 + \dot{y}_2 \bar{u}_3 + \varepsilon (y_3 \dot{y}_3 + y_2 \dot{y}_2) \Phi + \varepsilon w_3^p \\
\phi_2^p &= -\dot{y}_2 \bar{u}'_3 + \dot{y}_3 \bar{u}'_2 - \varepsilon (y_3 \dot{y}_3 + y_2 \dot{y}_2) \kappa_1 + \varepsilon \psi_2^p \\
\phi_1^p &= \Phi + \varepsilon \psi_1^p
\end{aligned} \tag{4.4}$$

Substituting Eq. (4.4) into Eq. (2.10), Eq. (4.1), and Eq. (4.2), using the partial derivative expression in Eq. (2.2), the RM plate strains can be written as:

$$\begin{aligned}
\epsilon_{11}^p &= \gamma_{11} + \varepsilon y_3 \kappa_2 - \varepsilon y_2 \kappa_3 \\
\epsilon_{22}^p &= \dot{w}_2^p \\
2\epsilon_{12}^p &= \dot{w}_1^p + (\varepsilon y_2 \dot{y}_3 - \varepsilon y_3 \dot{y}_2) \kappa_1 \\
\kappa_{11}^p &= \dot{y}_2 \kappa_2 + \dot{y}_3 \kappa_3 \\
\kappa_{22}^p &= \dot{\psi}_1^p \\
2\kappa_{12}^p &= -2\kappa_1 + \dot{\psi}_2^p \\
2\epsilon_{13}^p &= \varepsilon \psi_2^p \\
2\epsilon_{23}^p &= \varepsilon \psi_1^p + \dot{w}_3^p
\end{aligned} \tag{4.5}$$

Here we have discarded the asymptotically smaller terms. It should be noted in the above equation ψ_1^p and ψ_2^p are treated as one order higher than w_1^p , w_2^p , and w_3^p as they correspond to the perturbation of the slope degrees of freedom. The overall strain energy density associated with an isotropic segment can be written as:

$$\Pi = \frac{1}{2} \langle (\epsilon^p)^T K \epsilon^p \rangle \tag{4.6}$$

here $\epsilon^p = [\epsilon_{11}^p \quad \epsilon_{22}^p \quad 2\epsilon_{12}^p \quad \kappa_{11}^p \quad \kappa_{22}^p \quad 2\kappa_{12}^p \quad 2\epsilon_{13}^p \quad 2\epsilon_{23}^p]^T$ and

$$K = \begin{bmatrix} A_{11} & A_{12} & 0 & 0 & 0 & 0 & 0 & 0 \\ A_{12} & A_{22} & 0 & 0 & 0 & 0 & 0 & 0 \\ 0 & 0 & A_{66} & 0 & 0 & 0 & 0 & 0 \\ 0 & 0 & 0 & D_{11} & D_{12} & 0 & 0 & 0 \\ 0 & 0 & 0 & D_{12} & D_{22} & 0 & 0 & 0 \\ 0 & 0 & 0 & 0 & 0 & D_{66} & 0 & 0 \\ 0 & 0 & 0 & 0 & 0 & 0 & \bar{G}_{13} & 0 \\ 0 & 0 & 0 & 0 & 0 & 0 & 0 & \bar{G}_{23} \end{bmatrix} \quad (4.7)$$

where the additional terms, \bar{G}_{13} and \bar{G}_{23} , are the shear modulus of the material multiplied by the thickness and the shear correction factor. It should be noted K assumes this specific form in Eq. (4.7) for an isotropic plate segment. For a general composite segment we could have a completely populated 8×8 stiffness matrix. On inputting Eq. (4.5) into Eq. (4.6), we get the following strain energy density of the isotropic strip:

$$\begin{aligned} \Pi = & \langle (\gamma_{11} - \epsilon y_2 \kappa_3)^2 A_{11} + 2\dot{w}_2^p (\gamma_{11} - \epsilon y_2 \kappa_3) A_{12} + (\dot{w}_2^p)^2 A_{22} + (\dot{w}_1^p)^2 A_{66} \rangle \\ & + \langle (\kappa_2)^2 D_{11} + 2\dot{\psi}_1^p \kappa_2 D_{12} + (\dot{\psi}_1^p)^2 D_{22} + (-2\kappa_1 + \dot{\psi}_2^p)^2 D_{66} \rangle \\ & + \langle (\epsilon \dot{\psi}_2^p)^2 \bar{G}_{13} + (\epsilon \dot{\psi}_1^p + \dot{w}_3^p)^2 \bar{G}_{23} \rangle \end{aligned} \quad (4.8)$$

The case of an isotropic strip has been solved analytically by minimizing Eq. (4.8) with respect to the fluctuating functions to obtain the following fluctuating terms:

$$\begin{aligned} \dot{w}_1^p &= 0 \\ \dot{w}_2^p &= -\nu(\gamma_{11} - \epsilon y_2 \kappa_3) \\ \dot{w}_3^p &= \kappa_2 \nu y_2 \\ \dot{\psi}_1^p &= -\frac{1}{\epsilon} \kappa_2 \nu y_2 \\ \dot{\psi}_2^p &= \frac{1}{\epsilon} \frac{4\kappa_1 \sinh(Zc/2)}{Z \sinh(Zc)} \sinh(Zs) \end{aligned} \quad (4.9)$$

where $Z = \sqrt{\bar{G}_{13}/D_{66}}$. Eq. (4.9) can be substituted into Eq. (2.10), Eq. (4.1), and Eq. (4.2) to obtain the plate strain terms:

$$\begin{aligned}
\epsilon_{11}^p &= \gamma_{11} - \varepsilon y_2 \kappa_3 \\
\epsilon_{22}^p &= -\nu(\gamma_{11} - \varepsilon y_2 \kappa_3) \\
2\epsilon_{12}^p &= 0 \\
\kappa_{11}^p &= \kappa_2 \\
\kappa_{22}^p &= -\kappa_2 \nu \\
2\kappa_{12}^p &= -2\kappa_1 + \frac{4\kappa_1 \sinh(Zc/2)}{\sinh(Zc)} \cosh(Zy_2) \\
2\epsilon_{13} &= \frac{4\kappa_1 \sinh(Zc/2)}{Z \sinh(Zc)} \sinh(Zy_2) \\
2\epsilon_{23} &= 0
\end{aligned} \tag{4.10}$$

It can be seen from Eq. (4.10), the terms associated with κ_1 are different from the CLPT approximation. To validate the solution, a specific case of aluminum strip is taken into consideration, with material properties as $E = 68.9$ GPa and $\nu = 0.33$. The height of the strip has been kept constant at 4 cm and the effective torsional stiffness has been calculated. Figure 4.2 shows the plot of the difference between torsional stiffness obtained from CLPT and the RM model with respect to MSG Solid. As expected, the RM model provides a much better value of torsional stiffness even at a aspect ratio of 1 : 5 in comparison to the CLPT model.

The recovered shear strain $2\epsilon_{13}$ for a beam torsional strain (κ_1) of 0.01 is presented in Figure 4.3. It shows the solution of $2\epsilon_{13}$ perfectly follows the hyperbolic strain curve obtained from the MSG Solid model.

The results shown in this section are very promising for an isotropic strip section. However it was beyond the scope of this dissertation to develop this theory further as it required additional continuity conditions to formulated for the new degrees of freedom (Ψ_1^p and Ψ_2^p). It is hoped that the model can be developed in the future by using the base idea presented here.

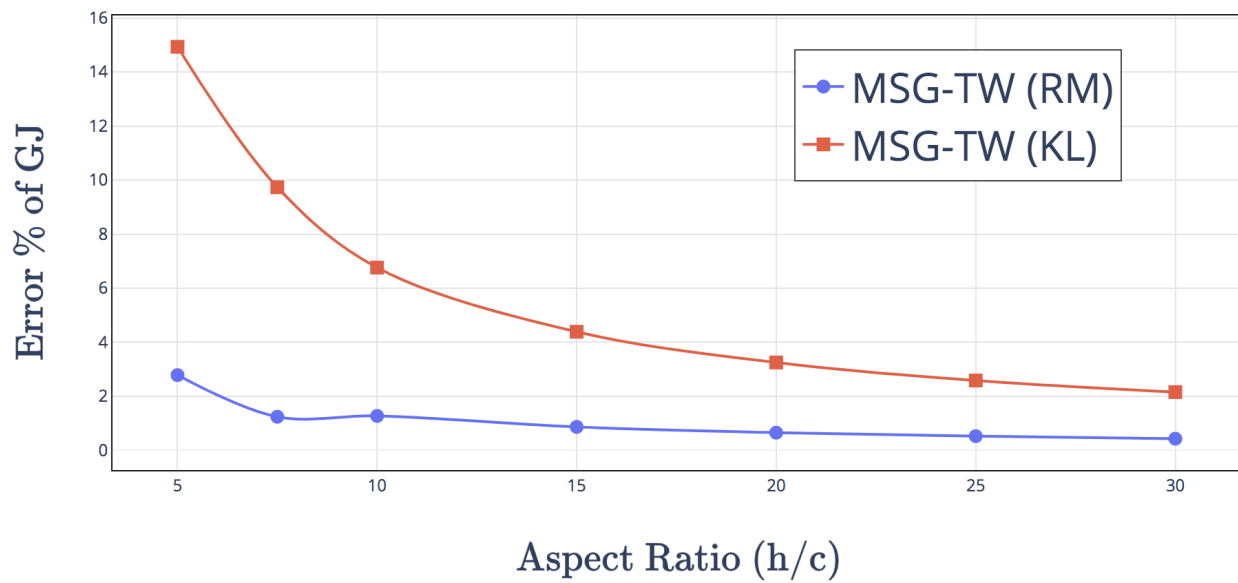


Figure 4.2. Convergence study of isotropic strip section.

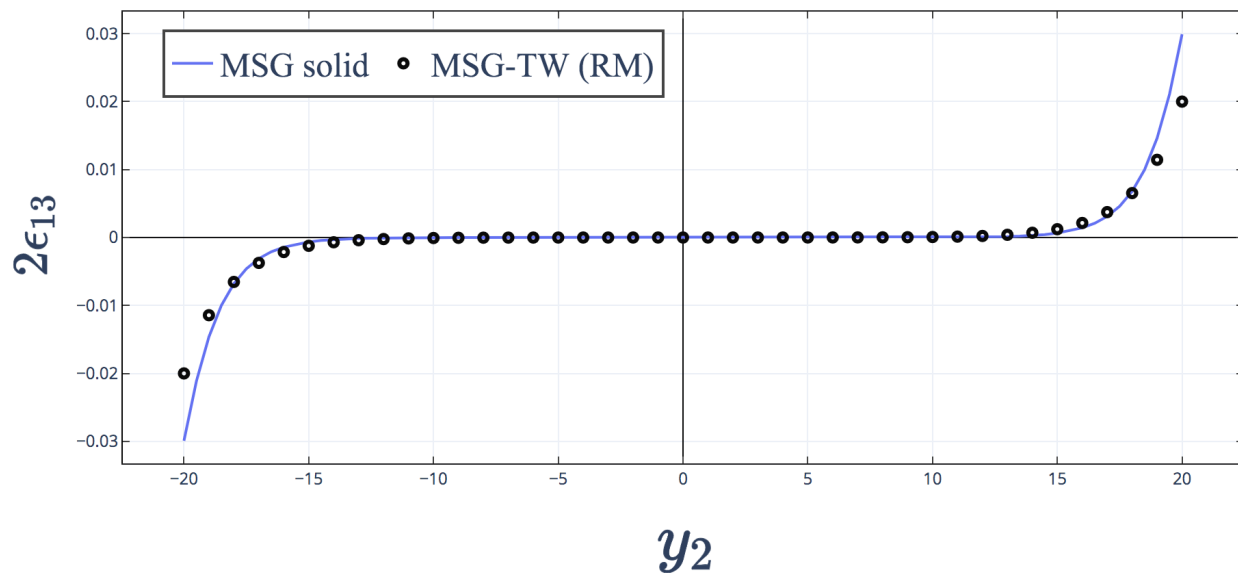


Figure 4.3. $2\epsilon_{13}$ distribution along the middle reference line.

A. SLOPE CONTINUITY CONDITION

In order to derive the slope continuity condition, we have considered the initial position vector of a point \vec{r}_0 before deformation, and the final position \vec{r} after deformation. \vec{r} can be written in terms of \vec{r}_0 and the displacement field \vec{u} as:

$$\vec{r} = \vec{r}_0 + \vec{u} \quad (\text{A.1})$$

As illustrated in Figure A.1, we have two segments numbered 1 and 2 and we have defined two coordinate systems, (x_1, x_2, x_3) being the global coordinate system and $(x_1, x_2^{p(i)}, x_3^{p(i)})$ being the global coordinate system for segment number i . In the undeformed configuration,

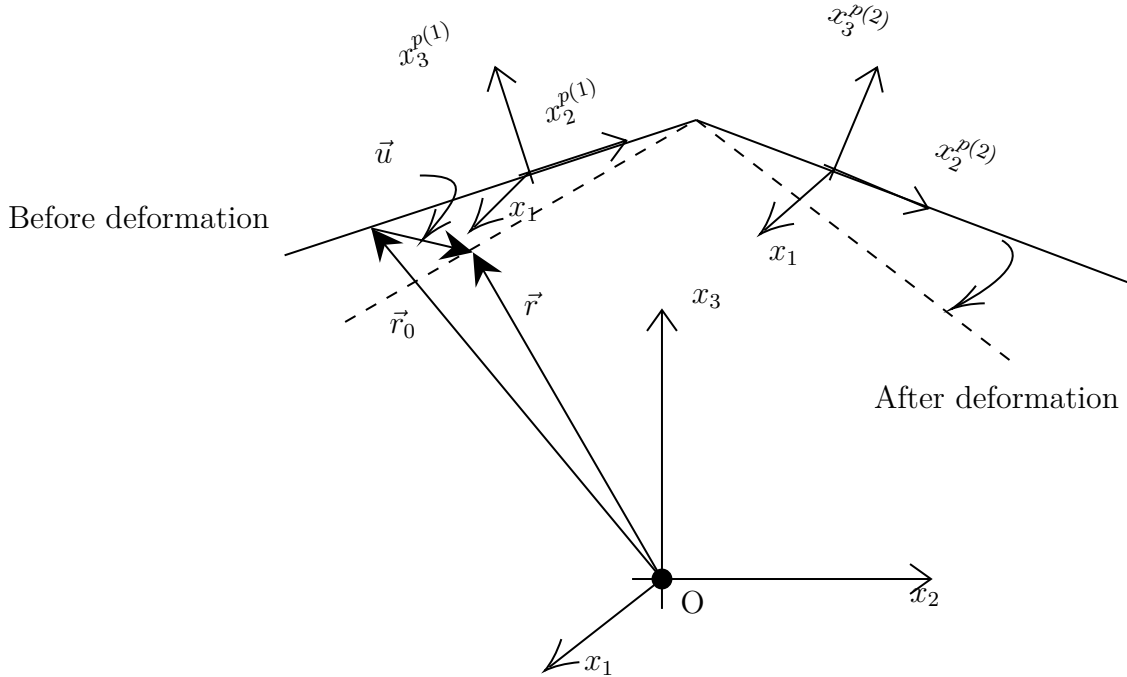


Figure A.1. Slope continuity

definitions of direction cosines \dot{y}_2 and \dot{y}_3 in Eq. (2.8) can be used to obtain the unit vectors along the plate reference line and perpendicular to it as:

$$\begin{aligned} \hat{e}_2^{p(i)} &= \dot{y}_2^{p(i)} \hat{e}_2 + \dot{y}_3^{p(i)} \hat{e}_3 \\ \hat{e}_3^{p(i)} &= -\dot{y}_3^{p(i)} \hat{e}_2 + \dot{y}_2^{p(i)} \hat{e}_3 \end{aligned} \quad (\text{A.2})$$

Here, $\hat{e}_2^{p(i)}$ is a unit vector along the each of the plate reference lines and $\hat{e}_3^{p(i)}$ is a unit vector perpendicular to the plate reference lines. Using Eq. A.2, we obtain the initial angle between the two plates before deformation as:

$$\cos \alpha_0 = \hat{e}_2^{p(1)} \cdot \hat{e}_2^{p(2)} \quad (\text{A.3})$$

Now using Eq. (A.1), a vector along the plate reference line in the deformed configuration can be written as:

$$\vec{S}^{p(i)} = \frac{\partial \vec{r}}{\partial x_2^{p(i)}} = \hat{e}_2^{p(i)} + \frac{\partial u_j^{p(i)}}{\partial x_2^{p(i)}} \hat{e}_j^{p(i)} \quad (\text{A.4})$$

where, $\hat{e}_j^{p(i)}$ refer to the unit vectors along $(x_1, x_2^{p(i)}, x_3^{p(i)})$ for $j = (1, 2, 3)$. Using this information we obtain the final angle between the two plates after deformation as:

$$\cos \alpha = \frac{\vec{S}^{p(1)} \cdot \vec{S}^{p(2)}}{|\vec{S}^{p(1)}| |\vec{S}^{p(2)}|} \quad (\text{A.5})$$

On expanding Eq. (A.5), and dropping the small nonlinear terms, we get:

$$\cos \alpha = \frac{\cos \alpha_0 \left(1 + \frac{\partial u_2^{p(2)}}{\partial x_2^{p(2)}} + \frac{\partial u_2^{p(1)}}{\partial x_2^{p(1)}} \right) + \left(-\dot{y}_2^{p(1)} \dot{y}_3^{p(2)} + \dot{y}_3^{p(1)} \dot{y}_2^{p(2)} \right) \left(\frac{\partial u_3^{p(2)}}{\partial x_2^{p(2)}} - \frac{\partial u_3^{p(1)}}{\partial x_2^{p(1)}} \right)}{|\vec{S}^{p(1)}| |\vec{S}^{p(2)}|} \quad (\text{A.6})$$

where (after dropping of small nonlinear terms):

$$|\vec{S}^{p(1)}| |\vec{S}^{p(2)}| = \left(1 + \frac{\partial u_2^{p(2)}}{\partial x_2^{p(2)}} + \frac{\partial u_2^{p(1)}}{\partial x_2^{p(1)}} \right) \quad (\text{A.7})$$

Eq. (A.6) can be simplified as:

$$(\cos \alpha - \cos \alpha_0) \left(1 + \frac{\partial u_2^{p(2)}}{\partial x_2^{p(2)}} + \frac{\partial u_2^{p(1)}}{\partial x_2^{p(1)}} \right) = \left(-\dot{y}_2^{p(1)} \dot{y}_3^{p(2)} + \dot{y}_3^{p(1)} \dot{y}_2^{p(2)} \right) \left(\frac{\partial u_3^{p(2)}}{\partial x_2^{p(2)}} - \frac{\partial u_3^{p(1)}}{\partial x_2^{p(1)}} \right) \quad (\text{A.8})$$

Based on the approximation that no shear strain exists in the plate, the initial angle, α_0 and the final angle, α are the same which leads to the right hand side of the above expression being zero. For the above equation to be valid, then, the partial derivative terms need to be zero which give us the slope continuity condition presented in Eq. (2.47).

For small angle changes, $\Delta\alpha$, where, $\alpha = \alpha_0 + \Delta\alpha$, we can further write Eq. (A.8) as:

$$\Delta\alpha \sin \alpha_0 \left(1 + \frac{\partial u_2^{p(2)}}{\partial x_2^{p(2)}} + \frac{\partial u_2^{p(1)}}{\partial x_2^{p(1)}} \right) = \left(-\dot{y}_2^{p(1)} \dot{y}_3^{p(2)} + \dot{y}_3^{p(1)} \dot{y}_2^{p(2)} \right) \left(\frac{\partial u_3^{p(2)}}{\partial x_2^{p(2)}} - \frac{\partial u_3^{p(1)}}{\partial x_2^{p(1)}} \right) \quad (\text{A.9})$$

the above equation can be used to additionally obtain boundary conditions if we have small changes in angles between the two plates.

B. ANALYTICAL SOLUTION FOR A CIRCULAR TUBE

The analytical expression for the cross-sectional properties of a circular tube was derived using the formulation in [18]. The methodology adopted in this work is similar to the MSG-TW beam model, where the displacement field is perturbed by a small unknown function; the shell strain terms are derived and after removing of asymptotically small terms the unknown functions are solved for by minimizing the strain energy. In [18], the shell strain terms have been expressed as:

$$\begin{Bmatrix} \epsilon \\ \kappa \end{Bmatrix} = P\epsilon + T\psi \quad (\text{B.1})$$

where,

$$P = \begin{bmatrix} 1 & 0 & y_3 & -y_2 \\ 0 & 0 & 0 & 0 \\ 0 & 0 & 0 & 0 \\ 0 & 0 & y_2 & y_3 \\ 0 & -2 & 0 & 0 \\ 0 & 0 & 0 & 0 \end{bmatrix} \quad T = \begin{bmatrix} 0 & 0 & 0 \\ 1 & 0 & 0 \\ 0 & 1 & 0 \\ 0 & 0 & 0 \\ b_{22}/2 & 0 & 0 \\ 0 & 0 & 1 \end{bmatrix} \quad (\text{B.2})$$

$$\epsilon = \begin{Bmatrix} \gamma_{11} \\ \kappa_1 \\ \kappa_2 \\ \kappa_3 \end{Bmatrix} \quad \psi = \begin{Bmatrix} 2\epsilon_{12}^0 \\ \epsilon_{22}^0 \\ \kappa_{22}^0 \end{Bmatrix}$$

The only unknowns which exist in ψ and we solve for ψ by minimizing the overall strain energy density which can be written as:

$$2\Pi_0 = \langle\langle (P\epsilon + T\psi)^T K (P\epsilon + T\psi) \rangle\rangle \quad (\text{B.3})$$

Here, K is the plate stiffness matrix associated with the composite layup. The above equation can be minimized with respect to ψ for open section but for closed sections in order to maintain stress continuity additional constraints need to be imposed, which are:

$$\langle\langle w_{i,2} \rangle\rangle = 0 \quad \langle\langle \kappa_{22}^0 \rangle\rangle = 0 \quad (\text{B.4})$$

These constraints can be transformed into a matrix form as:

$$\langle\langle\phi\psi - L\epsilon\rangle\rangle \quad (\text{B.5})$$

As presented in [18], these constraints can be imposed in the form of a langrange multiplier and eventually the value of ψ can be obtained which on plugging back Eq. (B.3), the overall analytical expression for the beam stiffness matrix can be obtained.

For the case of a circular tube (Figure. 3.5) the different matrix mentioned previously take the following form:

$$\begin{aligned}
 P &= \begin{bmatrix} 1 & 0 & R \sin(\theta) & -R \cos(\theta) \\ 0 & 0 & 0 & 0 \\ 0 & 0 & 0 & 0 \\ 0 & 0 & \sin(\theta) & \cos(\theta) \\ 0 & -2 & 0 & 0 \\ 0 & 0 & 0 & 0 \end{bmatrix} & T &= \begin{bmatrix} 0 & 0 & 0 \\ 1 & 0 & 0 \\ 0 & 1 & 0 \\ 0 & 0 & 0 \\ -\frac{1}{2R} & 0 & 0 \\ 0 & 0 & 1 \end{bmatrix} \\
 \phi &= \begin{bmatrix} 1 & 0 & 0 \\ 0 & -\sin(\theta) & -R \sin(\theta) \\ 0 & \cos(\theta) & R \cos(\theta) \\ 0 & 0 & 1 \end{bmatrix} & L &= \begin{bmatrix} 0 & 0 & 0 & 0 \\ 0 & R & 0 & 0 \\ 0 & 0 & 0 & 0 \\ 0 & 0 & 0 & 0 \end{bmatrix}
 \end{aligned} \quad (\text{B.6})$$

where θ is the angle made by the position vector of a point with respect to the positive direction of y_2 . On inputting the above expression into the formulation presented in [18] and solving we get the expression, Eq. (3.2), where:

$$\begin{aligned}
\Delta_A &= \begin{vmatrix} A_{11} & A_{12} & A_{16} \\ A_{12} & A_{22} & A_{26} \\ A_{16} & A_{26} & A_{66} \end{vmatrix} & \Delta_D &= \begin{vmatrix} D_{11} & D_{12} & D_{16} \\ D_{12} & D_{22} & D_{26} \\ D_{16} & D_{26} & D_{66} \end{vmatrix} \\
\mathbb{A} &= -2B_{22}|\bar{D}_{22}| - B_{66}|\bar{D}_{66}| - B_{12}|\bar{D}_{12}| + B_{11}|\bar{D}_{11}| + 3B_{26}|\bar{D}_{26}| \\
\mathbb{B} &= 9B_{26}^2D_{11} - 8B_{22}B_{66}D_{11} + 4B_{12}B_{66}D_{12} + 4B_{11}B_{66}D_{22} - 6B_{26}B_{12}D_{16} - 12B_{26}B_{11}D_{26} \\
&\quad + B_{12}^2D_{66} + 8B_{22}B_{11}D_{66} - A_{11}|\bar{D}_{11}| + 2A_{12}|\bar{D}_{12}| + 2A_{16}|\bar{D}_{16}| - 4A_{22}|\bar{D}_{22}| - 4A_{26}|\bar{D}_{26}| \\
&\quad - A_{66}|\bar{D}_{66}| \\
\mathbb{C} &= -B_{66}(B_{12}^2 + 8B_{11}B_{22}) + 9B_{11}B_{26}^2 + A_{11}(B_{66}D_{22} - 3B_{26}D_{26} + 2B_{22}D_{66}) \\
&\quad - A_{66}(B_{11}D_{22} + B_{12}D_{12} + 2B_{22}D_{11}) + A_{12}(4B_{66}D_{12} + 6B_{26}D_{16} + 2B_{12}D_{66}) \\
&\quad + A_{26}(2B_{12}D_{16} - 6B_{26}D_{11} + 4B_{11}D_{26}) + A_{16}(4B_{22}D_{16} - B_{12}A_{26} - 3B_{26}D_{12}) \\
&\quad + 4A_{22}(B_{66}D_{11} - B_{11}D_{66}) \\
\mathbb{D} &= 8D_{16}|\bar{A}_{16}| - 4D_{66}|\bar{A}_{66}| - 4D_{26}|\bar{A}_{26}| - D_{22}|\bar{A}_{22}| + 4D_{12}|\bar{A}_{12}| - 4D_{11}|\bar{A}_{11}| \\
&\quad + A_{11}(9B_{26}^2 - 8B_{22}B_{66}) - 8A_{12}B_{12}B_{66} + 16A_{22}B_{11}B_{66} + 6A_{16}B_{26}B_{12} \\
&\quad - 24A_{26}B_{11}B_{26} + A_{66}(B_{12}^2 + 8B_{22}B_{11}) \\
\mathbb{E} &= B_{12}|\bar{A}_{12}| - B_{22}|\bar{A}_{22}| - 2B_{66}|\bar{A}_{66}| + 2B_{11}|\bar{A}_{11}| + 3B_{26}|\bar{A}_{26}| \\
\mathbb{Z} &= |\bar{D}_{11}| + 4R^2|\bar{A}_{11}| - 2R(B_{66}D_{22} - 3B_{26}D_{26} + 2B_{22}D_{66}) \\
&\quad - 4R^3(2B_{66}A_{22} - 3B_{26}A_{26} + B_{22}A_{66}) \\
&\quad + R^2(-9B_{26}^2 + 8B_{22}B_{66} + 4D_{66}A_{22} - 4D_{26}A_{26} + D_{22}A_{66})
\end{aligned} \tag{B.7}$$

where, A_{ij} , B_{ij} and D_{ij} correspond to the components of the A , B and D submatrices in the plate stiffness matrix and $|\bar{A}_{ij}|$ is determinant of the minor of the A_{ij} element in:

$$A = \begin{bmatrix} A_{11} & A_{12} & A_{16} \\ A_{12} & A_{22} & A_{26} \\ A_{16} & A_{26} & A_{66} \end{bmatrix}$$

and $|\bar{D}_{ij}|$ is determinant of the minor of the D_{ij} element in:

$$D = \begin{bmatrix} D_{11} & D_{12} & D_{16} \\ D_{12} & D_{22} & D_{26} \\ D_{16} & D_{26} & D_{66} \end{bmatrix}$$

For the case of symmetric laminates where the B matrix is a $[0]_{3 \times 3}$ matrix, we can reduce Eq. (3.2) to:

$$\begin{aligned} C_{11}^b &= 2\pi R \left(A_{11} - \frac{A_{16}^2}{A_{66}} \right) \\ C_{12}^b &= \frac{\pi R}{A_{66}} (-2RA_{16}A_{26} + 2RA_{12}A_{66}) \\ C_{22}^b &= \frac{\pi R}{2A_{66}} (9D_{22}A_{66} - 4R^2(A_{26}^2 - A_{22}A_{66})) \\ C_{33}^b = C_{44}^b &= \frac{\pi R}{Z} (\Delta_D + R^2\mathbb{B} - R^4\mathbb{D} + 4R^6\Delta_A) \end{aligned} \tag{B.8}$$

where,

$$\begin{aligned} \mathbb{B} &= -A_{11}|\bar{D}_{11}| + 2A_{12}|\bar{D}_{12}| + 2A_{16}|\bar{D}_{16}| - 4A_{22}|\bar{D}_{22}| - 4A_{26}|\bar{D}_{26}| - A_{66}|\bar{D}_{66}| \\ \mathbb{D} &= 8D_{16}|\bar{A}_{16}| - 4D_{66}|\bar{A}_{66}| - 4D_{26}|\bar{A}_{26}| - D_{22}|\bar{A}_{22}| + 4D_{12}|\bar{A}_{12}| - 4D_{11}|\bar{A}_{11}| \\ \mathbb{Z} &= |\bar{D}_{11}| + 4R^2|\bar{A}_{11}| \end{aligned}$$

REFERENCES

- [1] K. Terada, T. Miura, and N. Kikuchi, “Digital image-based modeling applied to the homogenization analysis of composite materials,” *Computational Mechanics*, vol. 20, no. 4, pp. 331–346, 1997.
- [2] N. Buannic, P. Cartraud, and T. Quesnel, “Homogenization of corrugated core sandwich panels,” *Composite Structures*, vol. 59, no. 3, pp. 299–312, 2003.
- [3] M. Biancolini, “Evaluation of equivalent stiffness properties of corrugated board,” *Composite Structures*, vol. 69, no. 3, pp. 322–328, 2005.
- [4] W. Yu, “Simplified formulation of mechanics of structure genome,” *AIAA Journal*, pp. 1–9, 2019.
- [5] W. Yu, “A unified theory for constitutive modeling of composites,” *Journal of Mechanics of Materials and Structures*, vol. 11, pp. 379–411, 2016.
- [6] A. Li, R. Li, and J. Fish, “Generalized mathematical homogenization: From theory to practice,” *Computer Methods in Applied Mechanics and Engineering*, vol. 197, no. 41-42, pp. 3225–3248, 2008.
- [7] Y. Cai, L. Xu, and G. Cheng, “Novel numerical implementation of asymptotic homogenization method for periodic plate structures,” *International Journal of Solids and Structures*, vol. 51, no. 1, pp. 284–292, 2014.
- [8] J. Obradovic, S. Boria, and G. Belingardi, “Lightweight design and crash analysis of composite frontal impact energy absorbing structures,” *Composite Structures*, vol. 94, no. 2, pp. 423–430, 2012.
- [9] A. Dash, R. Velmurugan, M. Prasad, and R. S. Sikarwar, “Stability improvement of thin isotropic cylindrical shells with partially filled soft elastic core subjected to external pressure,” *Thin-Walled Structures*, vol. 98, pp. 301–311, 2016.
- [10] N. Buckney, A. Pirrera, S. D. Green, and P. M. Weaver, “Structural efficiency of a wind turbine blade,” *Thin-Walled Structures*, vol. 67, pp. 144–154, 2013.
- [11] A. Dash, R. Velmurugan, and M. Prasad, “Buckling of thin walled composite cylindrical shell filled with solid propellant,” in *IOP Conference Series: Materials Science and Engineering*, IOP Publishing, vol. 270, 2017, p. 012022.
- [12] P. Mangalgiri, “Composite materials for aerospace applications,” *Bulletin of Materials Science*, vol. 22, no. 3, pp. 657–664, 1999.

- [13] N. Raouf, S. H. Pourtakdoust, B. Ashouri Amin Abadi, and A. Rajabi-Ghanavieh, “Structural reliability analysis of solid rocket motor with ellipsoidal cap,” *Journal of Spacecraft and Rockets*, vol. 53, no. 2, pp. 389–392, 2016.
- [14] L. Librescu and O. Song, *Thin-Walled Composite Beams: Theory and Application*. Springer Science & Business Media, 2005, vol. 131.
- [15] K. Bhaskar and L. Librescu, “A geometrically non-linear theory for laminated anisotropic thin-walled beams,” *International Journal of Engineering Science*, vol. 33, no. 9, pp. 1331–1344, 1995.
- [16] Z. Qin and L. Librescu, “On a shear-deformable theory of anisotropic thin-walled beams: Further contribution and validations,” *Composite Structures*, vol. 56, no. 4, pp. 345–358, 2002.
- [17] S. Roy and W. Yu, “An asymptotically correct model for initially curved and twisted thin-walled composite beams,” *International Journal of Solids and Structures*, vol. 44, no. 11, pp. 4039–4052, 2007.
- [18] W. Yu, L. Liao, D. H. Hodges, and V. V. Volovoi, “Theory of initially twisted, composite, thin-walled beams,” *Thin-Walled Structures*, vol. 43, no. 8, pp. 1296–1311, 2005.
- [19] V. Berdichevsky, E. Armanios, and A. Badir, “Theory of anisotropic thin-walled closed-cross-section beams,” *Composites Engineering*, vol. 2, no. 5, pp. 411–432, 1992.
- [20] D. Harursampath, A. B. Harish, and D. H. Hodges, “Model reduction in thin-walled open-section composite beams using variational asymptotic method. part I: Theory,” *Thin-Walled Structures*, vol. 117, pp. 356–366, 2017.
- [21] A. Bensoussan, *Asymptotic Analysis for Periodic Structures*. Amsterdam: North-Holland Publication Company, 2011.
- [22] V. Berdichevsky, “Variational-asymptotic method of constructing a theory of shells,” *Journal of Applied Mathematics and Mechanics*, vol. 43, no. 4, pp. 711–736, 1979.
- [23] C. Cesnik and D. H. Hodges, “VABS: A new concept for composite rotor blade cross-sectional modeling,” *Journal of the American Helicopter Society*, vol. 42, p. 27, 1997.
- [24] W. Yu and M. Blair, “GEBT: A general-purpose nonlinear analysis tool for composite beams,” *Composite Structures*, vol. 94, no. 9, pp. 2677–2689, 2012.
- [25] V. V. Volovoi and D. H. Hodges, “Theory of anisotropic thin-walled beams,” *Journal of Applied Mechanics*, vol. 67, no. 3, pp. 453–459, 2000.

- [26] V. V. Volovoi and D. H. Hodges, “Single-and multicelled composite thin-walled beams,” *AIAA Journal*, vol. 40, no. 5, pp. 960–965, 2002.
- [27] Y. Xia, M. Friswell, and E. S. Flores, “Equivalent models of corrugated panels,” *International Journal of Solids and Structures*, vol. 49, no. 13, pp. 1453–1462, 2012.
- [28] L. Valdevit, J. Hutchinson, and A. Evans, “Structurally optimized sandwich panels with prismatic cores,” *International Journal of Solids and Structures*, vol. 41, no. 18, pp. 5105–5124, 2004.
- [29] M. Leekitwattana, S. Boyd, and R. Shenoi, “Evaluation of the transverse shear stiffness of a steel bi-directional corrugated-strip-core sandwich beam,” *Journal of Constructional Steel Research*, vol. 67, no. 2, pp. 248–254, 2011.
- [30] E. Knox, M. Cowling, and I. Winkle, “Adhesively bonded steel corrugated core sandwich construction for marine applications,” *Marine Structures*, vol. 11, no. 4, pp. 185–204, 1998.
- [31] D. Dubina, V. Ungureanu, and L. Gîlia, “Cold-formed steel beams with corrugated web and discrete web-to-flange fasteners,” *Steel Construction*, vol. 6, no. 2, pp. 74–81, 2013.
- [32] C. Ng and H. Zheng, “Sound transmission through double-leaf corrugated panel constructions,” *Applied Acoustics*, vol. 53, no. 1, pp. 15–34, 1998.
- [33] D. Twede, S. E. Selke, D.-P. Kamdem, and D. Shires, *Cartons, Crates and Corrugated board: Handbook of Paper and Wood Packaging Technology*. DEStech Publications, Inc, 2014.
- [34] S. Bapanapalli, O. Martinez, C. Gogu, B. Sankar, R. Haftka, and M. Blosser, “Analysis and design of corrugated-core sandwich panels for thermal protection systems of space vehicles,” in *47th AIAA/ASME/ASCE/AHS/ASC Structures, Structural Dynamics, and Materials Conference*, May 2006.
- [35] O. A. Martinez, B. V. Sankar, R. Haftka, S. K. Bapanapalli, and M. L. Blosser, “Micromechanical analysis of composite corrugated-core sandwich panels for integral thermal protection systems,” *AIAA Journal*, vol. 45, no. 9, pp. 2323–2336, 2007.
- [36] C. Thill, J. A. Etches, I. P. Bond, K. D. Potter, and P. M. Weaver, “Composite corrugated structures for morphing wing skin applications,” *Smart Materials and Structures*, vol. 19, no. 12, p. 124009, Nov. 2010.
- [37] F. Previtali, G. Molinari, A. F. Arrieta, M. Guillaume, and P. Ermanni, “Design and experimental characterisation of a morphing wing with enhanced corrugated skin,” *Journal of Intelligent Material Systems and Structures*, vol. 27, no. 2, pp. 278–292, 2016.

- [38] T. Yokozeki, S. Takeda, T. Ogasawara, and T. Ishikawa, “Mechanical properties of corrugated composites for candidate materials of flexible wing structures,” *Composites Part A: Applied Science and Manufacturing*, vol. 37, no. 10, pp. 1578–1586, 2006.
- [39] C. Gentilina, L. Nobilea, and K. A. Seffen, “Numerical analysis of morphing corrugated plates,” *Procedia Engineering*, vol. 1, no. 1, pp. 79–82, 2009.
- [40] I. Dayyani, M. Friswell, S. Ziaei-Rad, and E. S. Flores, “Equivalent models of composite corrugated cores with elastomeric coatings for morphing structures,” *Composite Structures*, vol. 104, pp. 281–292, 2013.
- [41] Y.-J. Cheon and H.-G. Kim, “An equivalent plate model for corrugated-core sandwich panels,” *Journal of Mechanical Science and Technology*, vol. 29, no. 3, pp. 1217–1223, 2015.
- [42] N. Talbi, A. Batti, R. Ayad, and Y. Guo, “An analytical homogenization model for finite element modelling of corrugated cardboard,” *Composite Structures*, vol. 88, no. 2, pp. 280–289, 2009.
- [43] Z. Aboura, N. Talbi, S. Allaoui, and M. Benzeggagh, “Elastic behavior of corrugated cardboard: Experiments and modeling,” *Composite Structures*, vol. 63, no. 1, pp. 53–62, 2004.
- [44] Z. Ye and W. Yu, “Homogenization of piecewise straight corrugated plates,” in *54th AIAA/ASME/ASCE/AHS/ASC Structures, Structural Dynamics, and Materials Conference*, 2013, p. 1608.
- [45] Z. Ye, V. Berdichevsky, and W. Yu, “An equivalent classical plate model of corrugated structures,” *International Journal of Solids and Structures*, vol. 51, no. 11-12, pp. 2073–2083, 2014.
- [46] N. P. Gokhale, P. Kala, V. Sharma, and M. Palla, “Effect of deposition orientations on dimensional and mechanical properties of the thin-walled structure fabricated by tungsten inert gas (tig) welding-based additive manufacturing process,” *Journal of Mechanical Science and Technology*, vol. 34, no. 2, pp. 701–709, 2020.
- [47] A. B. Coffey, A. Brazier, M. Tierney, A. G. Gately, and C. O’Bradaigh, “Development of thin-walled fibre-reinforced structures for medical applications,” *Composites Part A: Applied Science and Manufacturing*, vol. 34, no. 6, pp. 535–542, 2003.
- [48] H. Hermawan, D. Dubé, and D. Mantovani, “Developments in metallic biodegradable stents,” *Acta Biomaterialia*, vol. 6, no. 5, pp. 1693–1697, 2010.

- [49] F. Ma, C. Wang, C. Liu, and J. H. Wu, “Structural designs, principles, and applications of thin-walled membrane and plate-type acoustic/elastic metamaterials,” *Journal of Applied Physics*, vol. 129, p. 231 103, 2021.
- [50] P. F. Weyers, *Vibration and near-field sound of thin-walled cylinders caused by internal turbulent flow*. National Aeronautics and Space Administration, 1960, vol. 430.
- [51] C. Ren, Q. Li, and D. Yang, “Quasi-static and sound insulation performance of a multi-functional cylindrical cellular shell with bidirectional negative-stiffness metamaterial cores,” *International Journal of Mechanical Sciences*, vol. 180, p. 105 662, 2020.
- [52] L. J. Gibson and M. F. Ashby, *Cellular Solids: Structure and Properties*. Cambridge university press, 1999.
- [53] S. Arabnejad and D. Pasini, “Mechanical properties of lattice materials via asymptotic homogenization and comparison with alternative homogenization methods,” *International Journal of Mechanical Sciences*, vol. 77, pp. 249–262, 2013.
- [54] A.-J. Wang and D. L. McDowell, “In-plane stiffness and yield strength of periodic metal honeycombs,” *Journal of Engineering Materials and Technology*, vol. 126, no. 2, pp. 137–156, Mar. 2004.
- [55] I. Masters and K. Evans, “Models for the elastic deformation of honeycombs,” *Composite Structures*, vol. 35, no. 4, pp. 403–422, 1996.
- [56] R. Christensen, “Mechanics of low density materials,” *Journal of the Mechanics and Physics of Solids*, vol. 34, no. 6, pp. 563–578, 1986.
- [57] A. Askar and A. Cakmak, “A structural model of a micropolar continuum,” *International Journal of Engineering Science*, vol. 6, no. 10, pp. 583–589, 1968.
- [58] J. Chen, Y. Huang, and M. Ortiz, “Fracture analysis of cellular materials: A strain gradient model,” *Journal of the Mechanics and Physics of Solids*, vol. 46, no. 5, pp. 789–828, 1998.
- [59] Z. Bažant and M. Christensen, “Analogy between micropolar continuum and grid frameworks under initial stress,” *International Journal of Solids and Structures*, vol. 8, no. 3, pp. 327–346, 1972.
- [60] X. Wang and W. Stronge, “Micropolar theory for two-dimensional stresses in elastic honeycomb,” *Proceedings of the Royal Society of London. Series A: Mathematical, Physical and Engineering Sciences*, vol. 455, no. 1986, pp. 2091–2116, 1999.

- [61] K. Sab and F. Pradel, “Homogenisation of periodic cosserat media,” *International Journal of Computer Applications in Technology*, vol. 34, no. 1, pp. 60–71, 2009.
- [62] F. Reis and J. Ganghoffer, “Equivalent mechanical properties of auxetic lattices from discrete homogenization,” *Computational Materials Science*, vol. 51, no. 1, pp. 314–321, 2012.
- [63] I. Berinskii, “Elastic in-plane properties of cellular materials: Discrete approach,” *Mechanics of Materials*, vol. 148, p. 103 501, 2020.
- [64] Y. Chen and H. Hu, “In-plane elasticity of regular hexagonal honeycombs with three different joints: A comparative study,” *Mechanics of Materials*, vol. 148, p. 103 496, 2020.
- [65] S. Gonella and M. Ruzzene, “Homogenization of vibrating periodic lattice structures,” *Applied Mathematical Modelling*, vol. 32, no. 4, pp. 459–482, 2008.
- [66] A. Vigliotti and D. Pasini, “Stiffness and strength of tridimensional periodic lattices,” *Computer Methods in Applied mechanics and Engineering*, vol. 229, pp. 27–43, 2012.
- [67] D. Mousanezhad, B. Haghpanah, R. Ghosh, A. M. Hamouda, H. Nayeb-Hashemi, and A. Vaziri, “Elastic properties of chiral, anti-chiral, and hierarchical honeycombs: A simple energy-based approach,” *Theoretical and Applied Mechanics Letters*, vol. 6, no. 2, pp. 81–96, 2016.
- [68] D. H. Hodges, *Nonlinear Composite Beam Theory*. American Institute of Aeronautics and Astronautics, 2006.
- [69] A. Deo and W. Yu, “Thin-walled composite beam cross-sectional analysis using the mechanics of structure genome,” *Thin-Walled Structures*, vol. 152, p. 106 663, 2020.
- [70] J. Fish and T. Belytschko, *A First Course in Finite Elements*. Wiley, 2007.
- [71] A. Deo and W. Yu, “Equivalent plate properties of composite corrugated structures using mechanics of structure genome,” *International Journal of Solids and Structures*, vol. 208-209, pp. 262–271, 2021.
- [72] R. Chandra and I. Chopra, “Experimental and theoretical analysis of composite I-beams with elastic couplings,” eng, *AIAA Journal*, vol. 29, no. 12, pp. 2197–2206, 1991.
- [73] H. Chen, W. Yu, and M. Capellaro, “A critical assessment of computer tools for calculating composite wind turbine blade properties,” *Wind Energy*, vol. 13, no. 6, pp. 497–516, 2010.
- [74] K.-J. Park, K. Jung, and Y.-W. Kim, “Evaluation of homogenized effective properties for corrugated composite panels,” *Composite Structures*, vol. 140, pp. 644–654, 2016.

VITA

Ankit Deo was born on Feb. 1, 1992, in Chennai, Tamil Nadu, India. He graduated from India Institute of Technology, Kanpur, India on July 2015 with Bachelor and Master degrees. In Fall 2015, he started his PhD graduate program in the Multiscale Structural Mechanics Lab at the School of Aeronautics and Astronautics at Purdue University working under the guidance of Prof. Wenbin Yu. During the course of the PhD program he went for a internship at Dassault Systèmes, Providence from January 2018 to July 2018. At the internship he worked in the field of simulating Additive Manufacturing processes. His expertise are in the field of micromechanics, thin-walled composite structures, finite element analysis and scientific softwares such as Abaqus, MATLAB, etc.